

DISSERTATION

**Measuring Dynamical Masses of  
Galaxy Clusters  
with Stacked Phase Space**

by

**Akinari Hamabata**

A thesis submitted to  
the graduate school of science,  
the University of Tokyo  
in partial fulfillment of  
the requirements for the degree  
of  
Master of Science in Physics

January, 2018



# Abstract

The mass of galaxy clusters that has been estimated by using motions of astronomical objects around the clusters is called the dynamical mass. The dynamical mass approach provides a complementary method to estimate cluster masses which are dominated by dark matter and hence difficult to measure. In addition, the comparison of the dynamical mass with the mass estimated by gravitational lensing provides an important means of testing General Relativity.

However, previous studies of dynamical masses did not fully take account of the complexity of dynamics around clusters. To estimate the dynamical mass accurately, we have to understand more about the dynamical state of clusters. Using a large box  $N$ -body simulation, we analyze motions of dark matter halos surrounding galaxy clusters. We find that the stacked pairwise velocity distribution can be well described by a two component model, which consists of the infall component and the splashback component. We find that very little fraction of halos is well relaxed even at  $z = 0$ . We also find that the radial velocity distribution of the infall component deviates from the Gaussian distribution and is described well by the Johnson SU distribution. In addition, we study the dependence of the phase space distribution on cluster masses as well as masses of satellite-halos and sub-halos.

Our model is then used to derive the probability distribution function of the line-of-sight velocity  $v_{\text{los}}$ , which can directly be compared with observations. In doing so, we project our model of the three-dimensional phase space distribution along the line-of-sight by taking proper account of the effect of the Hubble flow. We find that we can estimate cluster masses even at the outer region of the projected phase space  $r_{\text{proj}} > 2 \text{ Mpc}/h$ , which is complementary to the traditional approach to use velocity dispersions measured at  $r_{\text{proj}} \lesssim 1 \text{ Mpc}/h$ . Our model allows us to understand how the  $v_{\text{los}}$  distributions at large radii can constrain cluster masses, which is complicated due to the competing effects of the infall velocities and the Hubble flow. We conclude that by using SDSS spectroscopic galaxies we can constrain mean cluster masses with an accuracy of 4% by using the outer phase space distributions at  $r_{\text{proj}} > 2 \text{ Mpc}/h$ . We discuss potential systematic errors associated with this method.



# Contents

<b>Chapter 1. Introduction</b>	<b>1</b>
<b>Chapter 2. Basic Dynamics of Dark Matter Halos</b>	<b>5</b>
2.1 Dynamics of Collisionless Particle . . . . .	5
2.2 Escape Velocity Profile of a Galaxy Cluster . . . . .	8
<b>Chapter 3. Basic Method of Dynamical Mass Measurement</b>	<b>11</b>
3.1 Measurement of $v_{\text{los}}$ . . . . .	12
3.2 Stacking Galaxy Clusters . . . . .	13
3.3 Reconstruction of Masses of Galaxy Clusters from $v_{\text{los}}$ Histograms . . . . .	14
<b>Chapter 4. Modeling the Phase Space Distribution of Dark Matter Halos</b>	<b>19</b>
4.1 Phase Space Distribution of Halos from $N$ -body Simulation . . . . .	21
4.2 Overview of Our Model . . . . .	21
4.3 Radial Velocity Distribution . . . . .	23
4.4 Tangential Velocity Distribution . . . . .	28
4.5 Radial Dependence of Parameters in The Model . . . . .	32
4.6 Reconstruct $v_{\text{los}}$ Histogram . . . . .	42
4.7 Dependence of the Phase Space Distribution on Satellite-Halo Masses . . . . .	52
<b>Chapter 5. Measurement of Dynamical Masses from <math>v_{\text{los}}</math> Distribution Functions</b>	<b>67</b>
5.1 Dependence of the PDF of $v_{\text{los}}$ on Cluster Masses . . . . .	67
5.2 Origin of Dynamical Mass Dependence of the PDF of $v_{\text{los}}$ . . . . .	71
5.3 Accuracy of Mass Estimation . . . . .	75
5.4 Systematic Errors . . . . .	76
5.4.1 Dependence of the PDF of $v_{\text{los}}$ on Satellite-Halo and Sub-Halo Masses	76
5.4.2 Inaccuracy of Our Model . . . . .	79
5.4.3 Measurement Errors of Galaxy Redshifts . . . . .	82
5.4.4 Miscentering . . . . .	82
<b>Chapter 6. Summary and Future Prospects</b>	<b>85</b>
<b>Acknowledgments</b>	<b>87</b>

---

<b>Appendix A. Review of a Cluster Finding Method</b>	<b>89</b>
A.1 Calculating Probability of Red Sequence Galaxy . . . . .	89
A.2 Calculating the Number of Member Galaxies . . . . .	90
A.3 Refining Cluster Candidates . . . . .	91
<b>Appendix B. Comparison Between Velocity Dispersions and Cluster Masses</b>	<b>93</b>

# Chapter 1

## Introduction

In the  $\Lambda$  Cold Dark Matter ( $\Lambda$ CDM) universe, the energy budget of the Universe is composed of three components. The first component is baryon, which represent ordinary matter such as stars, galaxies, and intracluster medium. The second component is dark matter, which interacts mostly via gravitational field. While the true nature of dark matter is unknown, it is usually assumed to interact with baryon only very weakly, which makes it very challenging to infer the distribution of dark matter from astronomical observations. The third component is dark energy. Dark energy is a hypothetical component with negative pressure, which is introduced as a source of the accelerated expansion of the Universe. In the standard  $\Lambda$ CDM model, initial density perturbations grow by the gravitational instability, and form the cosmic structure hierarchical.

We can extract information on the initial density perturbation, the structure formation history, and cosmological parameters from distributions of cosmic structures such as galaxy clusters. Galaxy clusters are the biggest self-gravitating system in the Universe, whose typical size is 1 Mpc, the typical weight is  $10^{14}M_{\odot}$ , and the main component is dark matter. For instance, we can extract the matter density ( $\Omega_m$ ) and the amplitude of the density perturbation ( $\sigma_8$ ) from the abundance of galaxy clusters (e.g., Rozo et al. 2010). Fig. 1.1 shows an example of cosmological constraints obtained from the abundance of galaxy clusters. The dominant source of the uncertainty in this analysis is the uncertainty of estimating cluster masses, which is necessary to compare observations with theory involving dark matter. To constrain cosmological parameters accurately, we need to estimate masses of galaxy clusters precisely, which is difficult because masses of clusters are dominated by dark matter.

There are several methods to estimate masses of galaxy clusters, including gravitational lensing (Schneider et al. 1992; Umetsu et al. 2011; Oguri et al. 2012; Newman et al. 2013), the X-ray observation (Sarazin 1988; Vikhlinin et al. 2006), and the Sunyaev-Zel'dovich effect (Sunyaev & Zeldovich 1972; Arnaud et al. 2010; Planck Collaboration et al. 2014). In addition, another method to estimate masses of galaxy clusters by using the relative motion of galaxies surrounding galaxy clusters has also been proposed (Smith 1936; Busha et al. 2005; Rozo et al. 2015; Farahi et al. 2016). In this thesis, we call the mass estimated by motions of galaxies around clusters as the dynamical mass. It is of great importance to compare cluster masses derived by these different methods in order to understand

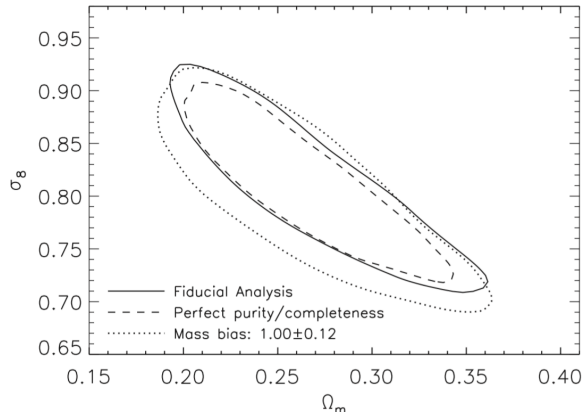


Figure 1.1: The cosmological constraints obtained from the abundance of galaxy clusters. The maxBCG clusters (Koester et al. 2007), and the mass calibration by stacked weak lensing (Johnston et al. 2007) are used in this analysis. The plot shows 68% confidence regions. The solid line shows the result of the fiducial analysis, the dotted line shows the analysis with a more conservative error on the mass calibration, and the dashed line shows the analysis with the perfect purity and completeness. Other cosmological parameters are fixed at WMAP5 values (Dunkley et al. 2009). Taken from Rozo et al. (2010).

systematic errors inherent to the individual methods. Different methods have different systematic errors, which can be inferred and hopefully corrected for by cross-checking the results of the individual methods.

Furthermore, we can also test General Relativity by comparing masses of galaxy clusters estimated by gravitational lensing effect (hereafter referred to as the lens mass) with dynamical masses (Schmidt 2010; Lam et al. 2013). Because the dynamical mass ( $M_{\text{dyn}}$ ) and lens mass ( $M_{\text{lens}}$ ) have different information about metric, we can test General Relativity by comparing these two masses. Fig. 1.2 is an example of the comparison between  $M_{\text{dyn}}$  and  $M_{\text{lens}}$  taken from Schmidt (2010). In that paper, they assume one class of modified gravity theories,  $f(R)$  gravity (Nojiri & Odintsov 2011), which add a new term  $f(R)$  to Lagrangian of the gravitational field ( $\mathcal{L}_G$ ) as

$$\mathcal{L}_G = R + f(R) , \quad (1.1)$$

where  $R$  is curvature, and  $f(R)$  is

$$f(R) = -2\Lambda - f_{R0} \frac{\overline{R_0}^2}{R^2} . \quad (1.2)$$

Note that  $\Lambda$  is cosmological constant,  $\overline{R_0}$  is the present day background curvature, and  $f_{R0}$  is a parameter of the model. Then they define  $\overline{g}_{\text{vir},f(R)}$  as the ratio of the dynamical and lens masses

$$\overline{g}_{\text{vir},f(R)} = \left( \frac{M_{\text{dyn}}}{M_{\text{lens}}} \right)^{5/3} . \quad (1.3)$$

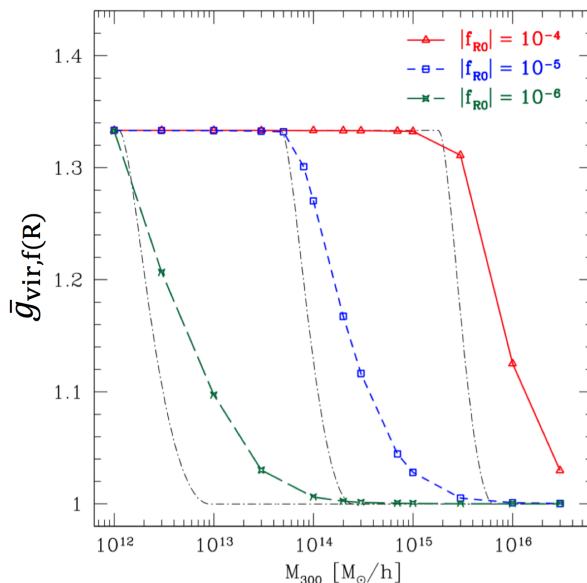


Figure 1.2: Comparison between galaxy cluster masses estimated by gravitational lensing ( $M_{\text{lens}}$ ) and by using relative motions of dark matter halos around clusters ( $M_{\text{dyn}}$ ) for one class of modified gravity theories,  $f(R)$  gravity. The vertical axis is  $\bar{g}_{\text{vir},f(R)} = (M_{\text{dyn}}/M_{\text{lens}})^{5/3}$ . The horizontal axis is  $M_{\text{lens}}$ . Symbols show the mass ratios taken from  $N$ -body simulations, and the corresponding dot-dashed lines show the results of an analytic calculation with approximations. Different symbols corresponds to different  $|f_{R0}|$ , which is a parameter of  $f(R)$  gravity. Taken from Schmidt (2010).

The value of this parameter is always unity for General Relativity, but can deviate from the unity for modified gravity theories. In Fig. 1.2, we show the comparison between  $M_{\text{lens}}$  and  $M_{\text{dyn}}$  in the case of the  $f(R)$  gravity. From Fig. 1.2, we can see that the ratio of  $M_{\text{lens}}$  and  $M_{\text{dyn}}$  deviates from unity for low-mass halos up to  $\sim 30\%$ , which can be tested with observations. This example highlights the importance of accurate measurements of  $M_{\text{dyn}}$  to test General Relativity.

While there are some previous studies to estimate  $M_{\text{dyn}}$  (Smith 1936; Busha et al. 2005; Rozo et al. 2015; Farahi et al. 2016), there is room for improvement in several ways. For example, to estimate  $M_{\text{dyn}}$  accurately, we have to understand the dynamical state of dark matter halos around galaxy clusters. However, there are no existing theoretical methods of the  $M_{\text{dyn}}$  measurement which fully take account of the complexity of the dynamical state of dark matter halos. Moreover, in most of previous studies, motions of galaxies (or dark matter halos) within  $\sim 1$  Mpc from centers of galaxy clusters are used to derive  $M_{\text{dyn}}$ . In this thesis, we study the phase space distribution of galaxies around galaxy clusters up to very large distances, several tens of Mpc from cluster centers, by using an  $N$ -body simulation, and propose a new method to measure  $M_{\text{dyn}}$  using a stacked phase space diagram. For this purpose, we construct a new model of the phase space distribution of dark matter halos around clusters. We discuss how  $M_{\text{dyn}}$  can be estimated by the stacked phase space distribution at large distances beyond  $\sim 2$  Mpc, which is

highly complementary to traditional methods to estimate  $M_{\text{dyn}}$  from motions of galaxies within  $\sim 1$  Mpc from cluster centers.

This thesis is organized as follows. In Chapter 2, we review the basic dynamics of dark matter halos. In Chapter 3, we review previous methods to measure  $M_{\text{dyn}}$ . We show our new model of the phase space distribution of dark matter halos in Chapter 4. In Chapter 5, we discuss how to measure  $M_{\text{dyn}}$  by using our model. Finally, we conclude in Chapter 6.

# Chapter 2

## Basic Dynamics of Dark Matter Halos

To estimate  $M_{\text{dyn}}$  of galaxy clusters, we need to know the phase space distribution or the dynamical state of dark matter halos. In this Chapter, we review basic theory of dynamics of dark matter halos.

### 2.1 Dynamics of Collisionless Particle

Dark matter particles are usually assumed to be collisionless. The dynamics of such collisionless particles are governed by the collisionless Boltzmann equation (see e.g., Mo et al. 2010)

$$\frac{df}{dt} = \frac{\partial f}{\partial t} + \sum_i v_i \frac{\partial f}{\partial x_i} - \sum_i \frac{\partial \phi}{\partial x_i} \frac{\partial f}{\partial v_i} = 0, \quad (2.1)$$

where  $f = f(\mathbf{x}, \mathbf{v}, t)$  is the phase space distribution function of the particles, and  $\phi = \phi(\mathbf{x}, t)$  is the gravitational potential. Note that we assume only single mass ( $m$ ) particles.

We can derive the continuity equation by integrating eq. (2.1) over the velocity space

$$\frac{\partial \rho}{\partial t} + \sum_i v_i \frac{\partial}{\partial x_i} (\rho \bar{v}_i) = 0, \quad (2.2)$$

where  $\rho$  is the density described as

$$\rho(\mathbf{x}, t) = m \int d^3v f(\mathbf{x}, \mathbf{v}, t), \quad (2.3)$$

and  $\bar{v}_i$  is the  $i$ -th component of the mean velocity given as

$$\bar{v}_i(\mathbf{x}, t) = \frac{\int d^3v v_i f(\mathbf{x}, \mathbf{v}, t)}{\int d^3v f(\mathbf{x}, \mathbf{v}, t)}. \quad (2.4)$$

We can also derive equation of motion for collisionless particles by multiplying eq. (2.1) by  $v_j$  and integrating eq. (2.1) over the velocity space

$$\frac{\partial \overline{\rho v_j}}{\partial t} + \sum_i \frac{\partial}{\partial x_i} (\overline{\rho v_i v_j}) + \rho \frac{\partial \phi}{\partial x_j} = 0, \quad (2.5)$$

where

$$\overline{v_i v_j}(\mathbf{x}, t) = \frac{\int d^3 v v_i v_j f(\mathbf{x}, \mathbf{v}, t)}{\int d^3 v f(\mathbf{x}, \mathbf{v}, t)}. \quad (2.6)$$

Now we define  $\sigma_{ij}$  as

$$\sigma_{ij} = \sqrt{\overline{v_i v_j} - \overline{v_i} \overline{v_j}}. \quad (2.7)$$

Using  $\sigma_{ij}$ , eq. (2.7) is rewritten as

$$\frac{\partial \overline{v_j}}{\partial t} + \sum \overline{v_i} \frac{\partial \overline{v_j}}{\partial x_i} = -\frac{1}{\rho} \sum \frac{\partial}{\partial x_i} (\rho \sigma_{ij}^2) - \frac{\partial \phi}{\partial x_j}. \quad (2.8)$$

Eq. (2.8) is called the Jeans equation.

We can also derive equation of energy by multiplying eq. (2.5) by  $x_k$  and integrating over real space

$$\int d^3 x x_k \frac{\partial (\overline{\rho v_j})}{\partial t} = - \sum_i \int d^3 x x_k \frac{\partial}{\partial x_i} (\overline{\rho v_i v_j}) - \int d^3 x \rho x_k \frac{\partial \phi}{\partial x_j}. \quad (2.9)$$

The second term of right hand side is rewritten as

$$- \sum_i \int d^3 x x_k \frac{\partial}{\partial x_i} (\overline{\rho v_i v_j}) = \int d^3 x (\overline{\rho v_j v_k}) - \sum_i \int dS_i x_k \overline{\rho v_i v_j}, \quad (2.10)$$

where,  $dS_i$  corresponds to the surface element oriented toward the direction of  $x_i$ . The first term of right hand side means the kinetic energy tensor

$$K_{jk} = \frac{1}{2} \int d^3 x (\overline{\rho v_j v_k}). \quad (2.11)$$

The second term of right hand side of eq. (2.10) means the surface pressure

$$\Sigma_{jk} = - \sum_i \int dS_i x_k \overline{\rho v_i v_j}. \quad (2.12)$$

Using the Chandrasekhar potential energy tensor defined as

$$W_{jk} = - \int d^3 x \rho x_j \frac{\partial \phi}{\partial x_k}, \quad (2.13)$$

we rewrite eq. (2.9) as

$$\int d^3 x x_k \frac{\partial (\overline{\rho v_j})}{\partial t} = 2K_{jk} + W_{jk} + \Sigma_{jk}. \quad (2.14)$$

The left hand side of eq. (2.14) can be rewritten as

$$\begin{aligned}
 \int d^3x x_k \frac{\partial(\rho \bar{v}_j)}{\partial t} &= \frac{1}{2} \frac{d}{dt} \int d^3x \rho (x_k \bar{v}_j + x_j \bar{v}_k) \\
 &= -\frac{1}{2} \frac{d}{dt} \int d^3x \frac{\partial(\rho \bar{v}_i)}{\partial x_i} x_j x_k \\
 &= \frac{1}{2} \frac{d}{dt} \int d^3x \frac{\partial \rho}{\partial t} x_j x_k \\
 &= \frac{1}{2} \frac{d^2 I_{jk}}{dt^2},
 \end{aligned} \tag{2.15}$$

where  $I_{jk}$  is the inertial moment tensor defined as

$$I_{jk} = \int d^3x \rho x_j x_k . \tag{2.16}$$

By using eqs. (2.10), (2.11), (2.12), (2.13), (2.15), and (2.16), eq. (2.9) can be rewritten as

$$\frac{1}{2} \frac{d^2 I_{jk}}{dt^2} = 2K_{jk} + W_{jk} + \Sigma_{jk} . \tag{2.17}$$

Eq. (2.17) is called the tensor virial theorem. We can derive the scalar virial theorem by taking trace of eq. (2.17)

$$\frac{1}{2} \frac{d^2 I}{dt^2} = 2K + W + \Sigma, \tag{2.18}$$

where

$$I = \int d^3x \rho |\mathbf{x}|^2, \tag{2.19}$$

$$K = \frac{1}{2} \int d^3x (\rho |\bar{\mathbf{v}}|^2), \tag{2.20}$$

$$W = - \int d^3x \rho \mathbf{x} \cdot \nabla \phi, \tag{2.21}$$

$$\begin{aligned}
 \Sigma &= \text{Tr}(\Sigma_{jk}) \\
 &= - \int dS_i x_k \rho \bar{v}_i \bar{v}_k.
 \end{aligned} \tag{2.22}$$

For a static system,  $d^2 I / dt^2 = 0$ , eq. (2.18) becomes

$$2K + W + \Sigma = 0 . \tag{2.23}$$

When we neglect the surface term  $\Sigma$ , the total energy  $E$  ( $\equiv K + W$ ) can be described as

$$E = -K = \frac{1}{2} W . \tag{2.24}$$

This model is used as a basic of dynamics of dark matter particles and halos.

If the system is spherically symmetric, eq. (2.8) can be rewritten in a spherical coordinate as

$$\frac{\partial \bar{v}_r}{\partial t} + \bar{v}_r \frac{\partial \bar{v}_r}{\partial r} = -\frac{1}{\rho} \frac{\partial}{\partial r} (\rho \sigma_{rr}^2) - \frac{2\beta \sigma_{rr}^2}{r} - \frac{\partial \phi}{\partial r}, \quad (2.25)$$

where

$$\beta = 1 - \frac{\sigma_{\theta\theta}^2 + \sigma_{\phi\phi}^2}{2\sigma_{rr}^2} \quad (2.26)$$

is called the velocity anisotropy parameter. If the velocity dispersion is isotropic,  $\beta$  reduces to zero, and if the radial (tangential) component is dominant,  $\beta = 1$  ( $\beta \rightarrow -\infty$ ).

When we assume that the system is static, we can rewrite eq. (2.25) by using eq. (2.26) as

$$\frac{GM(< r)}{r} = \frac{1}{2} \sigma_{rr}^2(r) \times (3 + 2\beta), \quad (2.27)$$

where  $M(< r)$  is the mass within  $r$ . Once we set  $r$  to  $r_{200}$ , which is the radius within which the average density is 200 times the critical density of the Universe,  $M_{200} \propto r_{200}^3$ , and regard  $\beta$  as constant, we can describe  $\sigma_{rr}(r_{200})$  as

$$\sigma_{rr}(r_{200}) \propto M_{200}^{1/3} \quad (2.28)$$

This equation shows the most basic relationship between masses of galaxy clusters and dynamics within dark matter halos.

## 2.2 Escape Velocity Profile of a Galaxy Cluster

The caustic model is a model that focuses on dark matter halos of infall sequence to galaxy clusters, based on a spherical collapse model (Diaferio & Geller 1997). In Stark et al. (2016), the caustic model is extended to apply it for an expanding Universe. In this Section, we review an improved caustic method based on Stark et al. (2016).

The caustic method is based on collisionless infall. The escape velocity ( $v_{\text{esc}}$ ) is described as

$$v_{\text{esc}}^2(r) = -2\Phi(r), \quad (2.29)$$

where  $\Phi$  is the potential. Following Nandra et al. (2012), they construct effective  $\Phi$  for an acceleration experienced particle with zero angular momentum by two components as

$$\vec{\nabla}\Phi = \vec{\nabla}\Psi + qH^2 r \hat{r}. \quad (2.30)$$

The first term of right hand side of eq. (2.30) corresponds to the Newtonian gravitational potential of a galaxy cluster, and the second term corresponds to the effect of expanding Universe, where,  $H$  is Hubble parameter, and  $q$  is given by  $q \equiv -(\ddot{a}a)/\dot{a}^2$ . Integrating eq. (2.30),

$$\int_r^{r_{\text{eq}}} d\Phi = \int_r^{r_{\text{eq}}} d\Psi + qH^2 \int_r^{r_{\text{eq}}} r' dr'. \quad (2.31)$$

Note that the integration is performed out to a finite radius,  $r_{\text{eq}}$ , which is termed the "equivalence radius" in Behroozi et al. (2013a). The finite range of the integration is due to the fact that the escape velocity at infinity is poorly defined. Following Behroozi et al. (2013a), they define the  $r_{\text{eq}}$  to be the point at which the acceleration due to the gravitational potential and the acceleration of the expanding Universe are equivalent ( $\vec{\nabla}\Phi = 0$ ). Hence,  $r_{\text{eq}}$  is defined as

$$r_{\text{eq}} = \left( \frac{GM}{-qH^2} \right)^{1/3}, \quad (2.32)$$

where  $M$  is the mass of the galaxy cluster. They assume that at large  $r$ ,  $\Psi$  is given by  $\Psi = -GM/r$  via the Poisson equation. Then, by integrating eq. (2.31), we have

$$\Phi(r) = \Psi(r) - \Psi(r_{\text{eq}}) + \frac{1}{2}qH^2(r^2 - r_{\text{eq}}^2) + \Phi(r_{\text{eq}}). \quad (2.33)$$

At  $r_{\text{eq}}$ ,  $v_{\text{esc}}$  must be zero,  $\Phi(r_{\text{eq}}) = 0$ . Hence,  $v_{\text{esc}}$  is described as

$$v_{\text{esc}}(r) = \sqrt{-2\{\Psi(r) - \Psi(r_{\text{eq}})\} - qH^2(r^2 - r_{\text{eq}}^2)}. \quad (2.34)$$

This is the one of the most basic models to describe infalling dark matter halos to a galaxy cluster. This model, however, cannot predict the phase space distribution of dark matter halos which we study in Section 4.3.



# Chapter 3

## Basic Method of Dynamical Mass Measurement

There have been several studies about dynamical mass measurements of galaxy clusters based on stacking analysis (Munari et al. 2013; Farahi et al. 2016). An advantage of the stacking approach is that we can derive an accurate average mass of a sample of galaxy clusters, which is crucial in the era of wide-field surveys in which a large sample of galaxy clusters can be constructed. In this Chapter, we review previous studies of dynamical mass measurements using the stacking approach.

We can obtain information on the gravitational potential of a cluster, which depends on the mass of the cluster, from motions of galaxies. Therefore, we can measure masses of galaxy clusters by analyzing motions of galaxies in and around galaxy clusters. On the other hand, in  $N$ -body simulations, galaxy clusters correspond to dark matter halos. In this thesis, a cluster-scale dark matter halo whose dynamical mass is our main interest is referred to as a host-halo, whereas a galaxy-scale dark matter halo and subhalo in and around the cluster-scale dark matter halo are referred to as a satellite-halo and a sub-halo, respectively. We give more strict definition of the host-halo, satellite-halo, and sub-halo in Chapter 4.

The outline of the measurement of dynamical masses of stacked galaxy clusters are as follows. First, we calculate pairwise line-of-sight velocities ( $v_{\text{los}}$ ) between host-halos (clusters) and satellite-halos and sub-halos (galaxies). Because galaxy clusters are located far away from us, we cannot measure motions perpendicular to the celestial sphere. Hence, all we can observe are line-of-sight velocities. Second, we stack galaxy clusters to construct the  $v_{\text{los}}$  histogram. Because each galaxy cluster has only 50-100 observable satellite-halos and sub-halos at most, it is impossible to construct an accurate enough  $v_{\text{los}}$  histogram from a single cluster. Hence, we have to stack a lot of clusters for accurate dynamical mass measurements. Third, we reconstruct masses of galaxy clusters from  $v_{\text{los}}$  histograms. Since the relationships between masses of galaxy clusters and  $v_{\text{los}}$  histograms have not yet been fully understood, we usually estimate dynamical masses of galaxy clusters from  $v_{\text{los}}$  histograms by an empirical way using  $N$ -body simulation results. We review each step in this Chapter.

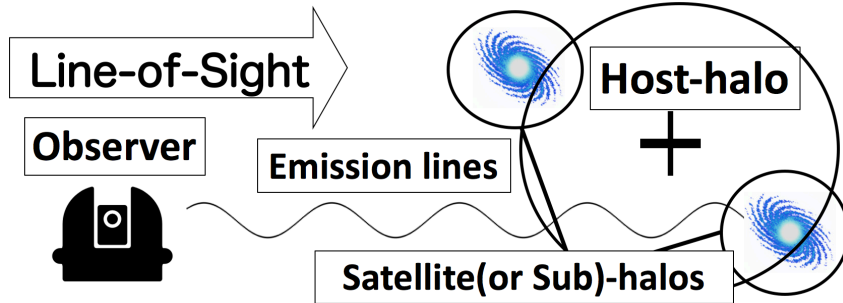


Figure 3.1: Rough illustration of  $v_{\text{los}}$  measurement

### 3.1 Measurement of $v_{\text{los}}$

In this Section, we review how to measure the line-of-sight velocity ( $v_{\text{los}}$ ) following to Farahi et al. (2016). They measure pairwise  $v_{\text{los}}$  between host-halos and satellite-halos and sub-halos by using galaxy redshifts. It is known that almost all galaxy clusters have large luminous galaxies at their centers. These galaxies are called Brightest Cluster Galaxies (BCG), whose positions are regarded as the centers of the galaxy clusters and whose velocities as bulk motion of galaxy clusters. The other galaxies in galaxy clusters are called satellite galaxies, whose positions and velocities are regarded as those of satellite-halos and sub-halos. We note that these are approximations and can generate systematic errors.

Fig. 3.1 shows a schematic picture of the configuration of the  $v_{\text{los}}$  measurement. For each pair of a cluster and a satellite galaxy, they calculate  $v_{\text{los}}$  by

$$v_{\text{los}} = c \left( \frac{z_{\text{sat}} - z_{\text{cen}}}{1 + z_{\text{cen}}} \right), \quad (3.1)$$

where  $z_{\text{cen}}$  is the redshift of the BCG, and  $z_{\text{sat}}$  is the redshift of the satellite galaxy. This  $v_{\text{los}}$  contains contributions from the Hubble flow and pairwise line-of-sight peculiar velocity. Specifically,  $v_{\text{los}}$  is given by

$$v_{\text{los}} = H \cdot d_{\text{los}} - (v_{\text{los:cen}} - v_{\text{los:sat}}), \quad (3.2)$$

where  $H$  is the Hubble parameter,  $d_{\text{los}}$  is the line-of-sight distance between the BCG and the satellite galaxy, and,  $v_{\text{los:cen}}$  and  $v_{\text{los:sat}}$  are the line-of-sight component of the peculiar velocity of the BCG and satellite galaxy, respectively.

The measurement error of  $v_{\text{los}}$  is

$$\Delta v_{\text{los}} = \sqrt{\left(\Delta z_{\text{sat}} \frac{1}{z_{\text{sat}} - z_{\text{cen}}}\right)^2 + \left\{\Delta z_{\text{cen}} \left(\frac{1}{1 + z_{\text{cen}}} + \frac{1}{z_{\text{sat}} - z_{\text{cen}}}\right)\right\}^2} \times v_{\text{los}} . \quad (3.3)$$

Since the typical value of  $v_{\text{los}}$  is 500 km/s, we have to measure redshifts as accurate as 500 km/s/ $c \sim 10^{-3}$ . In observations, the typical error of photometric redshifts is  $10^{-2}$ , whereas that of spectroscopic redshifts is  $10^{-4}$ . For this reason, we need to use spectroscopic galaxies to measure  $v_{\text{los}}$ .

## 3.2 Stacking Galaxy Clusters

For stacked  $v_{\text{los}}$  measurements, it is important to construct a large sample of galaxy clusters in order to reduce the error in the  $v_{\text{los}}$  histogram. In this Section, we review the main concept of red-sequence cluster finding methods (e.g., Rykoff et al. 2014; Oguri 2014).

It is known that a lot of galaxies in galaxy clusters follow a tight color-magnitude relationships. These galaxies are called red sequence galaxies. Fig. 3.2 is a color-magnitude diagram of the galaxy cluster Abell 22. The Figure indicates that many cluster member galaxies are populated along a line in the color-magnitude diagram. The tight red-sequence indicates that many cluster member galaxies were formed at a similar epoch.

This color-magnitude relation shows that a high density region of red and luminous galaxies must be associated with a galaxy cluster. Hence we can find galaxy clusters by finding such concentrations of red galaxies, and can also derive photometric redshifts of clusters from colors of the red-sequence.

In order to infer rough masses of galaxy clusters identified by the red-sequence methods, it is common to adopt richness, which is essentially the number of cluster member galaxies. For instance, Rykoff et al. (2014) define richness by the number of red cluster member galaxies with the projected radius of

$$R_{\lambda} = 1.0 h^{-1} \left(\frac{\lambda}{100}\right)^{0.2} \text{ Mpc}, \quad (3.4)$$

where  $\lambda$  is richness of a galaxy cluster. In Rykoff et al. (2014),  $\lambda$  and  $R_{\lambda}$  are computed iteratively, until they converge. We can expect that clusters with large richness are more massive on average, which is indeed confirmed by e.g., stacked weak lensing observations (e.g., Murata et al. 2017).

We review more details about CAMIRA (Oguri 2014), one of red-sequence cluster finding methods, in Appendix A.

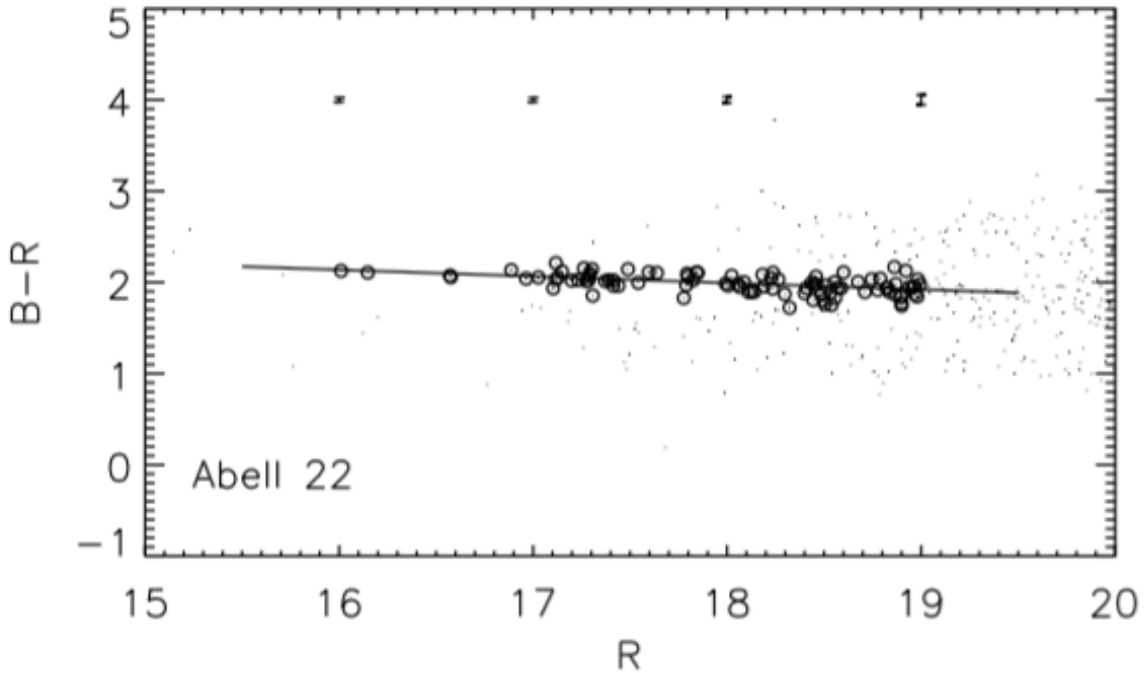


Figure 3.2: Color-magnitude diagram of the galaxy cluster Abell 22. The vertical axis is a galaxy color i.e., the difference between  $B$ -band and  $R$ -band magnitudes. The horizontal axis is the  $R$ -band magnitude. Points are galaxies. Points with circles shows color-magnitude relations of red cluster member galaxies. The solid line shows a fit to the red-sequence relation. Taken from Stott et al. (2009)

### 3.3 Reconstruction of Masses of Galaxy Clusters from $v_{\text{los}}$ Histograms

Now, we can construct the  $v_{\text{los}}$  histogram by stacking a lot of galaxy clusters. We discuss how we obtain masses of galaxy clusters from the  $v_{\text{los}}$  histogram. Here, we introduce previous studies based on Munari et al. (2013) and Rozo et al. (2015).

In those papers, all galaxies within  $r_{\text{proj}} < R_{\lambda}$  are used to construct the  $v_{\text{los}}$  histogram, where  $r_{\text{proj}}$  is the projected radius, and  $R_{\lambda}$  is defined in eq. (3.4).

The  $v_{\text{los}}$  histogram is fitted to the following function form

$$f(v_{\text{los}}) = \frac{A_0}{\sqrt{2\pi\sigma_G^2}} \exp\left(-\frac{v_{\text{los}}^2}{2\sigma_G^2}\right) + A_1. \quad (3.5)$$

The first term corresponds to signals from cluster member galaxies, and the second term of eq. (3.5) corresponds to contributions from foreground and background galaxies of galaxy clusters, i.e., field galaxies. Because the distribution of cluster member galaxies is highly elongated along the line-of-sight in the redshift space, it is difficult to separate cluster member galaxies from other galaxies on an individual basis, which is why we have

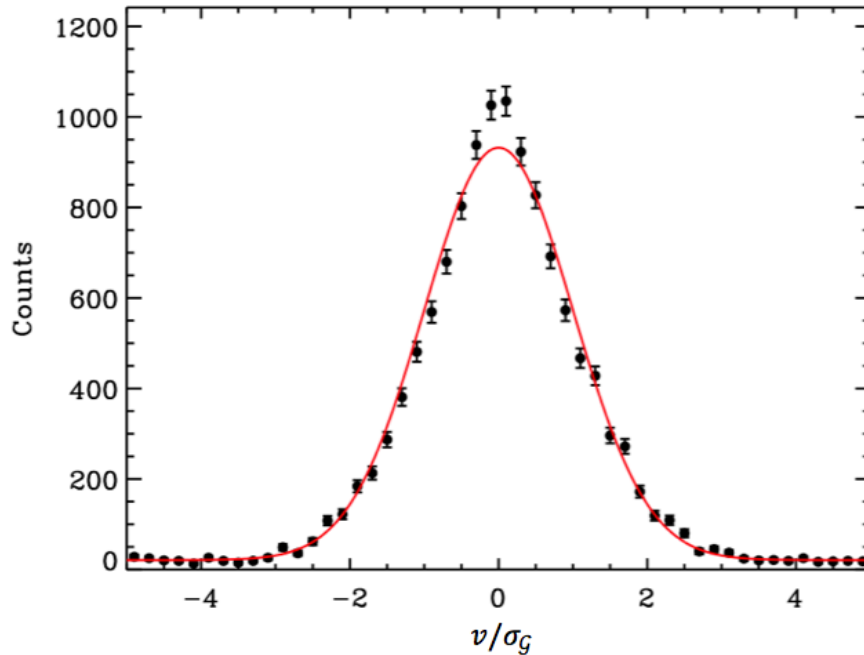


Figure 3.3: Distribution of  $v_{\text{los}}$ . The black points are from mock observations of an  $N$ -body simulation, and the solid line is the best fit of eq. (3.5). Taken from Rozo et al. (2015)

to subtract the contributions from the foreground and background galaxies statistically.

The fitting range may affect results. At first fitting, they set the fitting range to

$$|v_{\text{los}}| \leq 3000 \times (\lambda/20)^{0.45} \text{ km/s} . \quad (3.6)$$

After deriving  $\sigma_{\mathcal{G}}$ , they change the fitting range to

$$|v_{\text{los}}| \leq 5\sigma_{\mathcal{G}} \quad (3.7)$$

and re-fit the histogram. This process is repeated until it converges. Fig. 3.3 is an example of the  $v_{\text{los}}$  distribution and the fitting result. We can see that their model is generally good, but not perfect. For example, the model cannot reproduce the sharp peak around  $v_{\text{los}} = 0$ .

Free parameters in eq. (3.5) are  $A_0$ ,  $A_1$ , and  $\sigma_{\mathcal{G}}$ , where  $A_0$  and  $A_1$  are parameters to determine the ratio of the number of field galaxies to that of cluster member galaxies. Moreover,  $\sigma_{\mathcal{G}}$  is the "velocity dispersion" of galaxy clusters. In Munari et al. (2013), by using  $N$ -body simulation, they show that the cluster mass is inferred from the one-dimensional velocity dispersion ( $\sigma_{1\text{D}}$ ) as

$$\sigma_{1\text{D}} = A_2 \left( \frac{h(z) M_{200}}{10^{15} M_{\odot}} \right)^{\alpha} , \quad (3.8)$$

where,  $A_2$  and  $\alpha$  are fitting parameters,  $M_{200}$  is the mass within a sphere of radius  $r_{200}$ , and  $r_{200}$  is the radius that the density of a spherical region within  $r_{200}$  being equal to 200 times the critical density of the Universe  $\rho_{\text{crit}}$ . The parameter  $h(z)$  is the dimensionless Hubble parameter defined as

$$h(z) \equiv \frac{H(z)}{100 \text{ (km/s/Mpc)}}. \quad (3.9)$$

In the  $N$ -body simulation,  $\sigma_{1D}$  is defined as

$$\sigma_{1D} = \sqrt{\frac{1}{3N_{\text{sat}}} \sum_i^{N_{\text{sat}}} |\mathbf{v}_{\text{cluster}} - \mathbf{v}_{i,\text{sat}}|^2}, \quad (3.10)$$

where  $\mathbf{v}_{\text{cluster}}$  is the velocity of the center of galaxy cluster,  $\mathbf{v}_{i,\text{sat}}$  is the velocity of the  $i$ -th satellite-halo, and  $N_{\text{sat}}$  is the number of satellite halos. While we can infer the mean cluster mass from the stacked  $v_{\text{los}}$  diagram once we regard  $\sigma_{1D}$  and  $\sigma_{\mathcal{G}}$  as the same, there are several notable differences between these two parameters. First,  $\sigma_{1D}$  is calculated directly from the pairwise velocity rather than by fitting eq. (3.5) to the histogram. Second,  $\sigma_{1D}$  assumes an isotropic pairwise velocity distribution, whereas  $\sigma_{\mathcal{G}}$  does not rely on such an assumption. Third, the one-dimensional pairwise velocity derived in Munari et al. (2013) does not contain the Hubble flow. Forth, in Munari et al. (2013), only sub-halos within  $r_{200}$  are used to calculate  $\sigma_{1D}$ . These differences must cause the difference between  $\sigma_{1D}$  and  $\sigma_{\mathcal{G}}$ , which is neglected here. If satellite-halos and sub-halos are well relaxed and virialized within the cluster,  $A_2 = 1040 - 1140$  km/s, and  $\alpha = 1/3$  are expected (see also Section 2.1).

In Fig. 3.4, they show the relationships between  $\sigma_{1D}$  and galaxy cluster mass  $M_{200}$ . We can see that there is a difference between the best fit line and the virialized line.

If we regard  $\sigma_{1D}$  as the same parameter as  $\sigma_{\mathcal{G}}$ , we can estimate masses of galaxy clusters from  $v_{\text{los}}$  histograms by using eqs. (3.5) and (3.8). However, they are in fact different with each other as we will explicitly show in Appendix B from the analysis of our simulation.

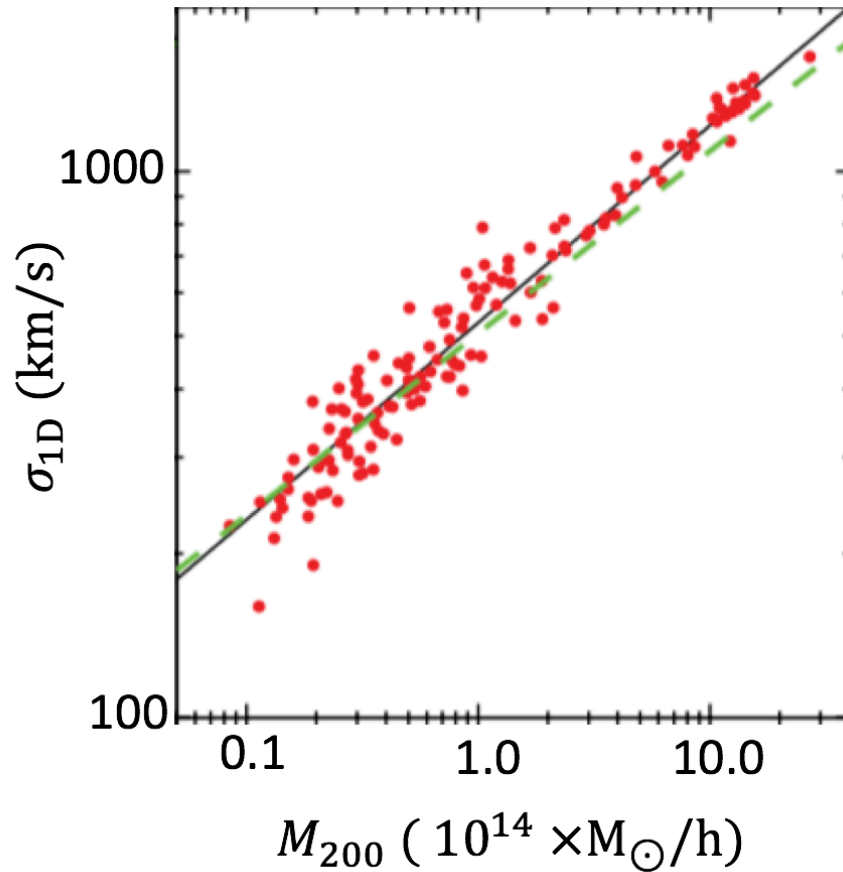


Figure 3.4: Comparison between cluster masses ( $M_{200}$ ) and velocity dispersions of dark matter halos ( $\sigma_{1D}$ ) taken from Munari et al. (2013). Filled circles are from mock observations, whereas the solid line is the best fit line of eq. (3.8), and the dashed line is the line that corresponds to the "virialized line",  $A_2 = 1095 \text{ km/s}$  and  $\alpha = 0.336$  for comparison. The best fit parameters of the solid line are  $A_2 = 1199 \pm 5.2 \text{ km/s}$  and  $\alpha = 0.365 \pm 0.0017$ .



# Chapter 4

## Modeling the Phase Space Distribution of Dark Matter Halos

To estimate cluster masses from the  $v_{\text{los}}$  histogram, we usually assume some model function of the  $v_{\text{los}}$  histogram like eq. (3.5). When we construct some model of  $v_{\text{los}}$  histogram, we usually make simplified assumptions about satellite-halos or sub-halos. For example, eq. (3.5) assumes that motions of satellite-halos and sub-halos are virialized, and foreground and background halos distribute uniformly in phase space. However, motions of massive satellite-halos and sub-halos ( $M_{\text{vir}} > 10^{11} M_{\odot}$ ) are not virialized even at present time, where,  $M_{\text{vir}}$  is defined in the same way as  $M_{200}$ , but using the overdensity of  $\Delta_{\text{vir}} (= 18\pi^2 \sim 178) \times \rho_{\text{crit}}$ .

Fig. 4.1 shows the stacked phase space distribution of dark matter halos in our  $N$ -body simulation at  $z = 0$  (see Section 4.1 for more details). We can clearly see that a significant fraction of satellite-halos and sub-halos are infalling to galaxy clusters, and a small fraction of halos are virialized even at  $z = 0$ .

As we can see in Fig. 4.1, the phase space distribution of dark matter halos is quite complicated. There are some studies which propose realistic model of the phase space distribution of dark matter halos. For example, Scoccimarro (2004) and Lam et al. (2013) proposed based on the so-called halo model, and Zu & Weinberg (2013) constructed a model in a phenomenological way. However these models still do not fully reproduce the complex phase space distribution of dark matter halos seen in  $N$ -body simulations even though it is necessary to fully exploit the  $v_{\text{los}}$  histograms for cluster mass measurements. This is why in this thesis we construct a new model of the phase space distribution of dark matter halos in a phenomenological way.

The features of our new model are; 1) we adopt a new model function of the phase space distribution. 2) we divide dark matter halos into two components, the infall component and the splashback component, and describe the phase space distributions separately.

In this Chapter, we present our model, which is calibrated against  $N$ -body simulations.

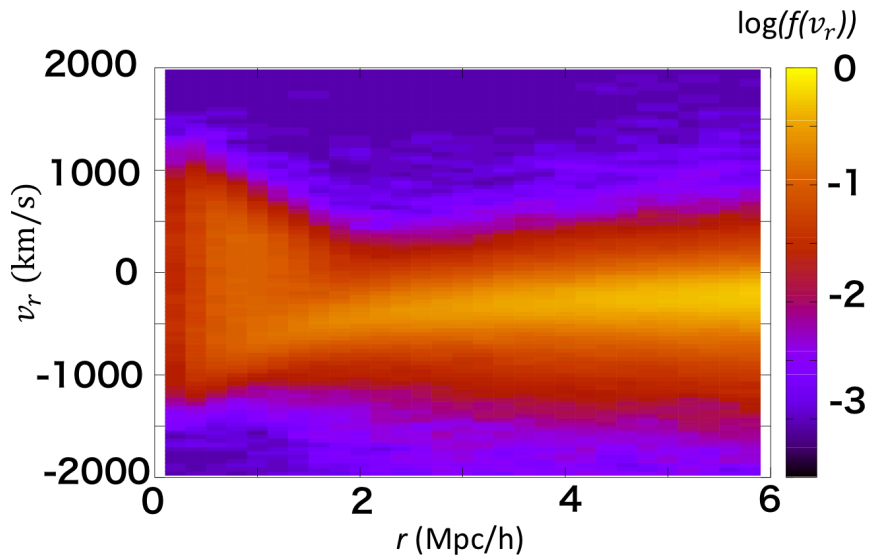


Figure 4.1: The stacked phase space distribution of dark matter halos in our  $N$ -body simulation at  $z = 0$ . Only massive satellite-halos and sub-halos ( $M_{\text{vir}} > 10^{11} M_{\odot}$ ) are used. The mass range of host halos (clusters) is  $10^{14} M_{\odot} < M_{\text{vir}} < 2 \times 10^{14} M_{\odot}$ . The vertical axis is the radial velocity of dark matter halos, which is defined such that positive  $v_r$  corresponds to outward motions. The horizontal axis is the radius from the centers of galaxy clusters. The color scale shows the number density of halos in the phase space,  $\log f(v_r)$  which is defined as the number density per each galaxy cluster with bin sizes of 40 km/s for  $v_r$  bin, 0.2 Mpc/ $h$  for  $r$  bin.

## 4.1 Phase Space Distribution of Halos from $N$ -body Simulation

First, we perform a cosmological  $N$ -body simulation. The simulation is performed with TreePM code `Gadget-2` (Springel 2005), which runs from  $z = 99$  to  $z = 0$  in a box of comoving  $360 \text{ Mpc}/h$  on a side with periodic boundary condition. The number of dark matter particles is  $1024^3$ , corresponding to the mass of each particle of  $m_p = 3.4 \times 10^9 M_\odot/h$ . The gravitational softening length is fixed at comoving  $20 \text{ kpc}/h$ . The initial condition is generated by the `MUSIC` code (Hahn & Abel 2011), which employs second order Lagrangian perturbation theory. The transfer function at  $z = 99$  is generated by the linear Boltzman code `CAMB` (Lewis et al. 2000). We adopt  $\Omega_{M,0} = 0.279$ ,  $\Omega_{\Lambda,0} = 0.721$ ,  $h = 0.7$ ,  $n_s = 0.972$ ,  $\sigma_8 = 0.821$  following the WMAP 9 year result (Hinshaw et al. 2013). To identify halos and sub-halos in our simulation, we use 6-dimension friend of friend (FoF) algorithm implemented in `Rockstar` (Behroozi et al. 2013b).

We use this simulation to obtain the phase space distribution of dark matter halos around galaxy clusters. Because we are interested in statistical features of dynamics of dark matter halos, we stack a lot of simulated galaxy clusters to derive accurate phase space distributions as shown in Fig. 4.1. In this thesis, we adopt dark matter halos that are more massive than  $5 \times 10^{13} M_\odot$  as galaxy clusters. We divide these galaxy clusters into three mass bins, low mass bin ( $5 \times 10^{13} M_\odot < M_{\text{vir}} < 10^{14} M_\odot$ ), middle ( $10^{14} M_\odot < M_{\text{vir}} < 2 \times 10^{14} M_\odot$ ), and high ( $2 \times 10^{14} M_\odot < M_{\text{vir}} < 5 \times 10^{14} M_\odot$ ). In our simulation, each bin contains 2082 (low), 1238 (middle), and 490 (high) galaxy clusters. To mimic observations, we remove galaxy clusters if there are any other clusters with larger masses within  $1 \text{ Mpc}/h$  from those clusters.

We use halos with masses  $M_{\text{vir}} > 10^{11} M_\odot$  as satellite-halos and sub-halos. We define sub-halos following the definition of the `Rockstar` algorithm (Behroozi et al. 2013b). We also define satellite-halos as halos excluding the galaxy cluster of interest. In brief, sub-halos are defined as substructures of halos. Note that galaxy clusters can become satellite-halos when we focus on other galaxy clusters. We use only  $z = 0$  snapshot in this thesis for simplicity. In Fig. 4.2, we show the mass distribution of all dark matter halos in our simulation. We can see that halo mass distribution of our simulation is smooth.

## 4.2 Overview of Our Model

We construct a model of the phase space distribution of satellite-halos and sub-halos surrounding galaxy clusters based on the stacked phase space distribution of the  $N$ -body simulation. Because we stack a lot of galaxy clusters without aligning their orientations, the spherical asymmetry of the phase space distribution should be damped. Hence, we assume a spherically symmetric phase space distribution.

We divide velocity into three orthogonal components, the radial velocity ( $v_r$ ) and two tangential velocities ( $v_{t,1}$ ,  $v_{t,2}$ ) as shown in Fig. 4.3. At this point we consider peculiar

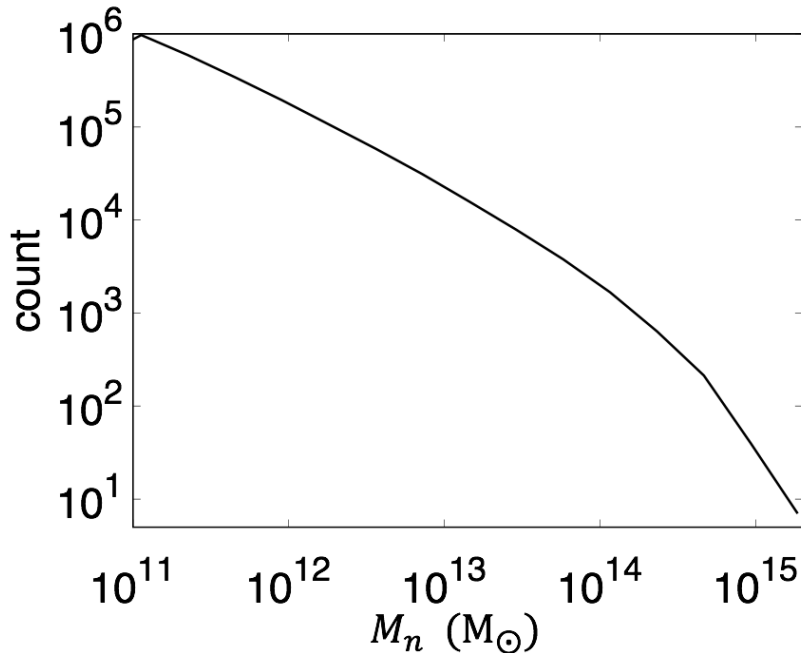


Figure 4.2: Mass distribution of halos in our simulation at  $z = 0$ . The  $n$ -th Mass bin is defined as  $(1/\sqrt{2})M_n < M_{\text{vir}} < \sqrt{2}M_n$ .

velocities only and do not consider the Hubble flow. Since one of the two components of the tangential velocities do not contribute to  $v_{\text{los}}$ , we neglect  $v_{t,2}$  in this thesis, and denote  $v_{t,1}$  as  $v_t$ .

Under the assumption of the spherically symmetric phase space distribution, we can describe the probability distribution function (PDF) of the phase space as

$$p_v = p_v(v_r, v_t, r) . \quad (4.1)$$

We then assume that the PDF of the phase space distribution can be divided into two components, the infall component and the splashback component. The infall component corresponds to dark matter halos that are now falling into galaxy clusters, and the splashback component corresponds to halos that are on their first orbit after falling into galaxy clusters. Such two components model is also proposed in Zu & Weinberg (2013), but they consider a virial component instead of the splashback component. Then, eq. (4.1) is described as

$$p_v(v_r, v_t, r) = (1 - \alpha)p_{\text{infall}}(v_r, v_t, r) + \alpha p_{\text{SB}}(v_r, v_t, r), \quad (4.2)$$

where  $\alpha$  is the fraction of the splashback component at given  $r$ . For simplicity, we also assume that there is no correlation between radial and tangential velocities. Then, we can describe eq. (4.2) as

$$p_v(v_r, v_t, r) = (1 - \alpha)p_{v_r, \text{infall}}(v_r, r)p_{v_t, \text{infall}}(v_t, r) + \alpha p_{v_r, \text{SB}}(v_r, r)p_{v_t, \text{SB}}(v_t, r) . \quad (4.3)$$

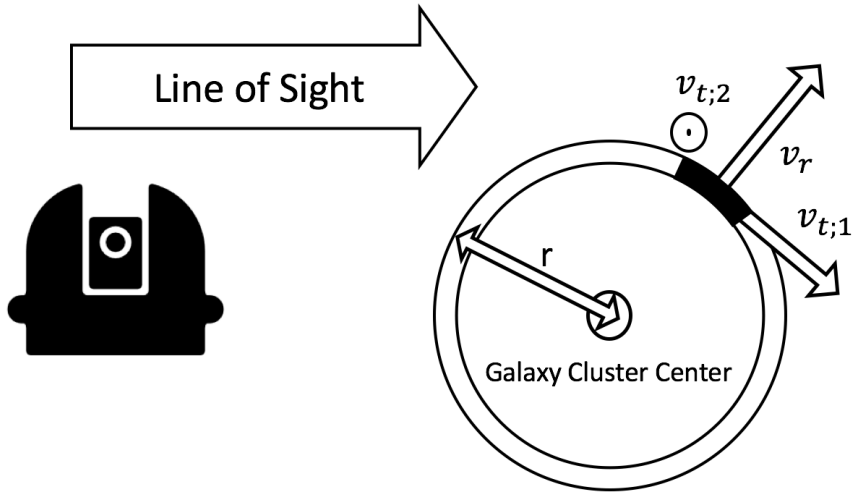


Figure 4.3: Our definition of three velocity components.

We check the correlation between radial and tangential velocities in Section 4.6.

In the next Sections, we present models of individual distributions included in eq. (4.3). In Section 4.3 (Section 4.4), we show the model function of the radial (tangential) velocity phase space distribution and show the best fit parameters for each radial bin. In Section 4.5, we show the radial dependence of parameters used in our model of the phase space distribution, and fit the dependence with smooth functions of the radius. In Section 4.6, we derive the PDF of  $v_{\text{los}}$  by projecting the phase space distribution along the line-of-sight including the effect of the Hubble flow.

### 4.3 Radial Velocity Distribution

In this Section, we present the function forms of  $p_{v_r, \text{infall}}$  and  $p_{v_r, \text{SB}}$  and determine model parameters by fitting the model functions to the phase space distributions in the  $N$ -body simulation.

First, we divide the phase space distribution into radial bins and make histograms of radial peculiar velocities of satellite-halos and sub-halos for each radial bin, for each cluster mass bin. The width of the radial bin is  $0.2 \text{ Mpc}/h$ .

As we show in Fig. 4.4, we find that the radial velocity distributions at large radii, where the distributions are dominated by the infall component, significantly deviate from the Gaussian distribution. There are non-negligible skewness and kurtosis in the radial velocity distribution, as was already shown in Scoccimarro (2004). To incorporate the skewness and kurtosis, we adopt the Johnson's SU-distribution (Johnson 1949) as the model function for the radial velocity distribution of the infall component.

$$\begin{aligned}
 p_{v_r, \text{infall}}(v_r, r) &= SU(v_r; \delta, \lambda, \gamma, \xi) \\
 &= \frac{\delta}{\lambda \sqrt{2\pi} \sqrt{\{z(v_r)\}^2 + 1}} \exp \left[ -\frac{1}{2} \{ \gamma + \delta \sinh^{-1} z(v_r) \} \right], \quad (4.4)
 \end{aligned}$$

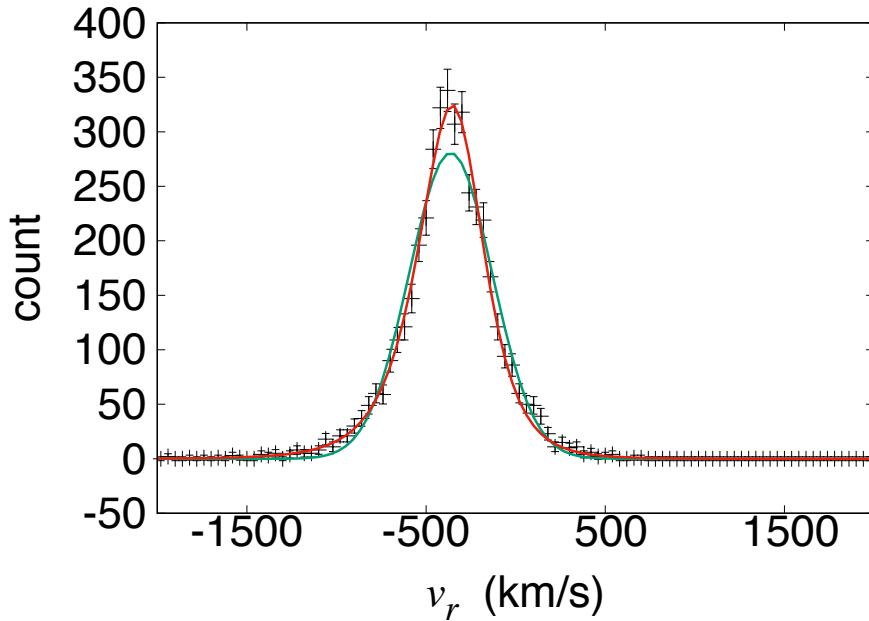


Figure 4.4: Stacked radial velocity distribution at  $2.6 \text{ Mpc}/h < r < 2.8 \text{ Mpc}/h$  for the middle galaxy cluster mass bin. Points with error bars are the histogram of radial velocities from our simulation, the red line is the best fit line of eq. (4.4), and the green line is the best fit line of the Gaussian distribution for comparison. Error bars show the Poisson errors.  $\chi^2/\text{dof} = 0.47$  for the SU-distribution, and  $\chi^2/\text{dof} = 1.37$  for the Gaussian distribution.

where

$$z(v_r) = \frac{v_r - \xi}{\lambda}, \quad (4.5)$$

and  $v_r$  is the radial peculiar velocity of each dark matter halo. The Johnson's SU-distribution has four free parameters, and can reproduce skewness and kurtosis of histograms. Note that these four parameters,  $\delta, \lambda, \gamma$ , and  $\xi$  are functions of the radius  $r$ . Fig. 4.4 shows the radial velocity distribution at  $2.6 \text{ Mpc}/h < r < 2.8 \text{ Mpc}/h$  for the middle galaxy cluster mass bin. We can see that the Johnson's SU-distribution is in better agreement with the histogram than the Gaussian distribution. Note that at large  $r$ , the splashback component must vanish i.e.,  $\alpha = 0$  at large  $r$ .

Fig. 4.5 shows the radial velocity distributions at radii larger than  $2.8 \text{ Mpc}/h$  for the middle galaxy cluster mass bin. We can see that the Johnson's SU-distribution is in good agreement with the histogram even at larger radii.

At small  $r$ , there are two peaks in histograms of radial velocities, reflecting the two distinct components as assumed in our model (see Fig. 4.6). As shown in Section 4.2, we add the splashback term to eq. (4.4) to reproduce the double peak feature. The model function we adopt for  $p_{v_r, \text{SB}}$  is the Gaussian distribution. Hence, at small  $r$ ,  $p_{v_r}$  is

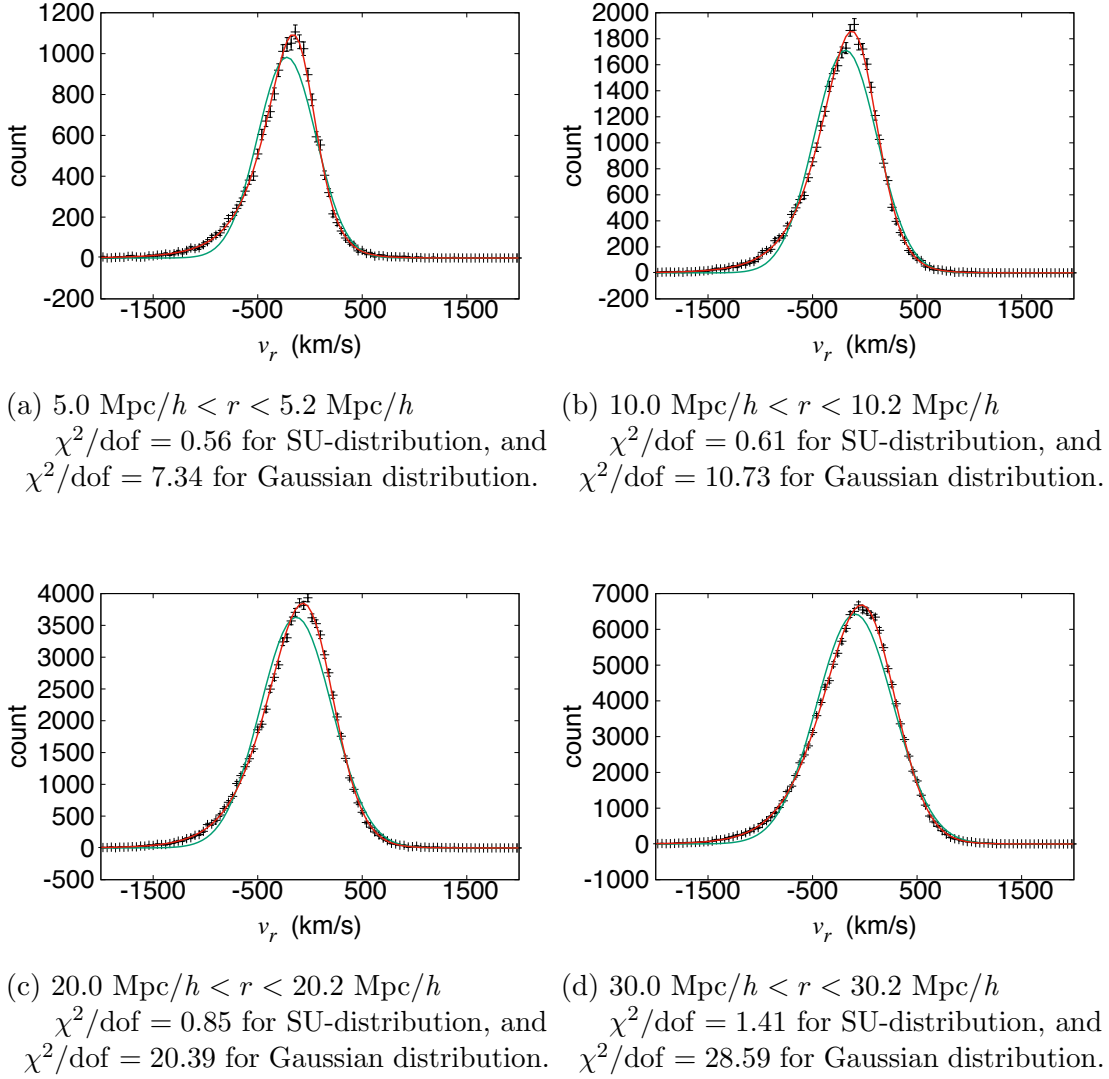


Figure 4.5: Same as Fig. 4.4, but for radii larger than  $2.8 \text{ Mpc}/h$ .

described as

$$p_{v_r}(v_r; \alpha, \delta, \lambda, \gamma, \xi, \mu_r, \sigma_r) = (1 - \alpha)SU(v_r; \delta, \lambda, \gamma, \xi) + \alpha G(v_r; \mu_r, \sigma_r^2), \quad (4.6)$$

where  $G(v_r; \mu_r, \sigma_r^2)$  is the Gaussian distribution.

$$G(v_r; \mu_r, \sigma_r^2) = \frac{1}{\sqrt{2\pi\sigma_r^2}} \exp\left\{-\frac{(v_r - \mu_r)^2}{2\sigma_r^2}\right\}, \quad (4.7)$$

Note that  $\mu_r$  and  $\sigma_r^2$  are functions of  $r$ . The physical meaning of the first term of the right side hand of eq. (4.6) is the infall component of the phase space distribution, whereas the second term of the right side hand of eq. (4.6) is the splashback component. At large  $r$ ,  $\alpha$  goes to zero and eq. (4.6) is reduces to eq. (4.4). In Zu & Weinberg (2013), they adopted

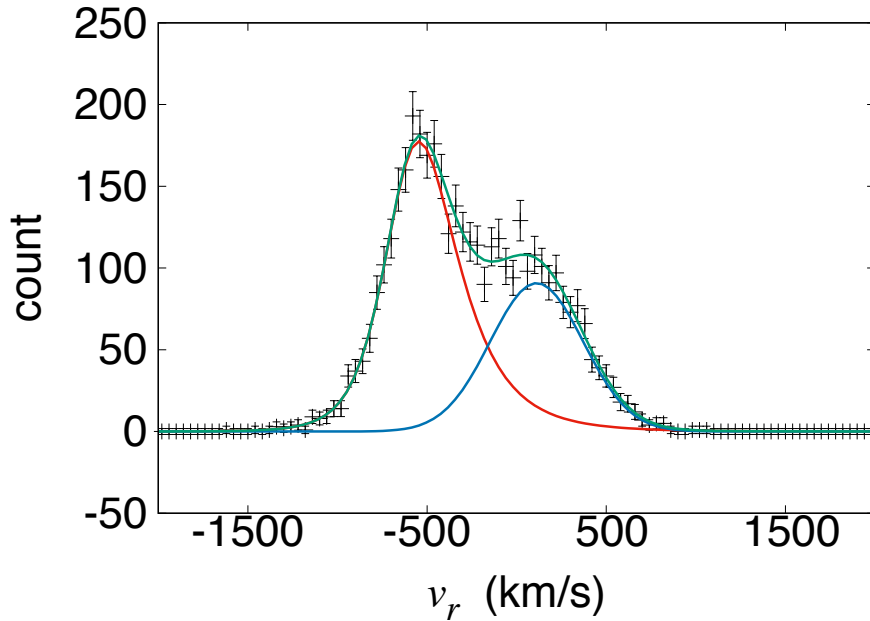
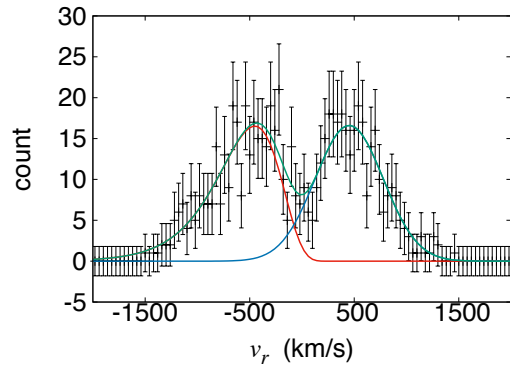


Figure 4.6: The radial velocity distribution at  $1.2 \text{ Mpc}/h < r < 1.4 \text{ Mpc}/h$  for the middle galaxy cluster mass bin. Points with error bars are the histogram of radial velocities from our simulation, the red line is the best fit line of the first term of the right side hand of eq. (4.6) i.e. the infall component, the blue line is the best fit line of the second term of the right side hand of eq. (4.6) i.e. the splashback component, and the green line is the sum of the red and blue lines.  $\chi^2/\text{dof} = 0.38$

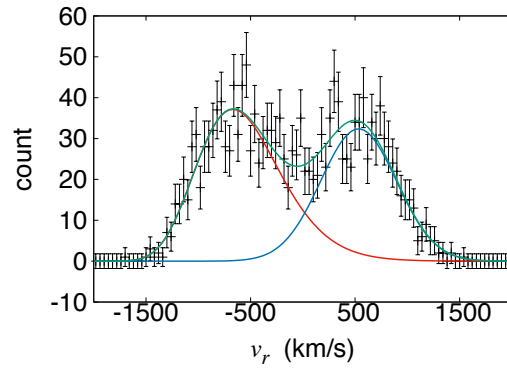
two component model that consists of the infall and virial components. While the mean velocity of the virial component is always set to zero, the mean velocity of the splashback component is allowed to deviate from zero and is regarded as a model parameter. This is one of the main differences between our model and the model proposed in Zu & Weinberg (2013). As a result, our model is in better agreement with the radial velocity distribution of simulated dark matter halos at  $r < 1.0 \text{ Mpc}/h$ , than the model of Zu & Weinberg (2013) as shown in Fig. 4.6 and Fig. 4.7.

In Fig. 4.6, we show the radial velocity distribution at  $1.2 \text{ Mpc}/h < r < 1.4 \text{ Mpc}/h$  for the middle galaxy cluster mass bin. We can see that our model function of eq. (4.6) is in good agreement with the histogram.

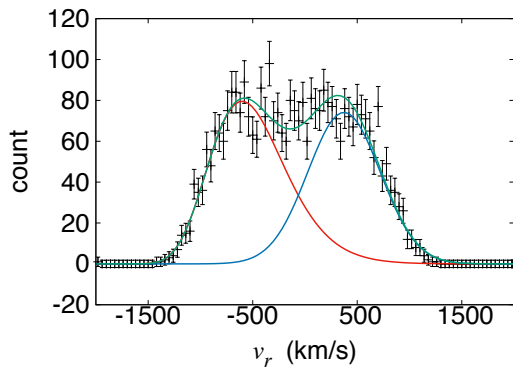
Fig. 4.7 shows the radial velocity distribution at small  $r$  other than  $1.2 \text{ Mpc}/h < r < 1.4 \text{ Mpc}/h$  for the middle galaxy cluster mass bin. We can see that eq. (4.6) is in good agreement with the histogram even at other  $r$ .



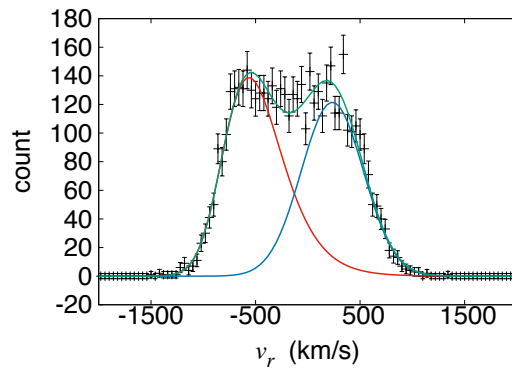
(a)  $0 \text{ Mpc}/h < r < 0.2 \text{ Mpc}/h$   
 $\chi^2/\text{dof} = 0.45$



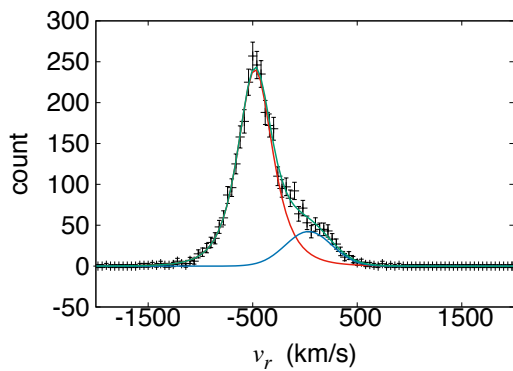
(b)  $0.2 \text{ Mpc}/h < r < 0.4 \text{ Mpc}/h$   
 $\chi^2/\text{dof} = 0.74$



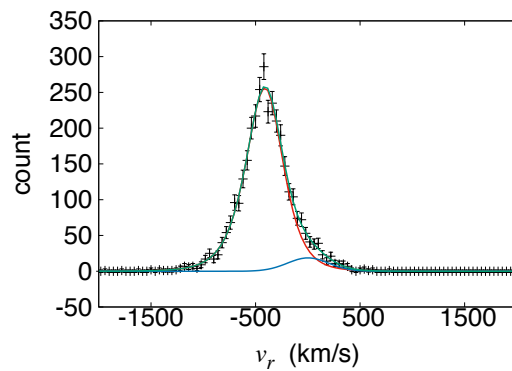
(c)  $0.4 \text{ Mpc}/h < r < 0.6 \text{ Mpc}/h$   
 $\chi^2/\text{dof} = 0.81$



(d)  $0.8 \text{ Mpc}/h < r < 1.0 \text{ Mpc}/h$   
 $\chi^2/\text{dof} = 0.73$



(e)  $1.6 \text{ Mpc}/h < r < 1.8 \text{ Mpc}/h$   
 $\chi^2/\text{dof} = 0.42$



(f)  $2.0 \text{ Mpc}/h < r < 2.2 \text{ Mpc}/h$   
 $\chi^2/\text{dof} = 0.43$

Figure 4.7: Same as Fig. 4.6, but for small  $r$  other than  $1.2 \text{ Mpc}/h < r < 1.4 \text{ Mpc}/h$ .

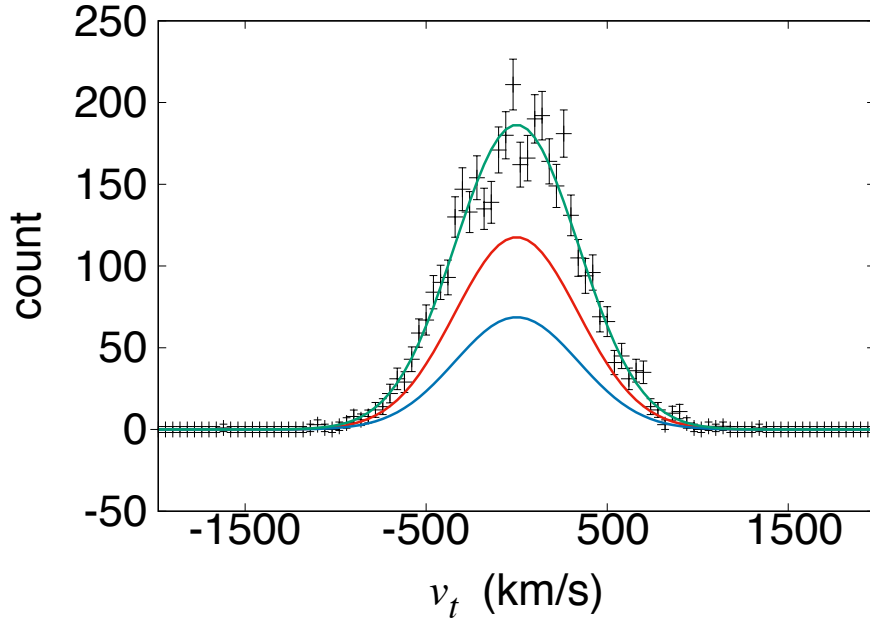


Figure 4.8: Same as Fig. 4.6, but for the tangential velocity. We use eq. (4.8) instead of eq. (4.6).  $\chi^2/\text{dof} = 0.66$

## 4.4 Tangential Velocity Distribution

Next, we derive the tangential velocity distribution. The model function for  $p_{v_t, \text{infall}}$  and  $p_{v_t, \text{SB}}$  are assumed to be the Gaussian distribution function. Specifically,  $p_{v_t}$  is described as

$$p_{v_t}(v_t; \alpha, \sigma_{t, \text{infall}}^2, \sigma_{t, \text{SB}}^2) = (1 - \alpha) \frac{1}{\sqrt{2\pi\sigma_{t, \text{infall}}^2}} \exp\left(-\frac{v_t^2}{2\sigma_{t, \text{infall}}^2}\right) + \alpha \frac{1}{\sqrt{2\pi\sigma_{t, \text{SB}}^2}} \exp\left(-\frac{v_t^2}{2\sigma_{t, \text{SB}}^2}\right). \quad (4.8)$$

Since we assume the spherically symmetric phase space distribution, the mean of  $v_t$  must be zero. In eq. (4.8) we use  $\alpha(r)$  calculated in eq. (4.6). Hence, we have only two parameters in eq. (4.8).

In Fig. 4.8, we show the tangential velocity distribution at  $1.2 \text{ Mpc}/h < r < 1.4 \text{ Mpc}/h$  for the middle galaxy cluster mass bin. We can see that our model function eq. (4.8) is in good agreement with the histogram.

Fig. 4.9 shows the tangential velocity distribution at small radii other than  $1.2 \text{ Mpc}/h < r < 1.4 \text{ Mpc}/h$  for the middle galaxy cluster mass bin. We can see that eq. (4.8) is in good agreement with the histogram even at other small radii.

Fig. 4.10 shows the tangential velocity distribution at larger radii for the middle galaxy cluster mass bin. Unlike the radial velocity, the Gaussian distribution is in good

agreement with the histograms at larger radii for the tangential velocities. However at large radii, we can see that the histograms of tangential velocities from our simulation show slightly non-zero kurtosis, and cause worse  $\chi^2/\text{dof}$ .

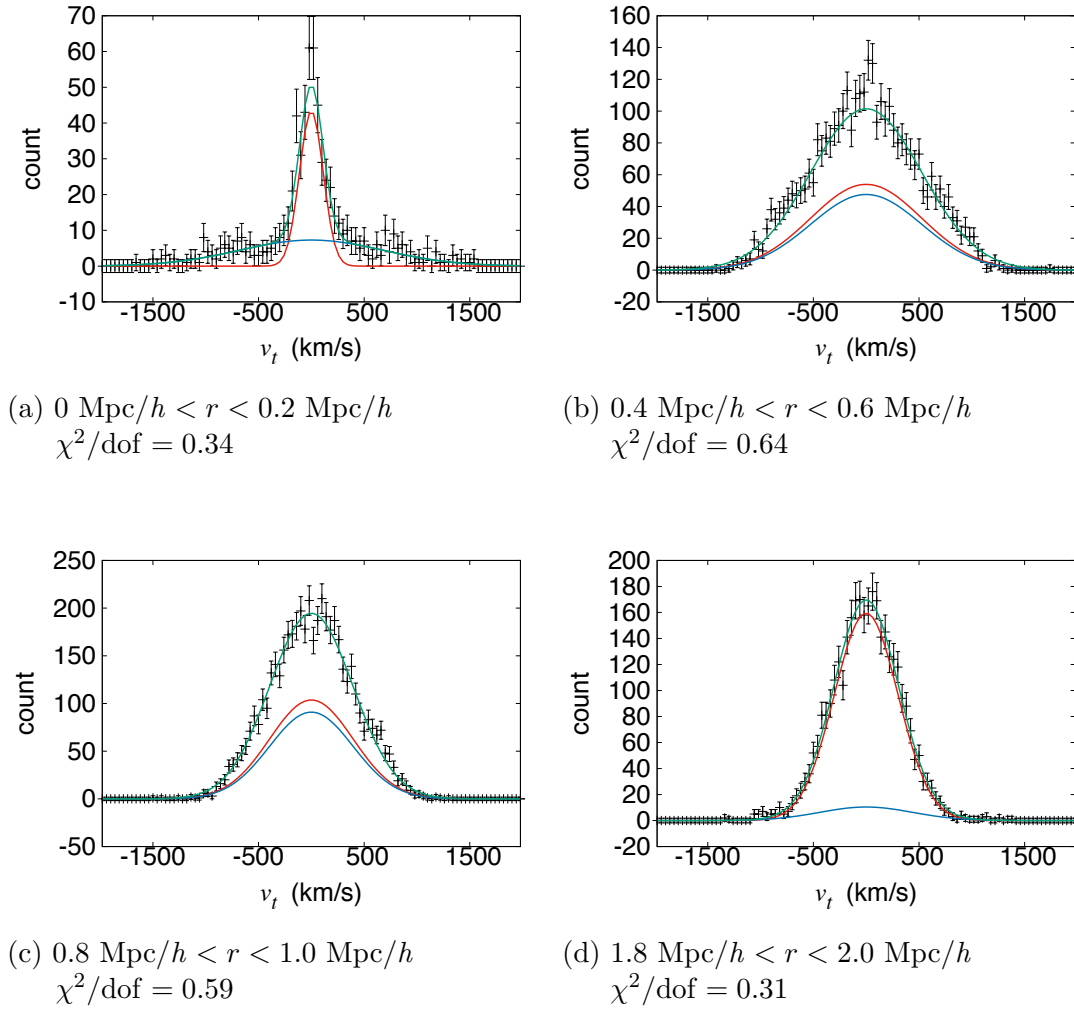
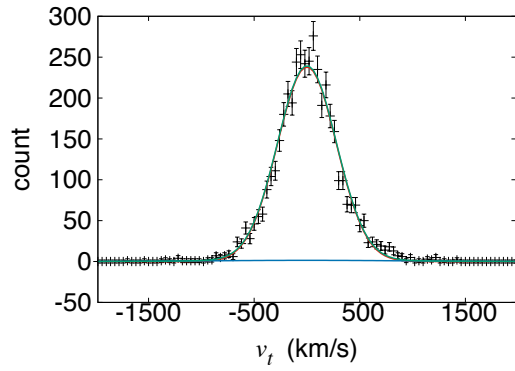
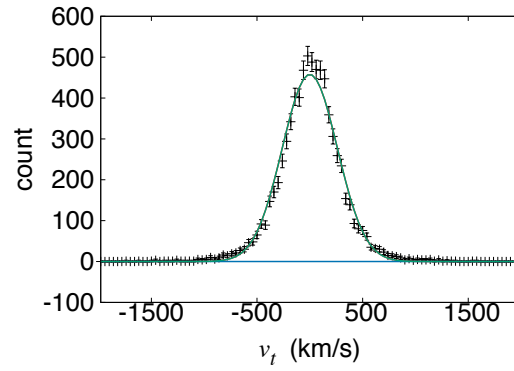


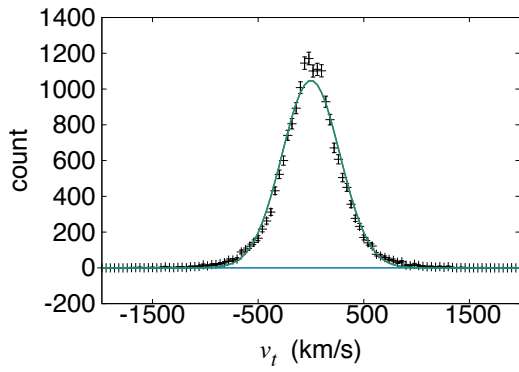
Figure 4.9: Same as Fig. 4.8, but for small  $r$  other than  $1.2 \text{ Mpc}/h < r < 1.4 \text{ Mpc}/h$ .



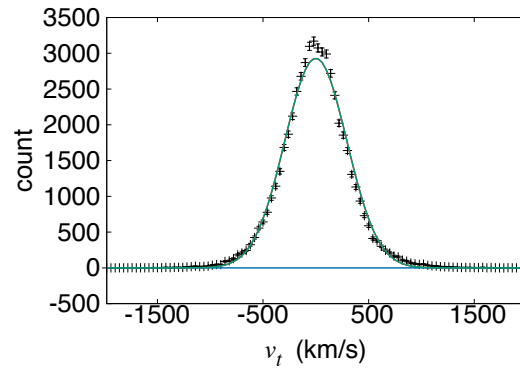
(a)  $2.6 \text{ Mpc}/h < r < 2.8 \text{ Mpc}/h$   
 $\chi^2/\text{dof} = 0.99$



(b)  $5.0 \text{ Mpc}/h < r < 5.2 \text{ Mpc}/h$   
 $\chi^2/\text{dof} = 1.73$



(c)  $10.0 \text{ Mpc}/h < r < 10.2 \text{ Mpc}/h$   
 $\chi^2/\text{dof} = 3.51$



(d)  $20.0 \text{ Mpc}/h < r < 20.2 \text{ Mpc}/h$   
 $\chi^2/\text{dof} = 6.18$

Figure 4.10: Same as Fig. 4.8, but for larger radii than  $1.4 \text{ Mpc}/h$ .

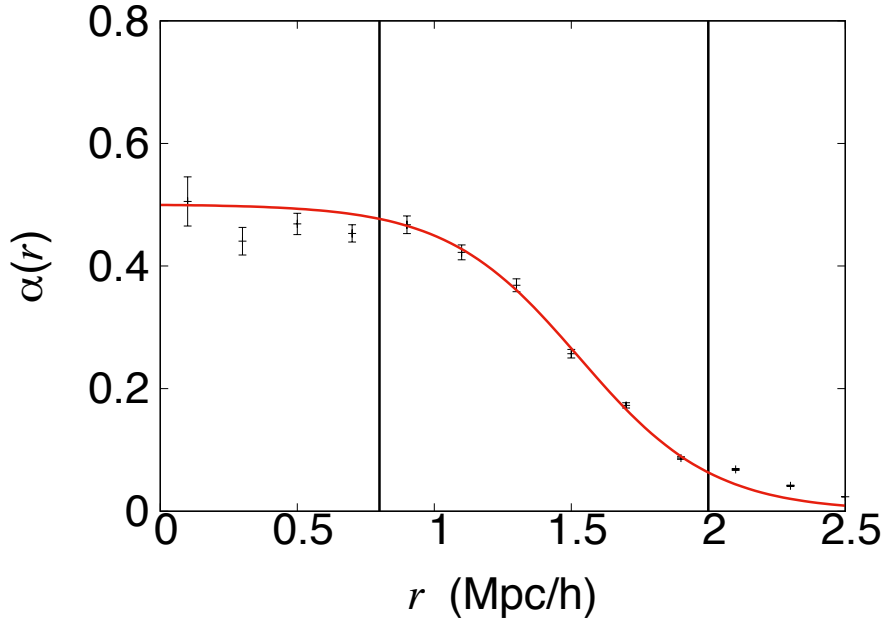


Figure 4.11: Radial distribution of  $\alpha(r)$  for the middle galaxy cluster mass bin. Points with error bars are  $\alpha(r)$  calculated by fitting eq. (4.6) to radial velocity distributions, and the solid line is the best fit line of eq. (4.9). The vertical lines show the upper and lower limits of the fitting range.

## 4.5 Radial Dependence of Parameters in The Model

In previous Sections, we adopt nine parameters to model the phase space probability distribution for each radial bin. To construct a full phase space PDF, we have to describe these parameters as a smooth function of  $r$ .

For  $\alpha(r)$ , we set the model function as

$$\alpha(r) = A_{\alpha,1} [\tanh \{(r - A_{\alpha,3})/A_{\alpha,2}\} - 1] , \quad (4.9)$$

where  $A_{\alpha,1}$ ,  $A_{\alpha,2}$ , and  $A_{\alpha,3}$  are free parameters. We choose this functional form just to describe  $\alpha(r)$  with a small number of free parameters. Fig. 4.11 shows the radial distribution of  $\alpha(r)$ . We can see that eq. (4.9) is in good agreement. We set the fitting range between vertical lines shown in Fig. 4.11, based on the reason that is given below.

We show the cluster mass dependence of  $\alpha(r)$  in Fig. 4.12. We can see that more massive clusters have larger fraction of the splashback component, and the larger splashback radius as shown in Mansfield et al. (2017).

For  $\delta(r)$  and  $\lambda(r)$ , we set the model function as

$$l(r) = A_{l,1} \exp(-rA_{l,2}) + A_{l,3} + A_{l,4}r. \quad (4.10)$$

where  $l$  runs over  $\delta$  and  $\lambda$ . Note that  $A_{l,1}$ ,  $A_{l,2}$ ,  $A_{l,3}$ , and  $A_{l,4}$  are free parameters. Fig. 4.13 shows  $\delta(r)$  and  $\lambda(r)$ . The lower limit of the fitting range is same as the lower limit

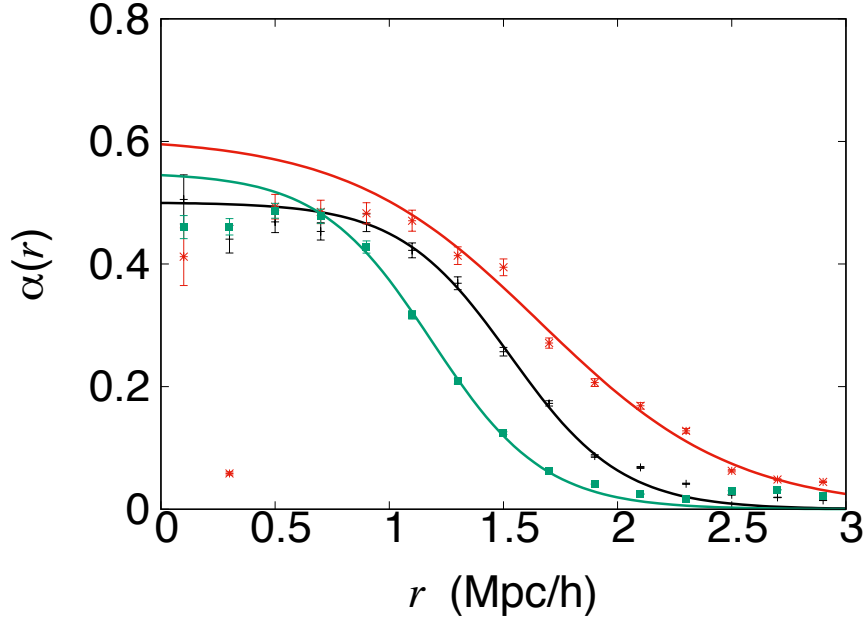


Figure 4.12: Radial distribution of  $\alpha(r)$  for each galaxy cluster mass bin. Black symbols and line correspond to the middle mass bin, red to the high mass bin, and green to the low mass bin. Points show  $\alpha(r)$  calculated by fitting eq. (4.6) to the radial velocity distribution, and lines are the best fit lines of eq. (4.9).

for  $\alpha$ . We can see that eq. (4.10) is in good agreement with  $\delta(r)$  and  $\lambda(r)$  within the fitting range.

We show the cluster mass dependence of  $\delta(r)$  and  $\lambda(r)$  in Fig. 4.14. We can see that even at  $r > 20$  Mpc/h,  $\delta(r)$  and  $\lambda(r)$  show the dependence on the cluster mass.

For  $\xi(r)$  and  $\gamma(r)$ , following Zu & Weinberg (2013), we set the model function as

$$l(r) = A_{l,1} - A_{l,2}r^{A_{l,3}} + A_{l,4}r, \quad (4.11)$$

where  $l$  runs over  $\xi$  and  $\gamma$ . Note that  $A_{l,1}$ ,  $A_{l,2}$ ,  $A_{l,3}$ , and  $A_{l,4}$  are free parameters. Fig. 4.15 shows  $\xi(r)$  and  $\gamma(r)$ . The lower limit of the fitting range is same as the lower limit set  $\alpha(r)$ . We can see that eq. (4.11) is in good agreement with  $\delta(r)$  and  $\lambda(r)$  within our fitting range.

We show the cluster mass dependence of  $\xi(r)$  and  $\gamma(r)$  in Fig. 4.16. We can see that even at  $r > 20$  Mpc/h,  $\xi(r)$  and  $\gamma(r)$  depend on the galaxy cluster mass.

For  $\mu_r$ , we set model function same as Zu & Weinberg (2013). The function form is

$$\mu_r(r) = A_{\mu_r,1} - A_{\mu_r,2}r^{A_{\mu_r,3}}. \quad (4.12)$$

Fig. 4.17 shows  $\mu_r(r)$ . The fitting range is same as  $\alpha(r)$ . We can see that eq. (4.12) is in good agreement with  $\mu_r(r)$ .

We show the cluster mass dependence of  $\mu_r(r)$  in Fig. 4.18. We can see that more massive clusters have larger  $\mu_r(r)$ . Moreover, the radius with  $\mu_r(r) \sim 0$  is very similar

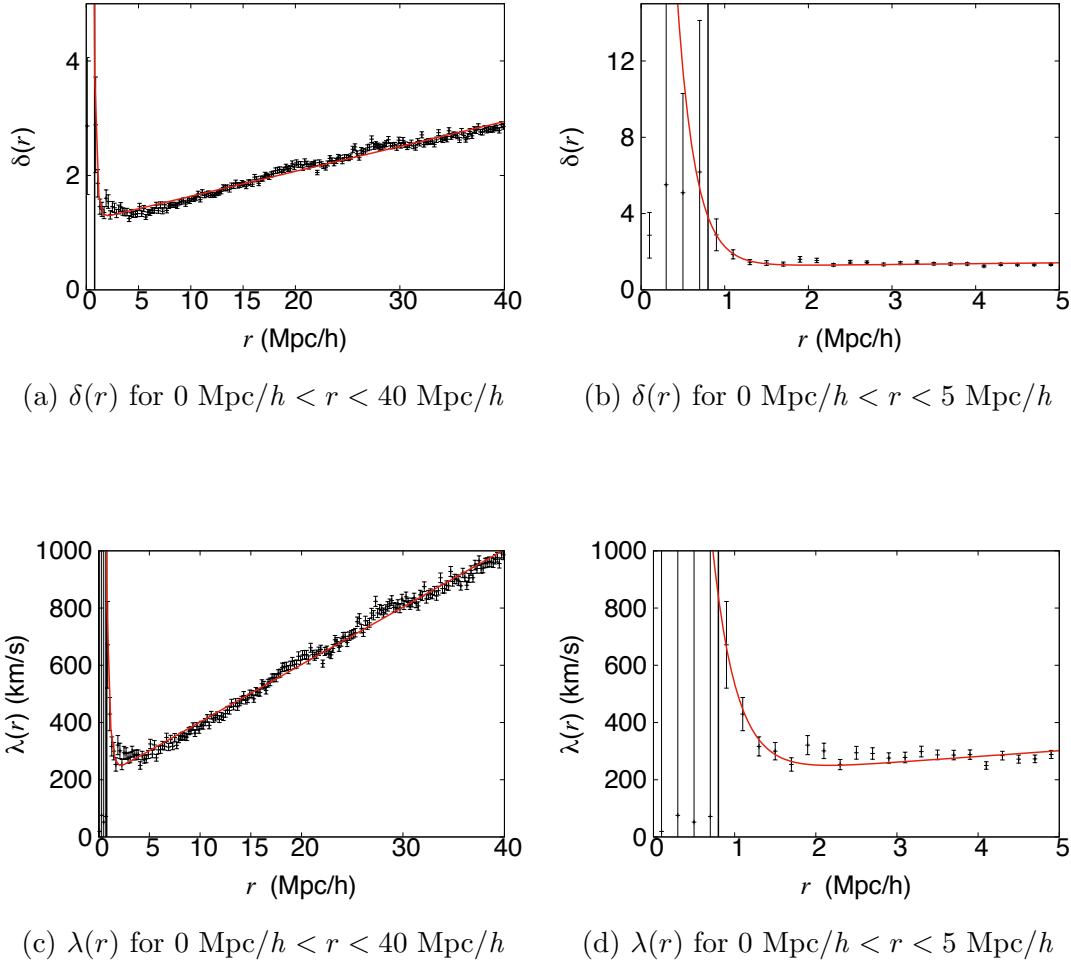


Figure 4.13: Same as Fig. 4.11, but for  $\delta(r)$  and  $\lambda(r)$ . We use eq. (4.10) instead of eq. (4.9). The lower limit of the fitting range, which is indicated by the vertical line, is same as the lower limit for  $\alpha(r)$ .

to the radius with  $\alpha(r) \sim 0$ . This indicates that the infall component may include dark matter halos which are on their second orbit to falling into galaxy clusters.

For  $\sigma_r$ ,  $\sigma_{t,\text{infall}}$  and  $\sigma_{t,\text{SB}}$ , we set model function same as  $\delta(r)$  and  $\lambda(r)$ . The function form is

$$l(r) = A_{l,1} \exp(-rA_{l,2}) + A_{l,3} + A_{l,4}r, \quad (4.13)$$

where  $l$  runs over  $\sigma_r$ ,  $\sigma_{t,\text{infall}}$ , and  $\sigma_{t,\text{SB}}$ . Fig. 4.19 shows  $\sigma_r(r)$  and  $\sigma_{t,\text{SB}}(r)$ . The fitting range is same as  $\alpha(r)$ . We can see that eq. (4.13) is in good agreement with  $\sigma_r(r)$  and  $\sigma_{t,\text{SB}}(r)$  within the fitting range.

We show the cluster mass dependence of  $\sigma_r(r)$  and  $\sigma_{t,\text{SB}}(r)$  in Fig. 4.20. We can see that eq. (4.13) is in good agreement with  $\sigma_r(r)$  and  $\sigma_{t,\text{SB}}(r)$  within fitting range for other cluster mass bins.

Fig. 4.22 shows  $\sigma_{t,\text{infall}}(r)$ . The lower limit of the fitting range is same as the lower limit set for  $\alpha(r)$ . We can see that eq. (4.13) is in good agreement with  $\sigma_{t,\text{infall}}(r)$  within fitting

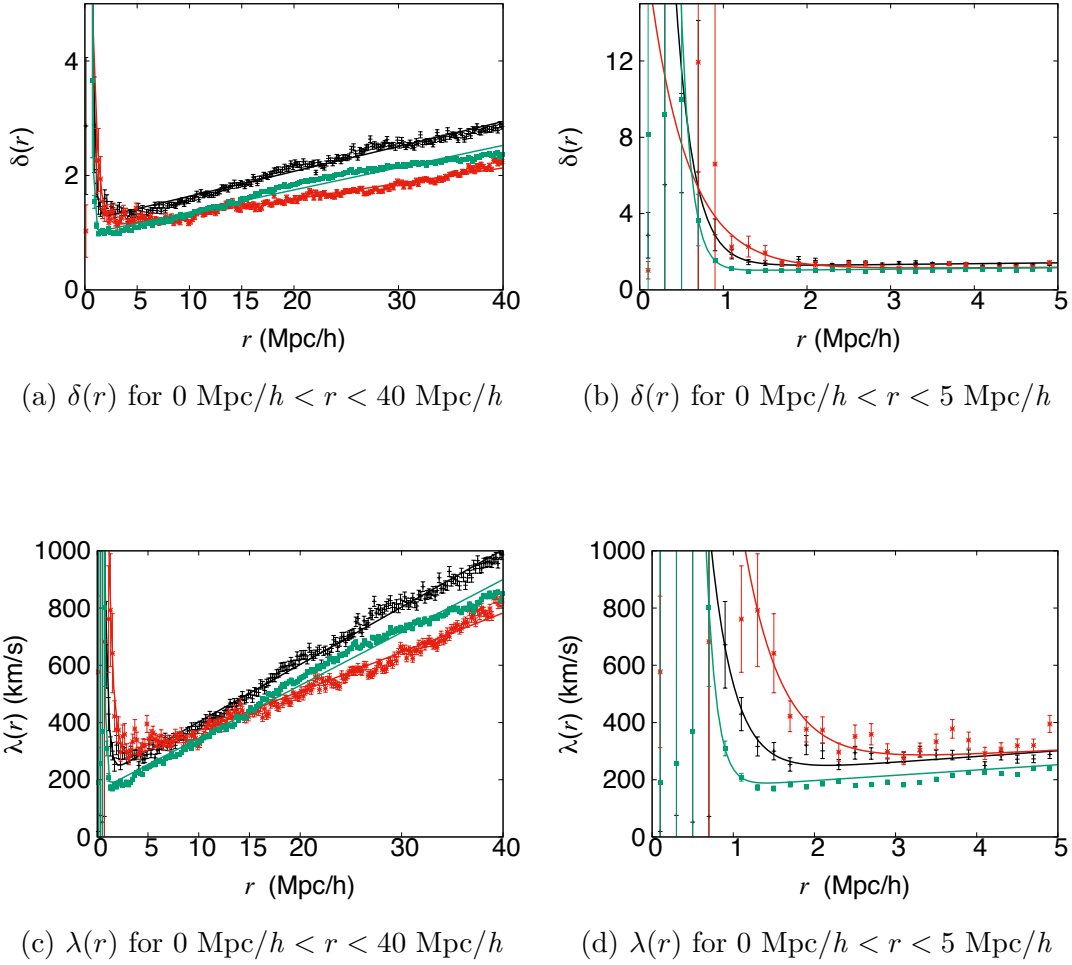


Figure 4.14: Same as Fig. 4.12, but for  $\delta(r)$  and  $\lambda(r)$ . We use eq. (4.10) instead of eq. (4.9).

range.

Then we show the galaxy cluster mass dependence of  $\sigma_{t,\text{infall}}(r)$  in Fig. 4.22. We can see that eq. (4.13) is in good agreement with  $\sigma_{t,\text{infall}}(r)$ . More massive clusters have larger  $\sigma_{t,\text{infall}}(r)$  even at  $r > 20 \text{ Mpc}/h$ .

We cannot determine parameters of the splashback component in the range that there is no splashback component, i.e.  $\alpha \ll 1$ . Hence, for  $\alpha(r)$ ,  $\mu_r(r)$ ,  $\sigma_r(r)$ , and  $\sigma_{t,\text{SB}}(r)$ , we need to set upper limit of the fitting range. We set the upper limit as the radius that  $\alpha(r)$  calculated by fitting eq. (4.6) to radial velocity distributions become smaller than 0.1. We also set the lower limit of the fitting range for computational reasons. Note that the fitting range is set independently for each cluster mass bin. We show the upper and lower limits of the fitting range for each cluster mass bin in Table 4.1.

We summarize all the fitting results in Table 4.2. We show residuals of fitting, e.g.,  $\Delta\alpha^2/\text{dof}$ , which are typical differences between fitting lines and parameter values. We can see that all the residuals are sufficiently small compared to typical absolute values of

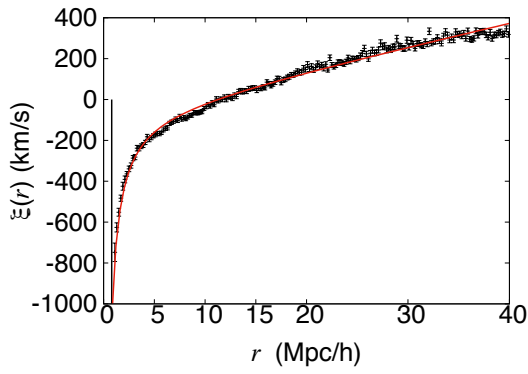
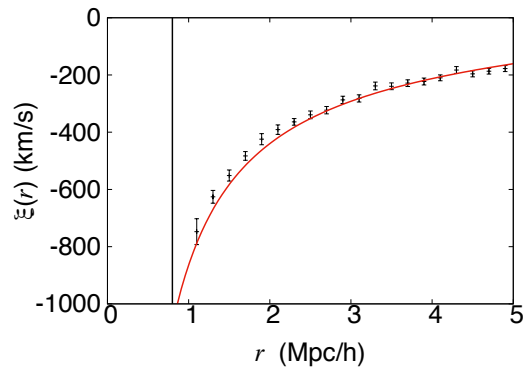
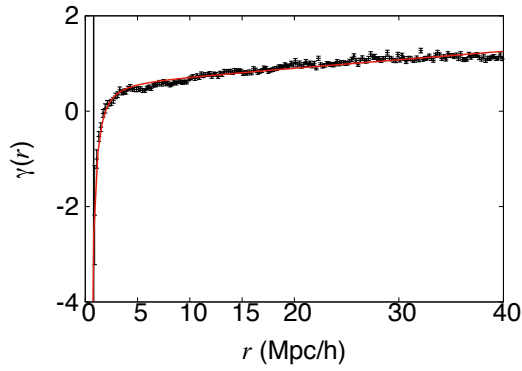
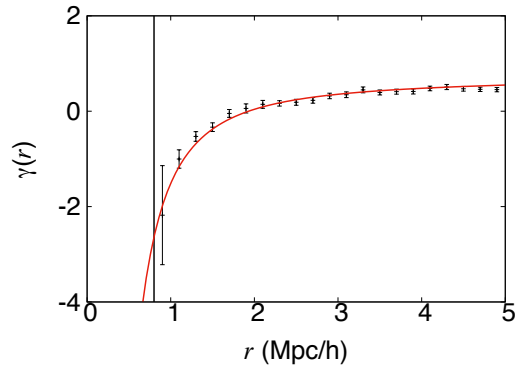
(a)  $\xi(r)$  for  $0 \text{ Mpc}/h < r < 40 \text{ Mpc}/h$ (b)  $\xi(r)$  for  $0 \text{ Mpc}/h < r < 5 \text{ Mpc}/h$ (c)  $\gamma(r)$  for  $0 \text{ Mpc}/h < r < 40 \text{ Mpc}/h$ (d)  $\gamma(r)$  for  $0 \text{ Mpc}/h < r < 5 \text{ Mpc}/h$ 

Figure 4.15: Same as Fig. 4.13, but for  $\xi(r)$  and  $\gamma(r)$ . We use eq. (4.11) instead of eq. (4.10).

parameters.

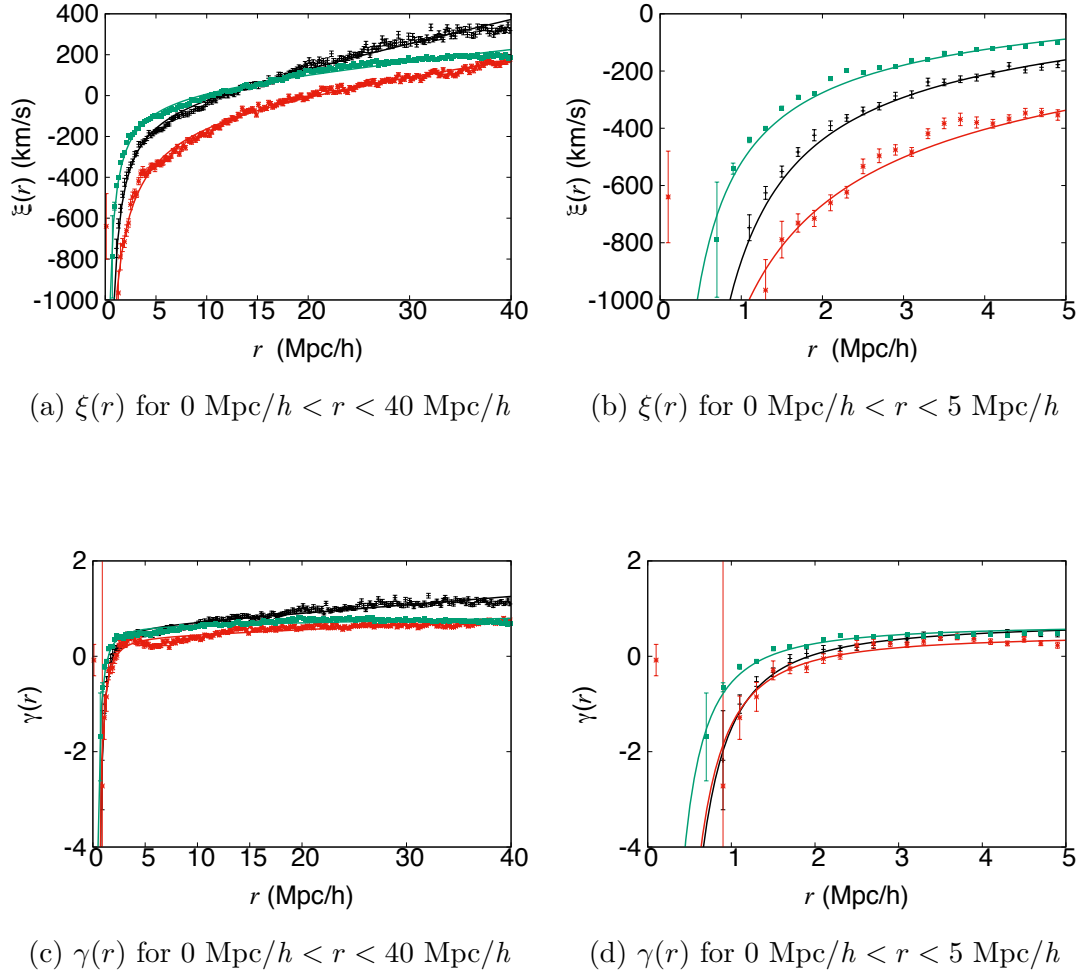


Figure 4.16: Same as Fig. 4.14, but for  $\xi(r)$  and  $\gamma(r)$ . We use eq. (4.11) instead of eq. (4.10).

Table 4.1: The upper and lower limits of the fitting range for each cluster mass bin.

cluster mass bin	lower limit of the fitting range	upper limit of the fitting range
low	0.6 $\text{Mpc}/h$	1.6 $\text{Mpc}/h$
middle	0.8 $\text{Mpc}/h$	2.0 $\text{Mpc}/h$
high	1.2 $\text{Mpc}/h$	2.6 $\text{Mpc}/h$

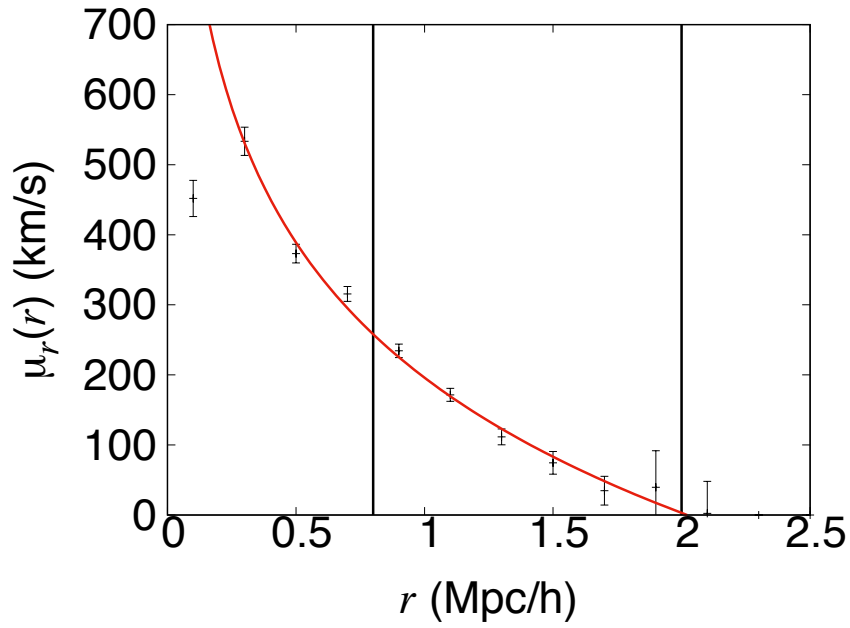


Figure 4.17: Same as Fig. 4.11, but for  $\mu_r(r)$ . We use eq. (4.12) instead of eq. (4.9).

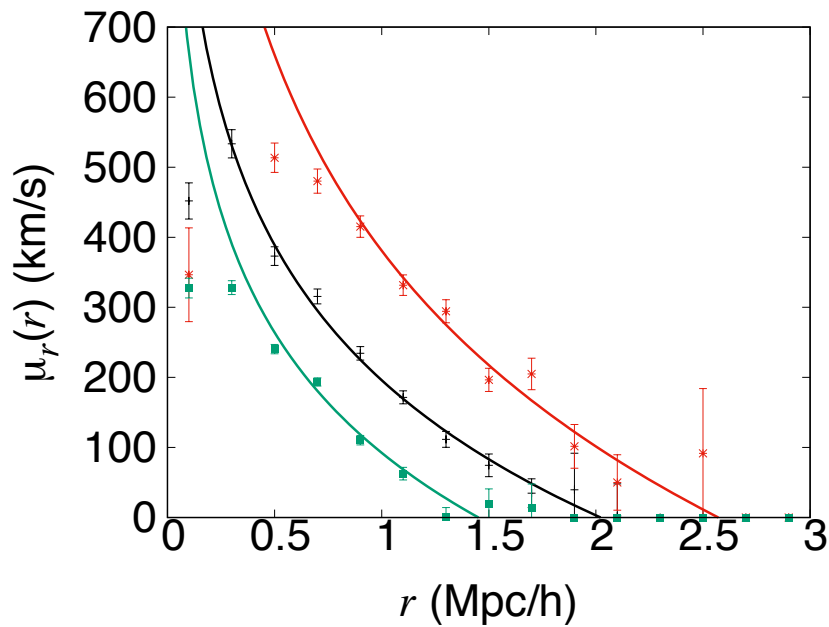


Figure 4.18: Same as Fig. 4.12, but for  $\mu_r(r)$ . We use eq. (4.12) instead of eq. (4.9).

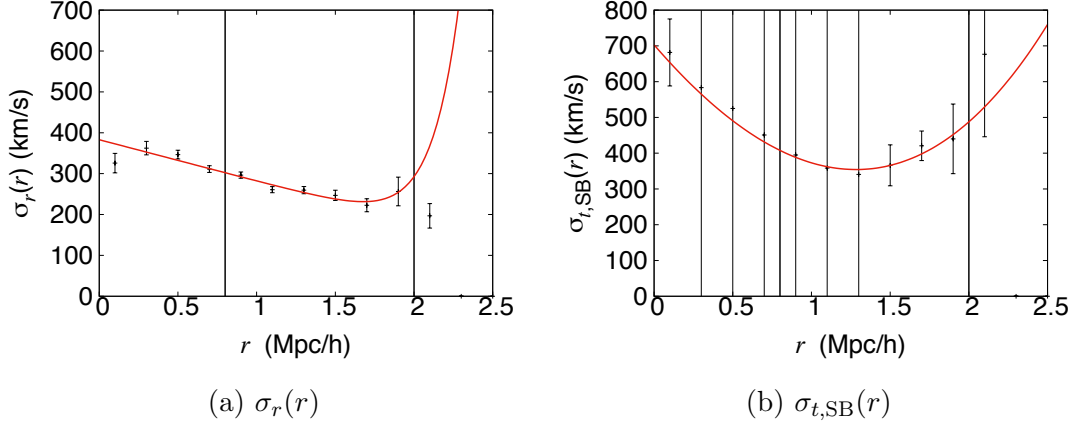


Figure 4.19: Same as Fig. 4.11, but for  $\sigma_r(r)$  and  $\sigma_{t,SB}(r)$ . We use eq. (4.13) instead of eq. (4.9).

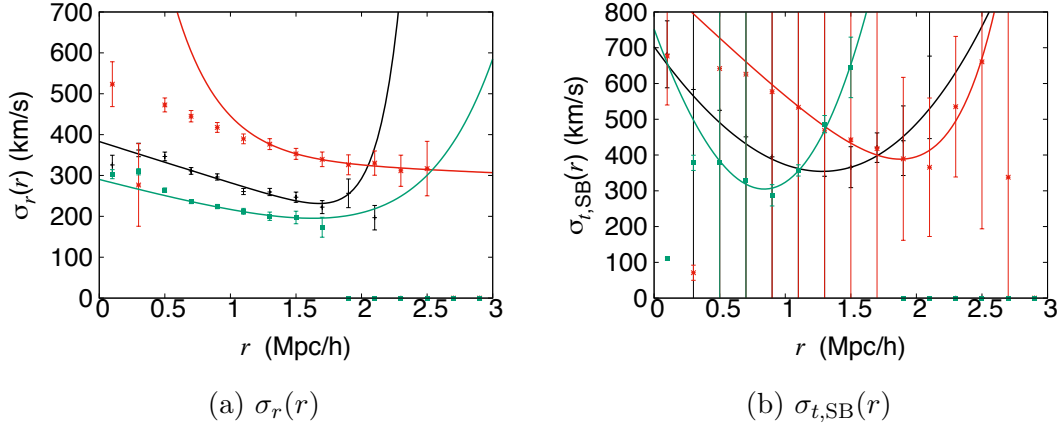


Figure 4.20: Same as Fig. 4.12, but for  $\sigma_r(r)$  and  $\sigma_{t,SB}(r)$ . We use eq. (4.13) instead of eq. (4.9).

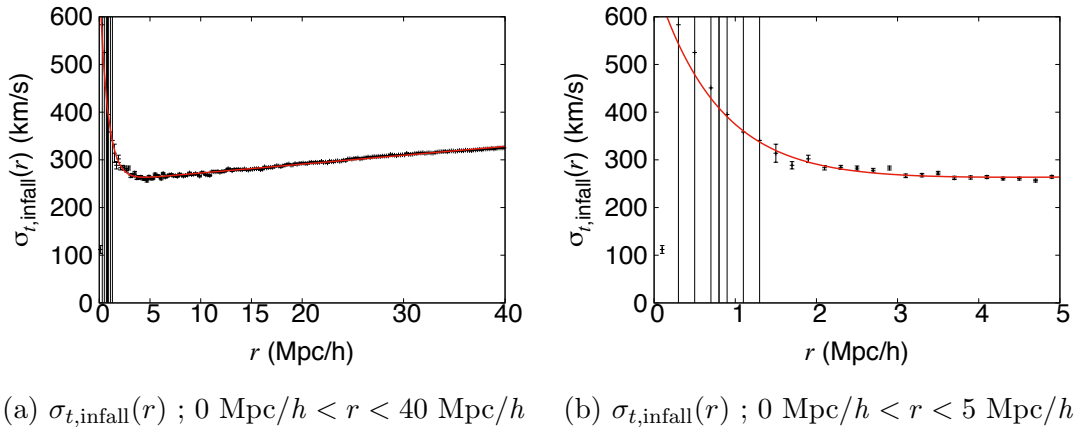
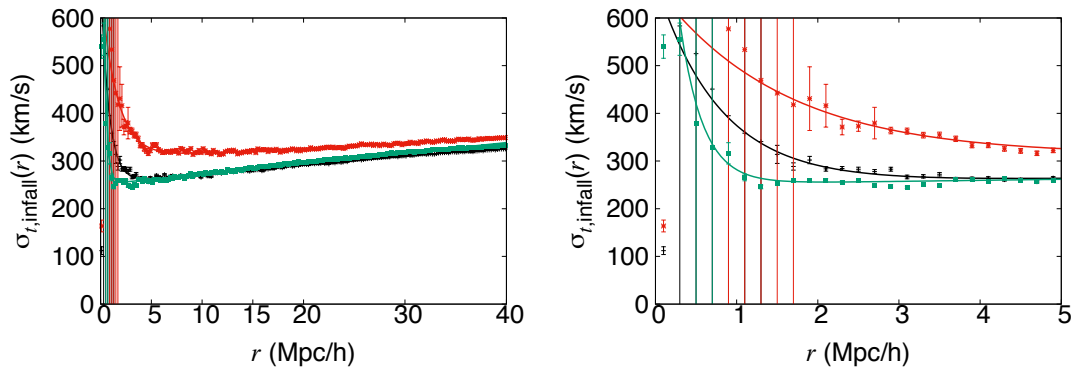


Figure 4.21: Same as Fig. 4.13, but for  $\sigma_{t,infall}(r)$ . We use eq. (4.13) instead of eq. (4.10).



(a)  $\sigma_{t,\text{infall}}(r)$  ;  $0 \text{ Mpc}/h < r < 40 \text{ Mpc}/h$     (b)  $\sigma_{t,\text{infall}}(r)$  ;  $0 \text{ Mpc}/h < r < 5 \text{ Mpc}/h$

Figure 4.22: Same as Fig. 4.12, but for  $\sigma_{t,\text{infall}}(r)$ . We use eq. (4.13) instead of eq. (4.9).

Table 4.2: Fitting results. See also eqs. (4.9), (4.10), (4.11), (4.12), and (4.13).

cluster mass bin	$A_{\alpha,1}$	$A_{\alpha,2}$	$A_{\alpha,3}$		$\Delta\alpha^2/dof$
low	-0.2747	0.4920	1.1856		$8.05 \times 10^{-4}$
middle	-0.2503	0.4863	1.5298		$7.37 \times 10^{-4}$
high	-0.3036	0.8484	1.6639		$58.95 \times 10^{-4}$
cluster mass bin	$A_{\delta,1}$	$A_{\delta,2}$	$A_{\delta,3}$	$A_{\delta,4}$	$\Delta\delta^2/dof$
low	757.5	8.072	0.9689	0.03891	$59.74 \times 10^{-4}$
middle	103.1	4.608	1.2004	0.04353	$64.82 \times 10^{-4}$
high	19.4	2.161	1.0473	0.02709	$44.05 \times 10^{-4}$
cluster mass bin	$A_{\lambda,1}$	$A_{\lambda,2}$	$A_{\lambda,3}$	$A_{\lambda,4}$	$\Delta\lambda^2/dof$
low	158008.0	7.891	160.0	18.49	523.3
middle	9565.6	3.416	201.0	20.08	464.6
high	9280.6	2.190	235.0	13.69	648.1
cluster mass bin	$A_{\xi,1}$	$A_{\xi,2}$	$A_{\xi,3}$	$A_{\xi,4}$	$\Delta\xi^2/dof$
low	55.67	581.4	-0.7666	5.097	288.3
middle	-55.79	819.8	-1.0118	11.192	506.7
high	43.85	1111.6	-0.6183	6.029	350.0
cluster mass bin	$A_{\gamma,1}$	$A_{\gamma,2}$	$A_{\gamma,3}$	$A_{\gamma,4}$	$\Delta\gamma^2/dof$
low	0.6200	1.1753	-1.6962	0.004419	$33.60^{-4}$
middle	0.5551	2.0867	-1.9243	0.017562	$51.34^{-4}$
high	0.3661	1.8175	-1.9456	0.009608	$48.71^{-4}$
cluster mass bin	$A_{\mu_r,1}$	$A_{\mu_r,2}$	$A_{\mu_r,3}$		$\Delta\mu_r^2/dof$
low	676808.0	676715.7	0.000366		866.1
middle	364923.6	364727.6	0.000763		322.3
high	245456.1	245075.1	0.001644		3557.7
cluster mass bin	$A_{\sigma_r,1}$	$A_{\sigma_r,2}$	$A_{\sigma_r,3}$	$A_{\sigma_r,4}$	$\Delta\sigma_r^2/dof$
low	2.7318	-1.7731	287.6	-86.799	6.551
middle	0.0013	-5.6642	382.9	-101.019	70.880
high	1980.8374	2.8624	345.7	-13.060	38.812
cluster mass bin	$A_{\sigma_{t,\text{infall},1}}$	$A_{\sigma_{t,\text{infall},2}}$	$A_{\sigma_{t,\text{infall},3}}$	$A_{\sigma_{t,\text{infall},4}}$	$\Delta\sigma_{t,\text{infall}}^2/dof$
low	981.2	3.521	250.7	2.201	13.59
middle	442.7	1.269	253.8	1.86	8.00
high	359.8	0.648	306.0	1.04	16.6
cluster mass bin	$A_{\sigma_{t,\text{SB},1}}$	$A_{\sigma_{t,\text{SB},2}}$	$A_{\sigma_{t,\text{SB},3}}$	$A_{\sigma_{t,\text{SB},4}}$	$\Delta\sigma_{t,\text{SB}}^2/dof$
low	4629.2	-0.4596	-3877.0	-3129.6	885.8
middle	3386.1	-0.3092	2683.1	-1556.9	453.4
high	1.6498	-2.3867	895.5	-347.7	1114.7

## 4.6 Reconstruct $v_{\text{los}}$ Histogram

By adopting best-fit parameters listed in Table 4.2 for eqs. (4.9), (4.10), (4.11), (4.12), and (4.13), we obtain smooth functions of eqs. (4.6) and (4.8), i.e., we have  $p_{v_r}(v_r, r)$  and  $p_{v_t}(v_t, r)$  for each cluster mass bin. The histogram of  $v_{\text{los}}$  can be derived by projecting the three-dimensional phase space distribution along the line-of-sight

$$p_{v_{\text{los}}}(v_{\text{los}}, r_{\text{proj}}) = \frac{1}{N(r_{\text{proj}})} \int_{-\infty}^{\infty} dv_r \int_{-\infty}^{\infty} dv_t \int_{-\infty}^{\infty} dd_{\text{los}} n(r) p_v(v_r, v_t, r) \delta_D(v_{\text{los}} - v'_{\text{los}}), \quad (4.14)$$

where,  $r_{\text{proj}}$  is the projected distance from the cluster center, and  $d_{\text{los}}$  is the line-of-sight distance from the cluster center,  $n(r)$  is the number density of satellite-halos and sub-halos,  $\delta_D(x)$  is the Dirac's delta distribution, and  $p_v(v_r, v_t, r)$  is phase space PDF (eq. 4.3). Note that  $r$  is defined as

$$r \equiv \sqrt{d_{\text{los}}^2 + r_{\text{proj}}^2}, \quad (4.15)$$

and  $N$  is a normalization factor defined as

$$N(r_{\text{proj}}) \equiv \int_{v_{\text{los,Lower}}}^{v_{\text{los,Upper}}} dv_{\text{los}} \int_{-\infty}^{\infty} dv_r \int_{-\infty}^{\infty} dv_t \int_{-\infty}^{\infty} dd_{\text{los}} \int_{-\infty}^{\infty} dv_{\text{los}} n(r) p_v(v_r, v_t, r) \delta_D(v_{\text{los}} - v'_{\text{los}}), \quad (4.16)$$

where  $v_{\text{los,Upper}}$  and  $v_{\text{los,Lower}}$  are upper and lower limits of  $v_{\text{los}}$  we calculate, respectively. Because of practical reasons, we set  $v_{\text{los,Upper}} = 2000$  km/s and  $v_{\text{los,Lower}} = -2000$  km/s in this thesis. Note that we can also apply this cut to observational data, because  $v_{\text{los}}$  is a direct observable. Hence, this cut does not affect comparisons of our model with observations. Also,  $v'_{\text{los}}$  is defined as

$$v'_{\text{los}} \equiv \cos \theta \cdot v_r + \sin \theta \cdot v_t + H \cdot d_{\text{los}}, \quad (4.17)$$

where  $H$  is the Hubble parameter, and  $\theta$  corresponds to the angle between the line from the cluster center and the line-of-sight (see also Fig. 4.23). At  $z = 0$ ,  $H \equiv H_0 = 100h$  km/s/Mpc.

In what follows, we set the integration range of  $v_r$  and  $v_t$  as  $-2000$  km/s  $< v_r, v_t < 2000$  km/s, because we find that there is almost no probability out of this range in the phase space distribution at any radii. We also set the integration range of  $d_{\text{los}}$  as  $-40$  Mpc/h  $< d_{\text{los}} < 40$  Mpc/h, because When we are interested in  $-2000$  km/s  $< v_{\text{los}} < 2000$  km/s, and we take the integration range of  $v_r$  and  $v_t$  and the Hubble flow at  $z = 0$  into account,  $-40$  Mpc/h  $< d_{\text{los}} < 40$  Mpc/h is sufficiently large.

In principle we can derive  $n(r)$  from observations, although in comparison with the  $N$ -body simulation results we use  $n(r)$  directly measured in the  $N$ -body simulation. Hence, all we have to determine is  $p_v(v_r, v_t, r)$ . Assuming that  $v_r$  and  $v_t$  are not correlated as we see in Section 4.2,  $p_v(v_r, v_t, r)$  is described as

$$p_v(v_r, v_t, r) = (1 - \alpha) SU(v_r; \delta, \lambda, \gamma, \xi) G(v_t; 0, \sigma_{t,\text{infall}}^2) + \alpha G(v_r; \mu_r, \sigma_r^2) G(v_t; 0, \sigma_{t,\text{SB}}^2). \quad (4.18)$$

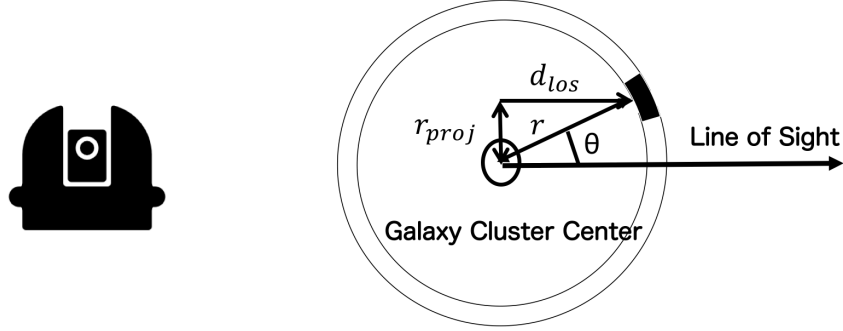


Figure 4.23: Schematic illustration of the integration parameters in eq. (4.17)

The first term of the right hand side of eq. (4.18) corresponds to the infall component, and the second term corresponds to the splashback component.

When we obtain phase space PDF,  $p_v(v_r, v_t, r)$ , we have assumed that  $v_r$  and  $v_t$  do not correlate and are independent with each other.

To explore the validity of this assumption, we check the correlation between  $v_r$  and  $v_t$  in  $p_v(v_r, v_t, r)$  by using  $\sqrt{v_r^2 + v_t^2}$ . We calculate  $\sqrt{v_r^2 + v_t^2}$  distribution from eq. (4.18) as

$$p\left(\sqrt{v_r^2 + v_t^2}, r\right) = \frac{1}{N(r)} \int_{-2000 \text{ km/s}}^{2000 \text{ km/s}} dv'_r \int_{-2000 \text{ km/s}}^{2000 \text{ km/s}} dv'_t n(r) p_v(v'_r, v'_t; r) \delta_D\left(\sqrt{v_r^2 + v_t^2} - \sqrt{v'^2_r + v'^2_t}\right), \quad (4.19)$$

where  $N(r)$  is a normalization factor. We call the PDF obtained in this way as "PDF from Theory" below. For comparison, we prepare the histogram obtained directly from the  $N$ -body simulation. We call the PDF obtained in this way as "PDF from Mock" below. If there is some correlation between  $v_r$  and  $v_t$ , these two PDFs do not match. In Figs. 4.24 and 4.25, we compare the PDF of  $(v_r^2 + v_t^2)^{1/2}$  from theory and PDF of  $(v_r^2 + v_t^2)^{1/2}$  from mock for the middle galaxy cluster mass bin for each radial bins. In Figs. 4.26 and 4.27, we also compare these two PDFs for other cluster mass bins. Although  $\chi^2/\text{dof}$  is not good for large radial bins,  $\Delta p^2_{(v_r^2+v_t^2)^{1/2}}/\text{dof}$  are still reasonably small.

We now check  $v_{\text{los}}$  PDFs. We can calculate the PDF of  $v_{\text{los}}$  from theory using eq. (4.14). We compare it with the PDF of  $v_{\text{los}}$  from mock for each cluster mass bins and  $r_{\text{proj}}$  bin in Figs. 4.28, 4.29, 4.30, and 4.31. We obtain relatively good  $\chi^2/\text{dof}$  and  $\Delta p^2_{v_{\text{los}}}/\text{dof}$ , despite the fact that there are relatively large deviations in  $p_{(v_r^2+v_t^2)^{1/2}}$ .

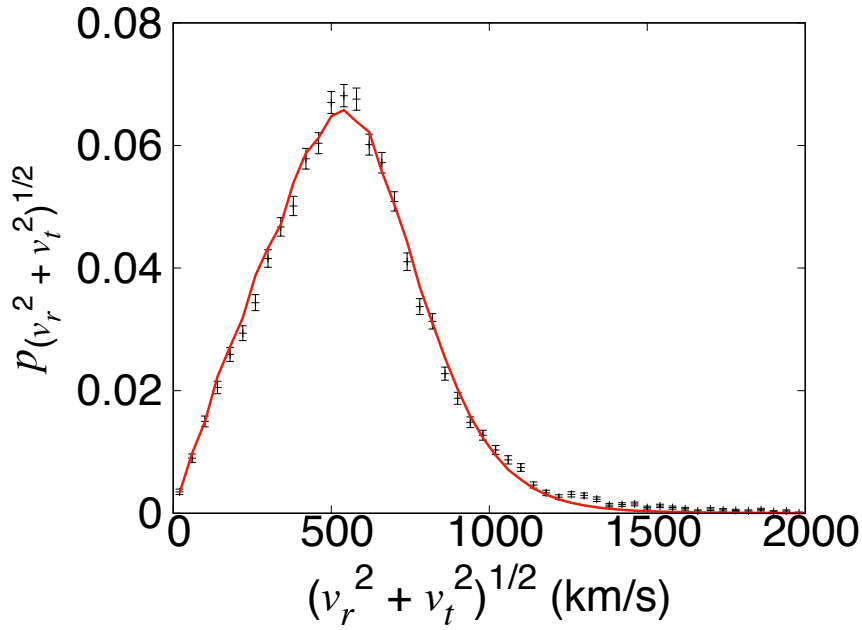
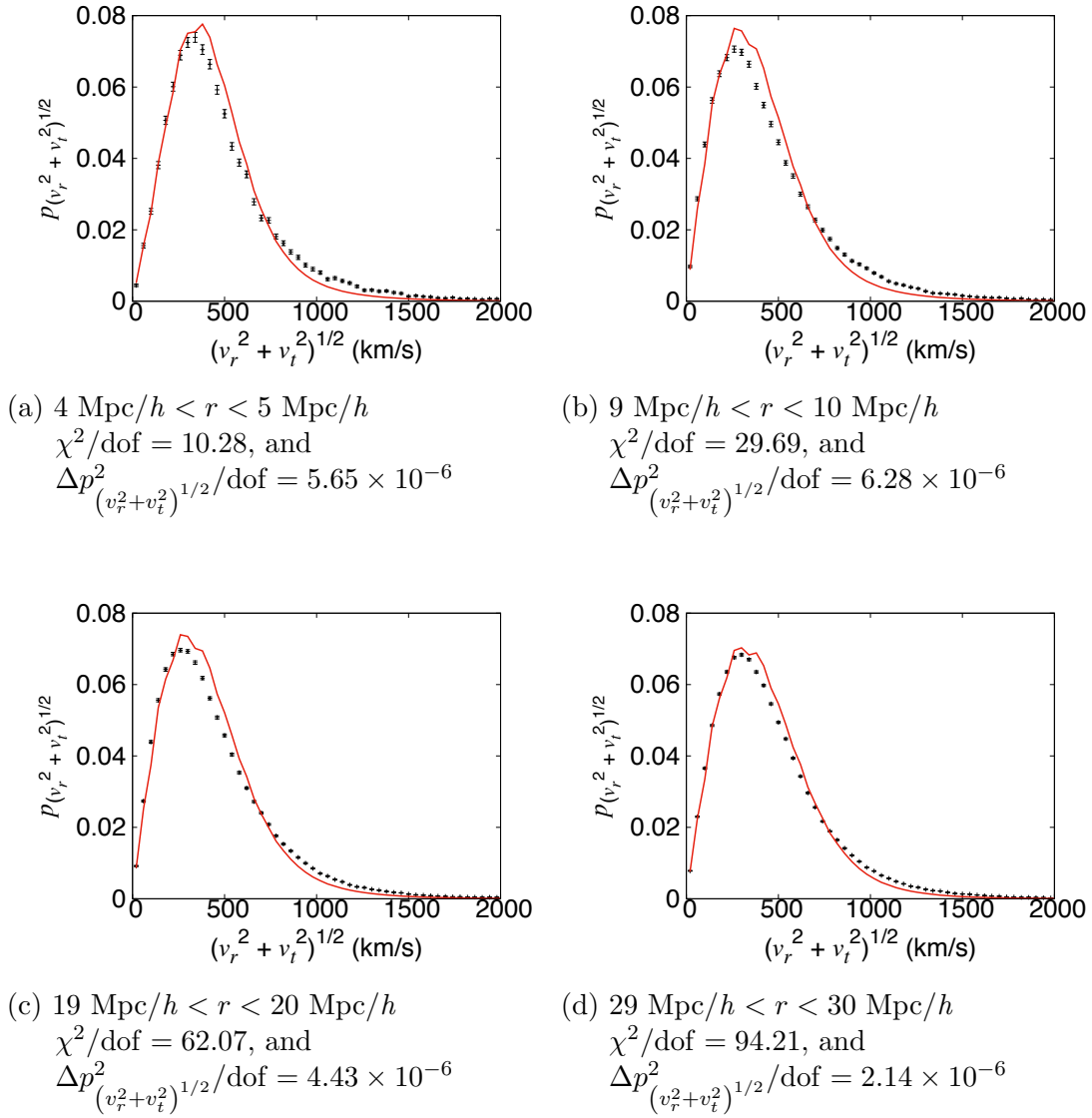


Figure 4.24: Comparison between the PDF of  $(v_r^2 + v_t^2)^{1/2}$  obtained from our theory and the PDF of  $(v_r^2 + v_t^2)^{1/2}$  from mock observation of our simulation for the middle galaxy cluster mass bin at  $1 \text{ Mpc}/h < r < 2 \text{ Mpc}/h$ . The solid line is the PDF of  $(v_r^2 + v_t^2)^{1/2}$  from theory, and points with error bars are the PDF of  $(v_r^2 + v_t^2)^{1/2}$  from Mock.  $\chi^2/\text{dof} = 2.20$ , and  $\Delta p^2_{(v_r^2 + v_t^2)^{1/2}}/\text{dof} = 1.31 \times 10^{-6}$ .

Figure 4.25: Same as Fig. 4.24, but for larger radii than  $2 \text{ Mpc}/h$ .

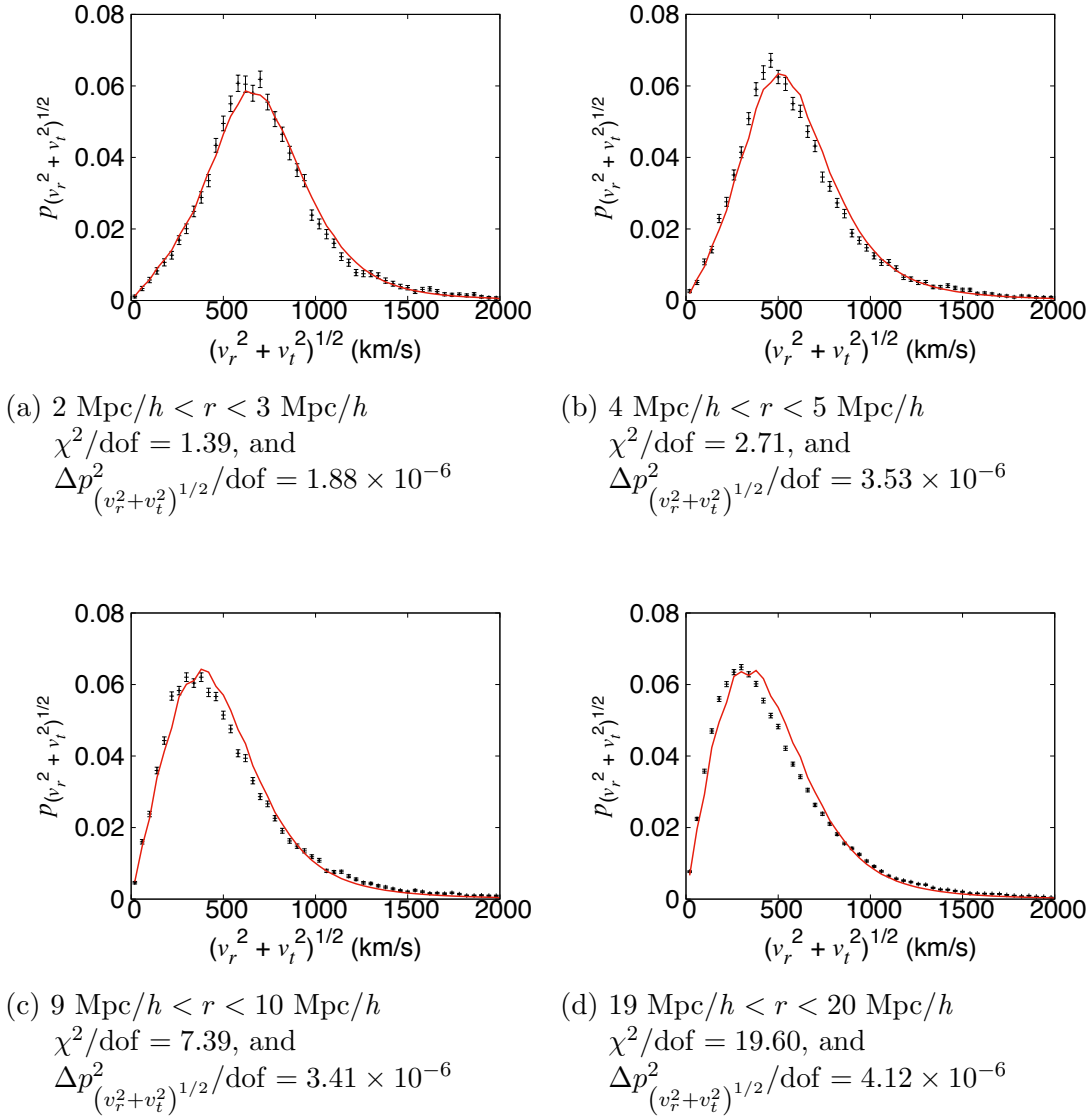


Figure 4.26: Same as Fig. 4.24, but for the high cluster mass bin and radii other than  $1 \text{ Mpc}/h < r < 2 \text{ Mpc}/h$ .

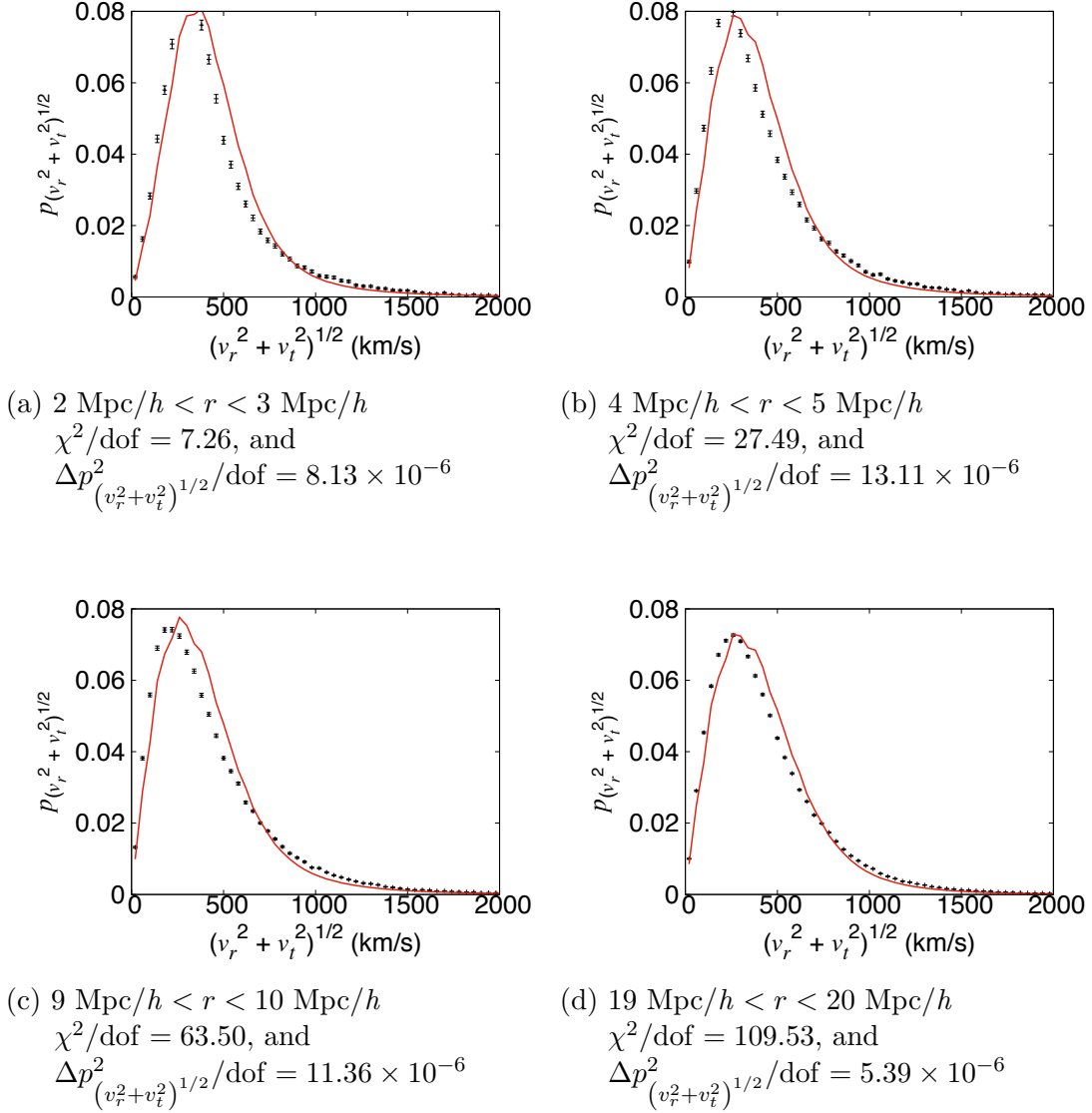


Figure 4.27: Same as Fig. 4.24, but for the low cluster mass bin and radii other than  $1 \text{ Mpc}/h < r < 2 \text{ Mpc}/h$ .

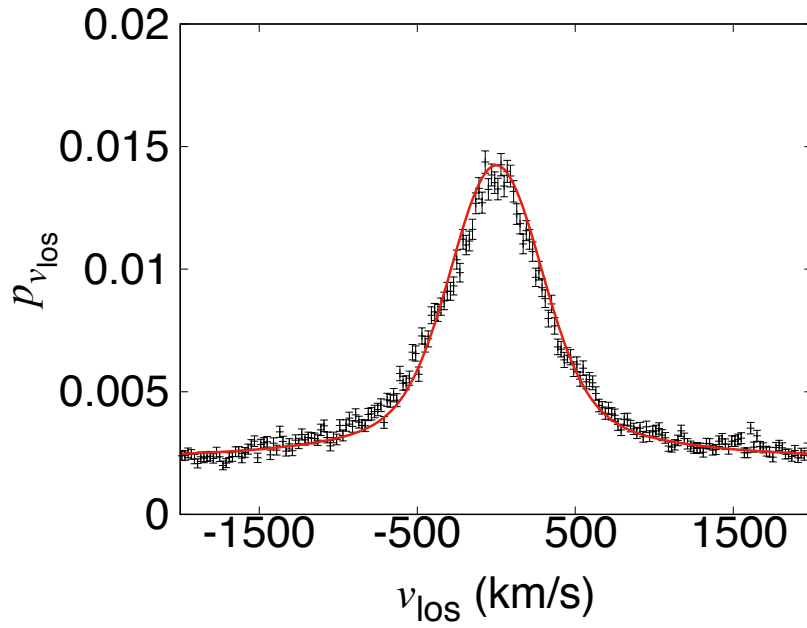
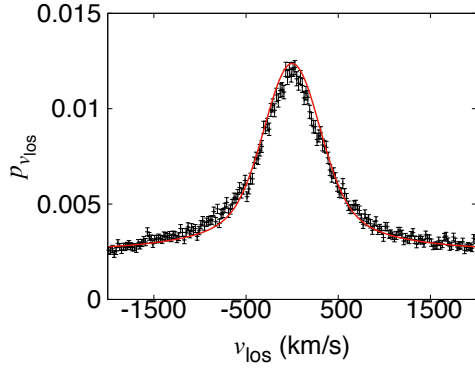
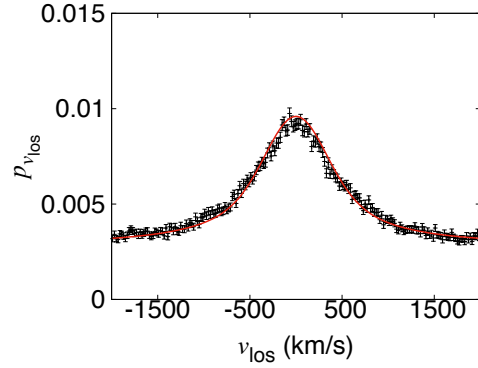


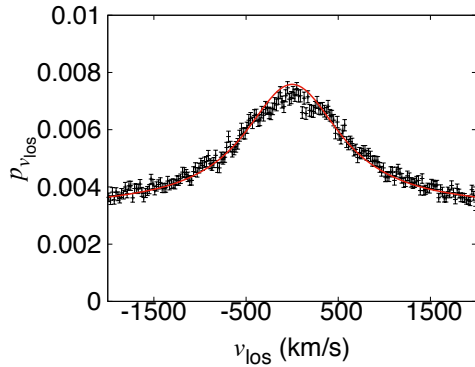
Figure 4.28: Comparison between PDF of  $v_{\text{los}}$  from our theory and PDF of  $v_{\text{los}}$  from mock observation of our simulation for the middle galaxy cluster mass bin at  $2 \text{ Mpc}/h < r_{\text{proj}} < 3 \text{ Mpc}/h$ . Red line is PDF of  $f_{v_{\text{los}}}$  from theory, and black points is PDF of  $v_{\text{los}}$  from Mock.  $\chi^2/\text{dof} = 2.36$ , and  $\Delta p_{v_{\text{los}}}^2/\text{dof} = 0.22 \times 10^{-6}$



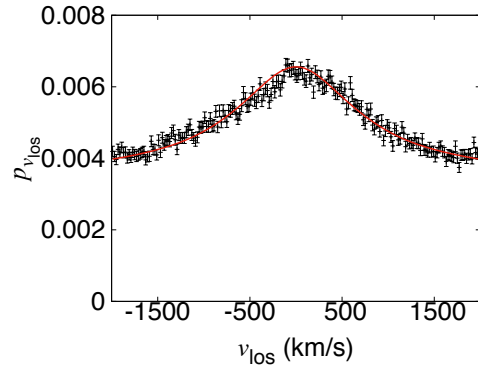
(a)  $3 \text{ Mpc}/h < r_{\text{proj}} < 4 \text{ Mpc}/h$   
 $\chi^2/\text{dof} = 2.12$ , and  
 $\Delta p_{v_{\text{los}}}^2/\text{dof} = 0.15 \times 10^{-6}$



(b)  $5 \text{ Mpc}/h < r_{\text{proj}} < 6 \text{ Mpc}/h$   
 $\chi^2/\text{dof} = 1.53$ , and  
 $\Delta p_{v_{\text{los}}}^2/\text{dof} = 7.67 \times 10^{-8}$

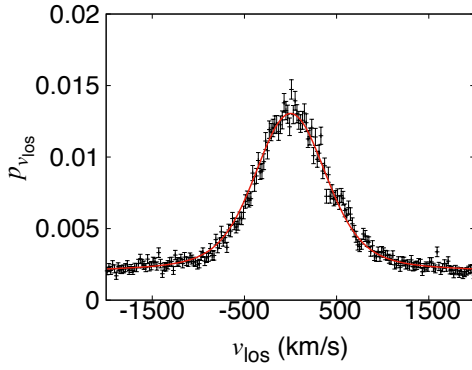


(c)  $8 \text{ Mpc}/h < r_{\text{proj}} < 9 \text{ Mpc}/h$   
 $\chi^2/\text{dof} = 1.57$ , and  
 $\Delta p_{v_{\text{los}}}^2/\text{dof} = 5.11 \times 10^{-8}$

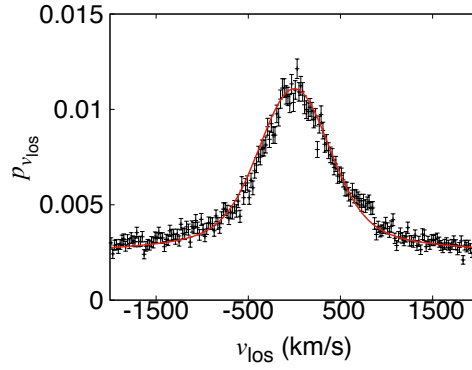


(d)  $11 \text{ Mpc}/h < r_{\text{proj}} < 12 \text{ Mpc}/h$   
 $\chi^2/\text{dof} = 1.43$ , and  
 $\Delta p_{v_{\text{los}}}^2/\text{dof} = 3.78 \times 10^{-8}$

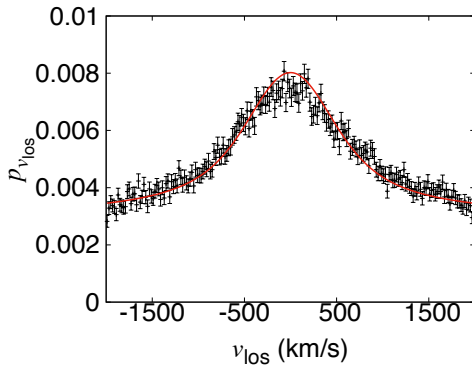
Figure 4.29: Same as Fig. 4.28, but for projection radii larger than  $2 \text{ Mpc}/h$ .



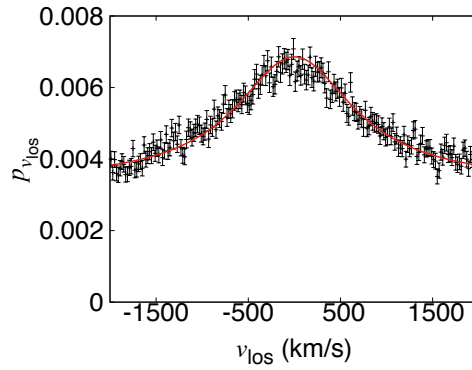
(a)  $2 \text{ Mpc}/h < r_{\text{proj}} < 3 \text{ Mpc}/h$   
 $\chi^2/\text{dof} = 1.19$ , and  
 $\Delta p_{v_{\text{los}}}^2/\text{dof} = 0.21 \times 10^{-6}$



(b)  $4 \text{ Mpc}/h < r_{\text{proj}} < 5 \text{ Mpc}/h$   
 $\chi^2/\text{dof} = 1.69$ , and  
 $\Delta p_{v_{\text{los}}}^2/\text{dof} = 0.20 \times 10^{-6}$



(c)  $8 \text{ Mpc}/h < r_{\text{proj}} < 9 \text{ Mpc}/h$   
 $\chi^2/\text{dof} = 1.48$ , and  
 $\Delta p_{v_{\text{los}}}^2/\text{dof} = 0.12 \times 10^{-6}$



(d)  $11 \text{ Mpc}/h < r_{\text{proj}} < 12 \text{ Mpc}/h$   
 $\chi^2/\text{dof} = 1.12$ , and  
 $\Delta p_{v_{\text{los}}}^2/\text{dof} = 6.80 \times 10^{-8}$

Figure 4.30: Same as Fig. 4.28, but for the high cluster mass bin. We also show for projection radii other than  $2 \text{ Mpc}/h < r_{\text{proj}} < 3 \text{ Mpc}/h$ .

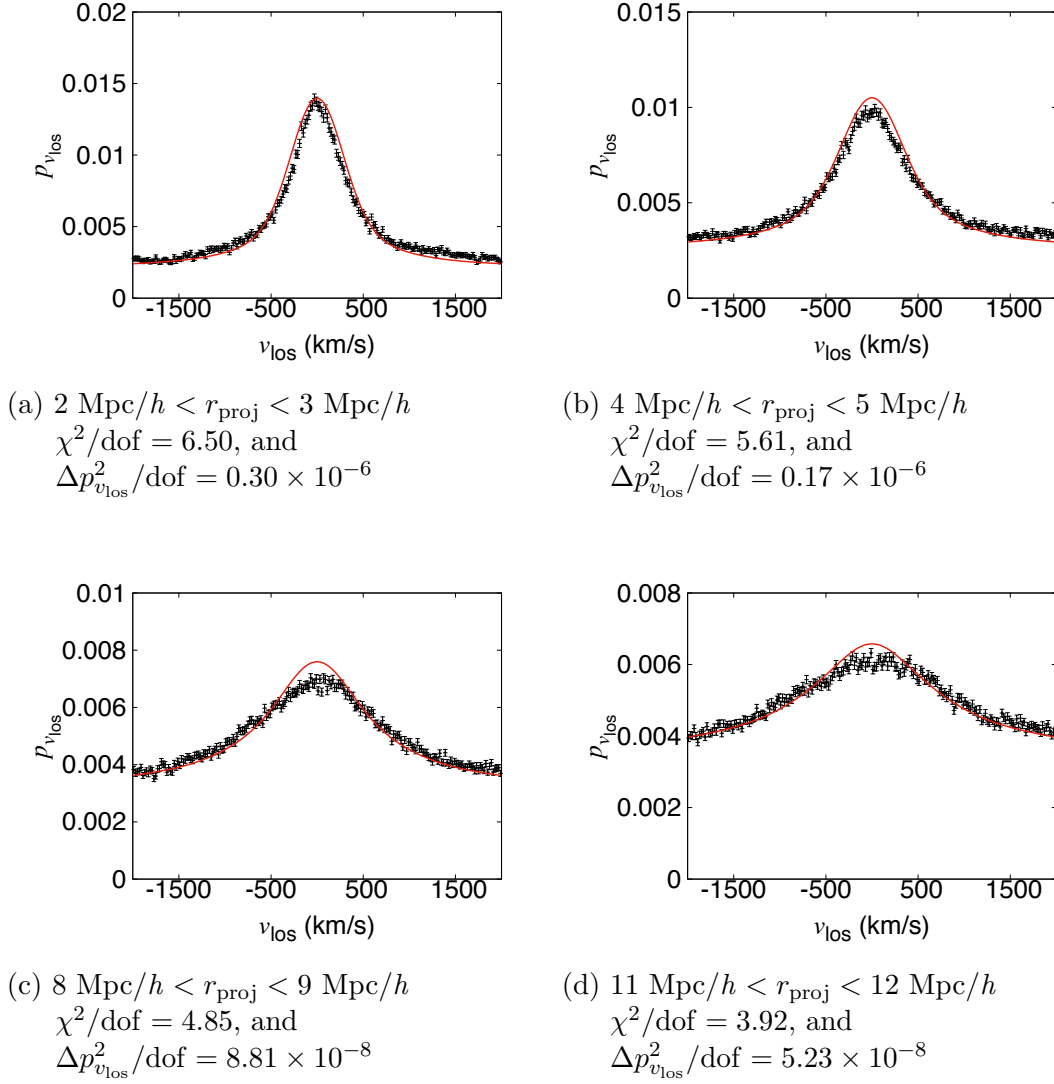


Figure 4.31: Same as Fig. 4.28, but for the low cluster mass bin. We also show for projection radii other than  $2 \text{ Mpc}/h < r_{\text{proj}} < 3 \text{ Mpc}/h$ .

Table 4.3: The upper and lower limits of the fitting range for each satellite-halo and sub-halo selection. See text.

data name	lower limit of the fitting range	upper limit of the fitting range
data-2	0.8 Mpc/h	2.0 Mpc/h
data-4	0.8 Mpc/h	1.8 Mpc/h
data-8	0.8 Mpc/h	1.8 Mpc/h
data-sat	0.8 Mpc/h	2.0 Mpc/h

## 4.7 Dependence of the Phase Space Distribution on Satellite-Halo Masses

In previous Sections, we fix the lower limit of satellite-halo and sub-halo masses as  $10^{11} M_{\odot}$ . However if this lower limit changes, the phase space distribution may also change. In this Section, we explore the satellite-halo and sub-halo mass dependence of the phase space distribution for the middle galaxy cluster mass bin.

To do so, we set three different lower limits of satellite-halo and sub-halo masses,  $2 \times 10^{11} M_{\odot}$  (called "data-2"),  $4 \times 10^{11} M_{\odot}$  ("data-4"), and  $8 \times 10^{11} M_{\odot}$  ("data-8"). We also consider the case that we only use satellite-halos with masses larger than  $10^{11} M_{\odot}$  ("data-sat"). We analyze these datasets in the same way as we did in previous Sections. In Tables 4.3 and 4.4, we show the results of our analysis of the phase space distributions from these datasets. In Table 4.4, we show residuals of fitting, e.g.,  $\Delta\alpha^2/dof$ . These are typical differences between fitting lines and parameter values. We can see that all the residuals are sufficiently small compared to typical absolute values of parameters.

In Figs. 4.32, 4.33, 4.34, 4.35, 4.36, and 4.37, we show the comparison of parameters of the phase space distribution for each satellite-halo and sub-halo selection for the middle galaxy cluster mass bin. We also plot parameters for the fiducial case that we set the lower limit of satellite-halo and sub-halo masses as  $1 \times 10^{11} M_{\odot}$  ("data-1") for comparison. We analyze the data in the same way as we did in previous sections. Note that data-sat have no satellite-halos within 1.0 Mpc/h, because all the halos within that radius are sub-halos rather than satellite-halos.

From Fig. 4.32, we can see that more massive satellite-halos and sub-halos have smaller fractions of the splashback component, and the smaller splashback radii.

From Figs. 4.33, 4.34, and 4.37, we can see that for  $\delta$ ,  $\lambda$ ,  $\xi$ ,  $\gamma$ , and  $\sigma_{t, \text{infall}}$ , parameters are very similar between data-1 and data-sat, and very similar between data2, data4, and data8.

We also check the correlation between  $v_r$  and  $v_t$  in these datasets. We check it in the same way as we did in Section 4.6. In Figs. 4.38, 4.39, 4.40, and 4.41, we compare the PDFs of  $(v_r^2 + v_t^2)^{1/2}$  from theory and the PDFs of  $(v_r^2 + v_t^2)^{1/2}$  from mock for each datasets at each radial bin. We can see similar trends with data-1 we saw in Section 4.6.

We show  $v_{\text{los}}$  PDFs for these datasets as in Section 4.6. In Figs. 4.42, 4.43, 4.44,

Table 4.4: Fitting results. See also eqs. (4.9), (4.10), (4.11), (4.12), and (4.13).

Data name	$A_{\alpha,1}$	$A_{\alpha,2}$	$A_{\alpha,3}$		$\Delta\alpha^2/\text{dof}$
data-2	-0.2347	0.4449	1.4983		$3.73 \times 10^{-4}$
data-4	-0.2565	0.5147	1.3944		$15.02 \times 10^{-4}$
data-8	-0.2698	0.4618	1.2869		$13.60 \times 10^{-4}$
data-sat	-0.2458	0.4769	1.5041		$4.56 \times 10^{-4}$
Data name	$A_{\delta,1}$	$A_{\delta,2}$	$A_{\delta,3}$	$A_{\delta,4}$	$\Delta\delta^2/\text{dof}$
data-2	106.0	5.195	1.0360	0.03793	$51.25 \times 10^{-4}$
data-4	181.0	5.870	1.0399	0.03743	$79.43 \times 10^{-4}$
data-8	88.9	5.932	1.0351	0.03713	$97.65 \times 10^{-4}$
data-sat	3.5	1.697	1.1836	0.04415	$60.31 \times 10^{-4}$
Data name	$A_{\lambda,1}$	$A_{\lambda,2}$	$A_{\lambda,3}$	$A_{\lambda,4}$	$\Delta\lambda^2/\text{dof}$
data-2	19691.2	4.545	196.5	17.82	431.3
data-4	22508.3	4.910	200.7	17.65	736.6
data-8	10064.2	4.801	204.0	17.45	937.1
data-sat	803.39	1.430	196.1	20.26	427.7
Data name	$A_{\xi,1}$	$A_{\xi,2}$	$A_{\xi,3}$	$A_{\xi,4}$	$\Delta\xi^2/\text{dof}$
data-2	-30.40	706.2	-0.7916	8.225	282.0
data-4	-44.33	683.0	-0.8088	8.373	461.8
data-8	-35.30	692.9	-0.7816	7.993	601.9
data-sat	56.41	805.8	-0.6619	9.439	355.3
Data name	$A_{\gamma,1}$	$A_{\gamma,2}$	$A_{\gamma,3}$	$A_{\gamma,4}$	$\Delta\gamma^2/\text{dof}$
data-2	0.4517	1.275	-1.817	0.011686	$28.06 \times 10^{-4}$
data-4	0.3998	1.182	-2.504	0.007569	$50.07 \times 10^{-4}$
data-8	0.4188	1.075	-1.931	0.011826	$63.64 \times 10^{-4}$
data-sat	0.6579	1, 726	-1.293	0.017562	$39.56 \times 10^{-4}$
Data name	$A_{\mu_r,1}$	$A_{\mu_r,2}$	$A_{\mu_r,3}$		$\Delta\mu_r^2/\text{dof}$
data-2	218047.0	217860.9	0.001661		257.0
data-4	408.8	242.4	0.060163		417.3
data-8	174310.2	174189.5	0.001430		975.1
data-sat	428.4	268.4	0.633703		205.8
Data name	$A_{\sigma_r,1}$	$A_{\sigma_r,2}$	$A_{\sigma_r,3}$	$A_{\sigma_r,4}$	$\Delta\sigma_r^2/\text{dof}$
data-2	0.0013	-5.6284	371.3	-84.689	110.045
data-4	545.8734	0.00000357	-184.0	-79.162	220.332
data-8	532.6487	0.0001584	-197.3	-39.8098	268.192
data-sat	5663.6579	0.1314	-5299.6	595.880	115.898
Data name	$A_{\sigma_{t,\text{infall},1}}$	$A_{\sigma_{t,\text{infall},2}}$	$A_{\sigma_{t,\text{infall},3}}$	$A_{\sigma_{t,\text{infall},4}}$	$\Delta\sigma_{t,\text{infall}}^2/\text{dof}$
data-2	252.5	0.767	269.8	1.71	9.67
data-4	184.3	0.853	268.8	1.78	19.84
data-8	108.3	0.708	265.0	1.92	34.62
data-sat	283.1	1.031	250.0	1.86	145.3
Data name	$A_{\sigma_{t,\text{SB},1}}$	$A_{\sigma_{t,\text{SB},2}}$	$A_{\sigma_{t,\text{SB},3}}$	$A_{\sigma_{t,\text{SB},4}}$	$\Delta\sigma_{t,\text{SB}}^2/\text{dof}$
data-2	0.0	-16.43	598.7	22.1	227.0
data-4	0.0	-14.59	329.1	8.56	12.5
data-8	$3 \times 10^{-6}$	444.4	1.6639	4.48	286.9
data-sat	9.9	-2.06	476.3	-20.53	54.8

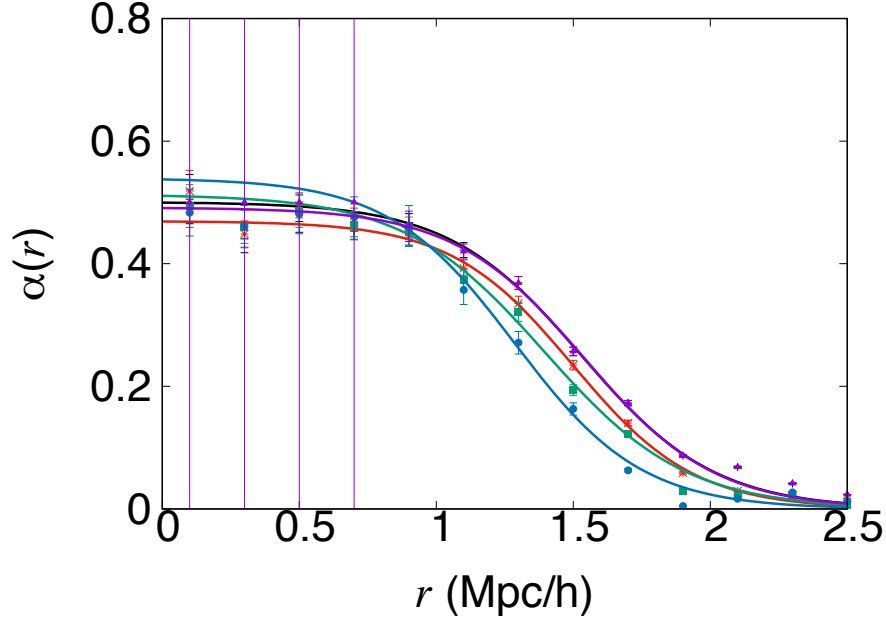
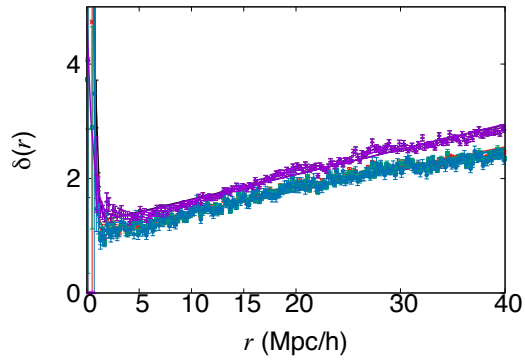
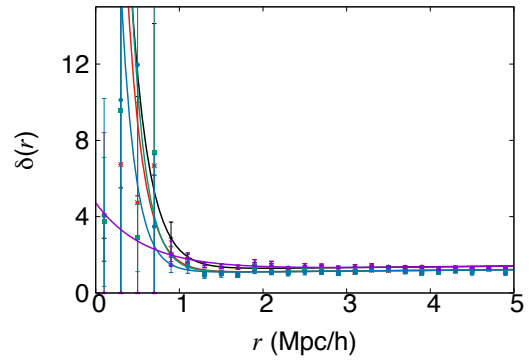


Figure 4.32: Radial distribution of  $\alpha(r)$  for each satellite-halos or sub-halos selection. Red corresponds to data-2, green to data-4, green to data-8, and magenta to data-sat. We also plot  $\alpha(r)$  for data-1 in black for comparison. Points are  $\alpha(r)$  calculated by fitting eq. (4.6) to radial velocity distribution, and lines are the best fit line eq. (4.9).

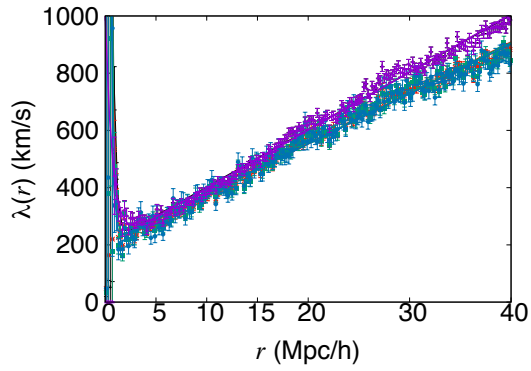
and 4.45, we show the comparison of the PDF of  $v_{\text{los}}$  from Mock and the PDF of  $v_{\text{los}}$  from Theory. We discuss the dependence of satellite-halo and sub-halo masses for the PDF of  $v_{\text{los}}$  in Section 5.1.



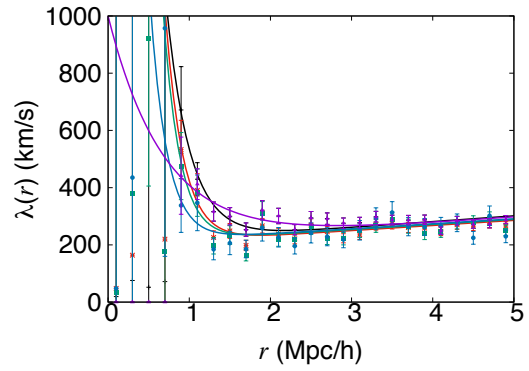
(a)  $\delta(r)$  for  $0 \text{ Mpc}/h < r < 40 \text{ Mpc}/h$



(b)  $\delta(r)$  for  $0 \text{ Mpc}/h < r < 5 \text{ Mpc}/h$



(c)  $\lambda(r)$  for  $0 \text{ Mpc}/h < r < 40 \text{ Mpc}/h$



(d)  $\lambda(r)$  for  $0 \text{ Mpc}/h < r < 5 \text{ Mpc}/h$

Figure 4.33: Same as Fig. 4.32, but for  $\delta(r)$  and  $\lambda(r)$ . We use eq. (4.10) instead of eq. (4.9).

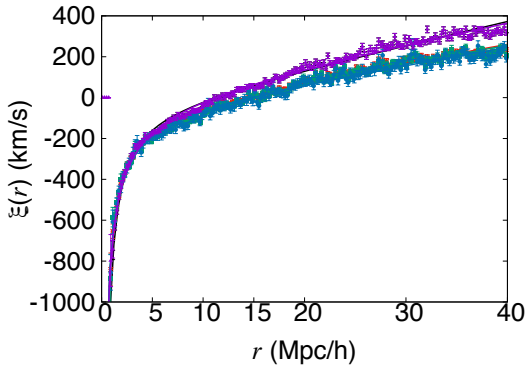
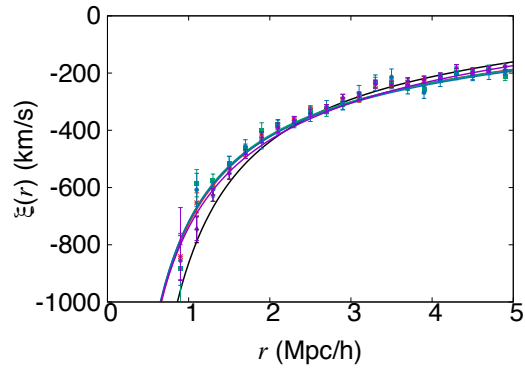
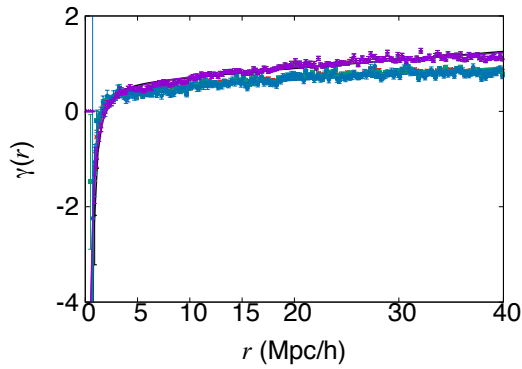
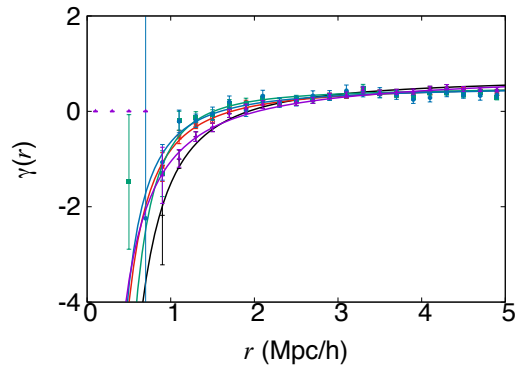
(a)  $\xi(r)$  for  $0 \text{ Mpc}/h < r < 40 \text{ Mpc}/h$ (b)  $\xi(r)$  for  $0 \text{ Mpc}/h < r < 5 \text{ Mpc}/h$ (c)  $\gamma(r)$  for  $0 \text{ Mpc}/h < r < 40 \text{ Mpc}/h$ (d)  $\gamma(r)$  for  $0 \text{ Mpc}/h < r < 5 \text{ Mpc}/h$ 

Figure 4.34: Same as Fig. 4.32, but for  $\xi(r)$  and  $\gamma(r)$ . We use eq. (4.11) instead of eq. (4.9).

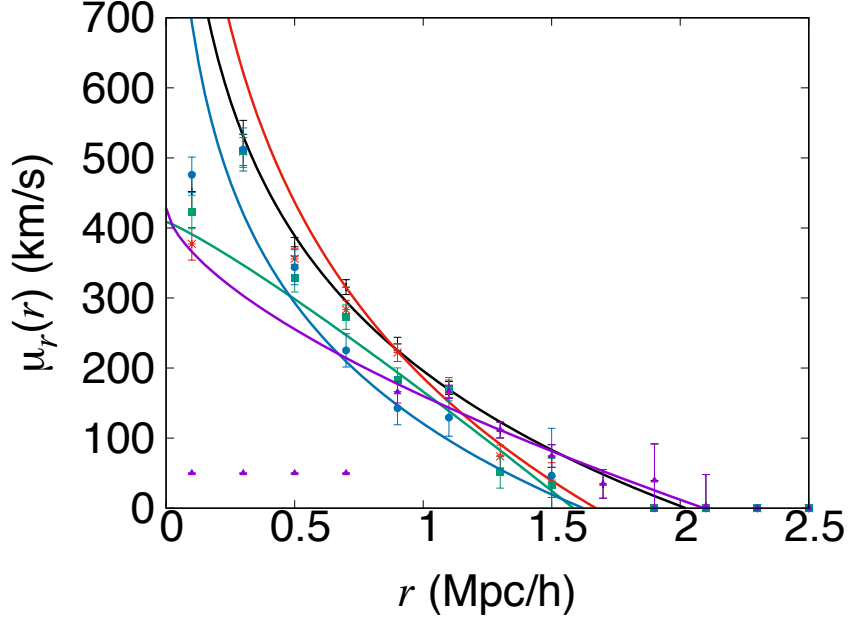
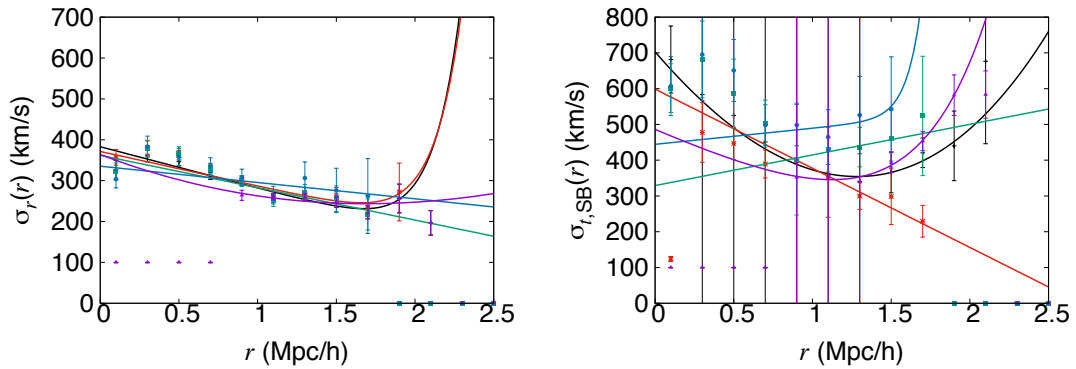


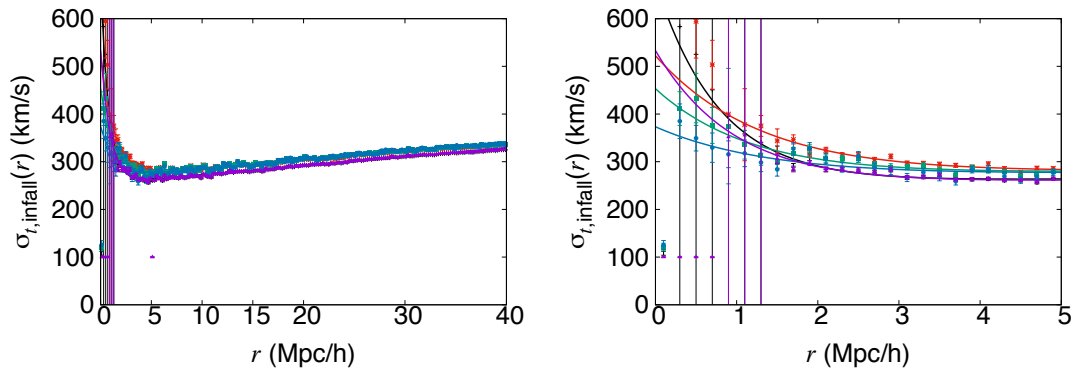
Figure 4.35: Same as Fig. 4.32, but for  $\mu_r(r)$ . We use eq. (4.12) instead of eq. (4.9).



(a)  $\sigma_r$  for  $0 \text{ Mpc}/h < r < 5 \text{ Mpc}/h$

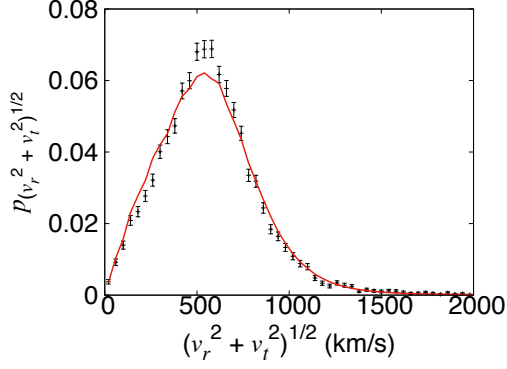
(b)  $\sigma_{t,SB}$  for  $0 \text{ Mpc}/h < r < 5 \text{ Mpc}/h$

Figure 4.36: Same as Fig. 4.32, but for  $\sigma_r(r)$  and  $\sigma_{t,SB}(r)$ . We use eq. (4.13) instead of eq. (4.9).

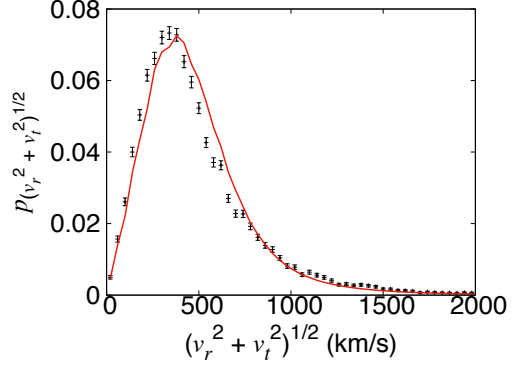


(a)  $\sigma_{t,\text{infall}}(r)$  for  $0 \text{ Mpc}/h < r < 40 \text{ Mpc}/h$     (b)  $\sigma_{t,\text{infall}}$  for  $0 \text{ Mpc}/h < r < 5 \text{ Mpc}/h$

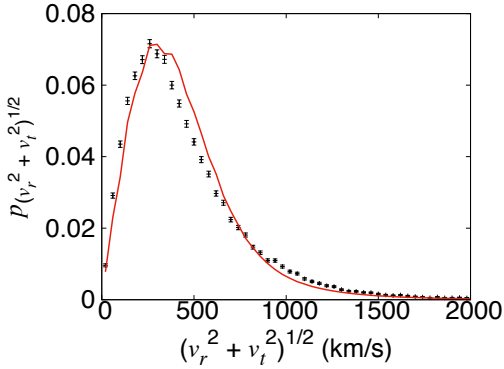
Figure 4.37: Same as Fig. 4.32, but for  $\sigma_{t,\text{infall}}(r)$ . We use eq. (4.13) instead of eq. (4.9).



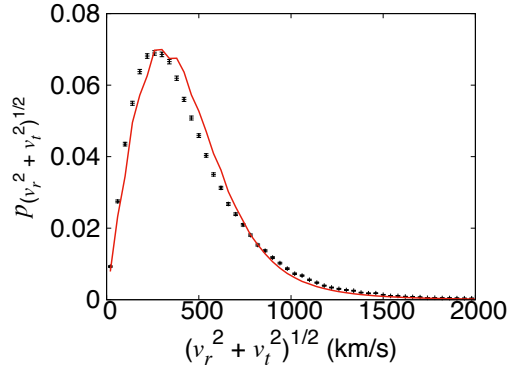
(a)  $1 \text{ Mpc}/h < r < 2 \text{ Mpc}/h$   
 $\chi^2/\text{dof} = 1.28$ , and  
 $\Delta p^2_{(v_r^2+v_t^2)^{1/2}}/\text{dof} = 3.53 \times 10^{-6}$



(b)  $4 \text{ Mpc}/h < r < 5 \text{ Mpc}/h$   
 $\chi^2/\text{dof} = 5.50$ , and  
 $\Delta p^2_{(v_r^2+v_t^2)^{1/2}}/\text{dof} = 7.22 \times 10^{-6}$

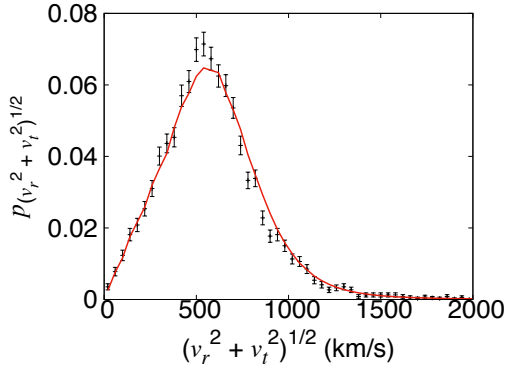


(c)  $9 \text{ Mpc}/h < r < 10 \text{ Mpc}/h$   
 $\chi^2/\text{dof} = 12.46$ , and  
 $\Delta p^2_{(v_r^2+v_t^2)^{1/2}}/\text{dof} = 6.65 \times 10^{-6}$

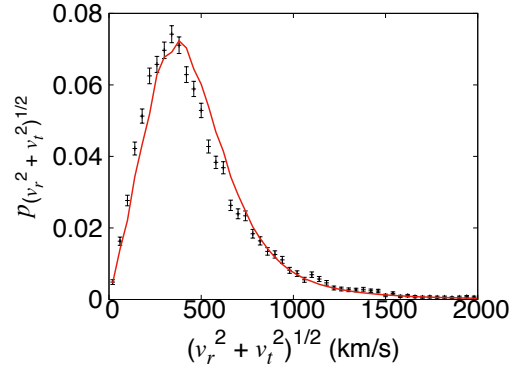


(d)  $19 \text{ Mpc}/h < r < 20 \text{ Mpc}/h$   
 $\chi^2/\text{dof} = 28.94$ , and  
 $\Delta p^2_{(v_r^2+v_t^2)^{1/2}}/\text{dof} = 5.24 \times 10^{-6}$

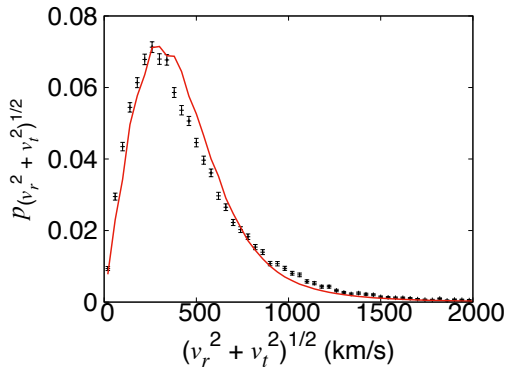
Figure 4.38: Comparison between PDF of  $(v_r^2 + v_t^2)^{1/2}$  from theory and PDF of  $(v_r^2 + v_t^2)^{1/2}$  from mock for data-2. Red line is PDF of  $(v_r^2 + v_t^2)^{1/2}$  from theory, and black points is PDF of  $(v_r^2 + v_t^2)^{1/2}$  from Mock.



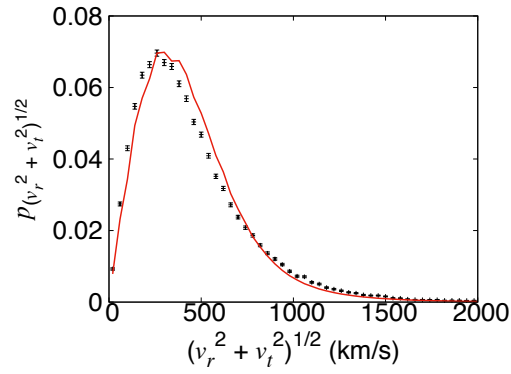
(a)  $1 \text{ Mpc}/h < r < 2 \text{ Mpc}/h$   
 $\chi^2/\text{dof} = 0.78$ , and  
 $\Delta p^2_{(v_r^2+v_t^2)^{1/2}}/\text{dof} = 3.33 \times 10^{-6}$



(b)  $4 \text{ Mpc}/h < r < 5 \text{ Mpc}/h$   
 $\chi^2/\text{dof} = 3.14$ , and  
 $\Delta p^2_{(v_r^2+v_t^2)^{1/2}}/\text{dof} = 7.88 \times 10^{-6}$



(c)  $9 \text{ Mpc}/h < r < 10 \text{ Mpc}/h$   
 $\chi^2/\text{dof} = 7.12$ , and  
 $\Delta p^2_{(v_r^2+v_t^2)^{1/2}}/\text{dof} = 6.78 \times 10^{-6}$



(d)  $19 \text{ Mpc}/h < r < 20 \text{ Mpc}/h$   
 $\chi^2/\text{dof} = 15.85$ , and  
 $\Delta p^2_{(v_r^2+v_t^2)^{1/2}}/\text{dof} = 4.96 \times 10^{-6}$

Figure 4.39: Same as Fig. 4.38, but for data-4.

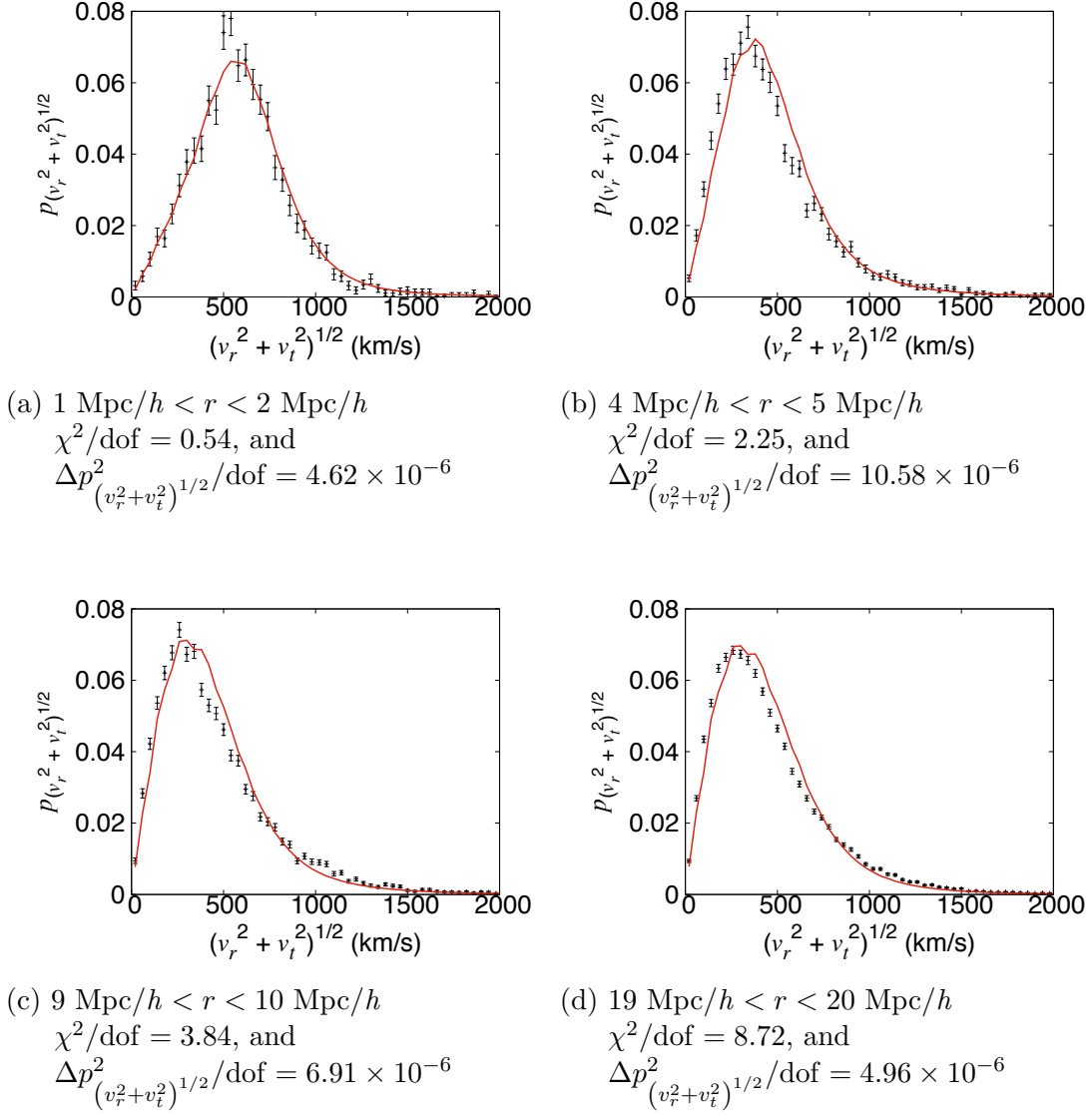
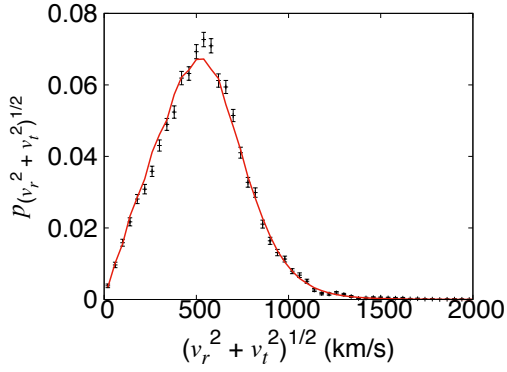
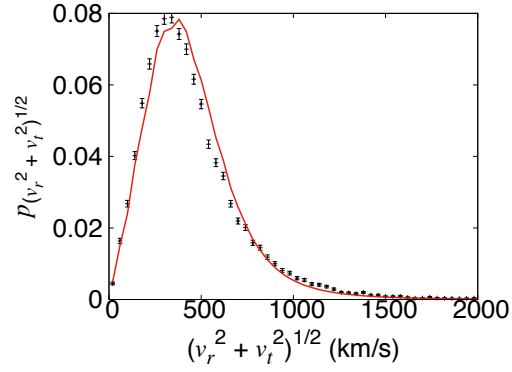


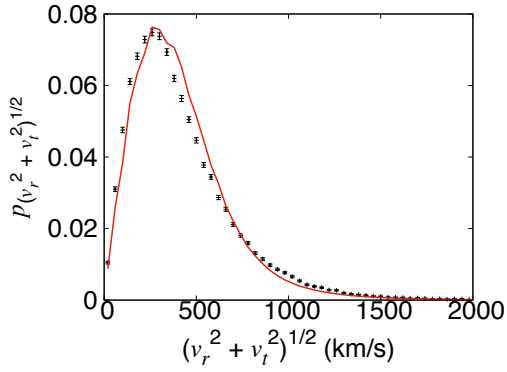
Figure 4.40: Same as Fig. 4.38, but for data-8.



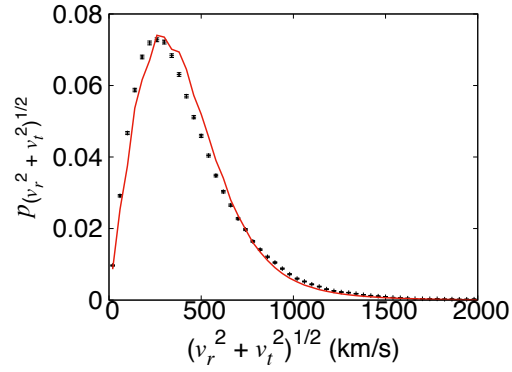
(a)  $1 \text{ Mpc}/h < r < 2 \text{ Mpc}/h$   
 $\chi^2/\text{dof} = 0.98$ , and  
 $\Delta p^2_{(v_r^2+v_t^2)^{1/2}}/\text{dof} = 2.00 \times 10^{-6}$



(b)  $4 \text{ Mpc}/h < r < 5 \text{ Mpc}/h$   
 $\chi^2/\text{dof} = 5.04$ , and  
 $\Delta p^2_{(v_r^2+v_t^2)^{1/2}}/\text{dof} = 5.25 \times 10^{-6}$



(c)  $9 \text{ Mpc}/h < r < 10 \text{ Mpc}/h$   
 $\chi^2/\text{dof} = 13.14$ , and  
 $\Delta p^2_{(v_r^2+v_t^2)^{1/2}}/\text{dof} = 5.43 \times 10^{-6}$



(d)  $19 \text{ Mpc}/h < r < 20 \text{ Mpc}/h$   
 $\chi^2/\text{dof} = 30.74$ , and  
 $\Delta p^2_{(v_r^2+v_t^2)^{1/2}}/\text{dof} = 4.41 \times 10^{-6}$

Figure 4.41: Same as Fig. 4.38, but for data-sat.

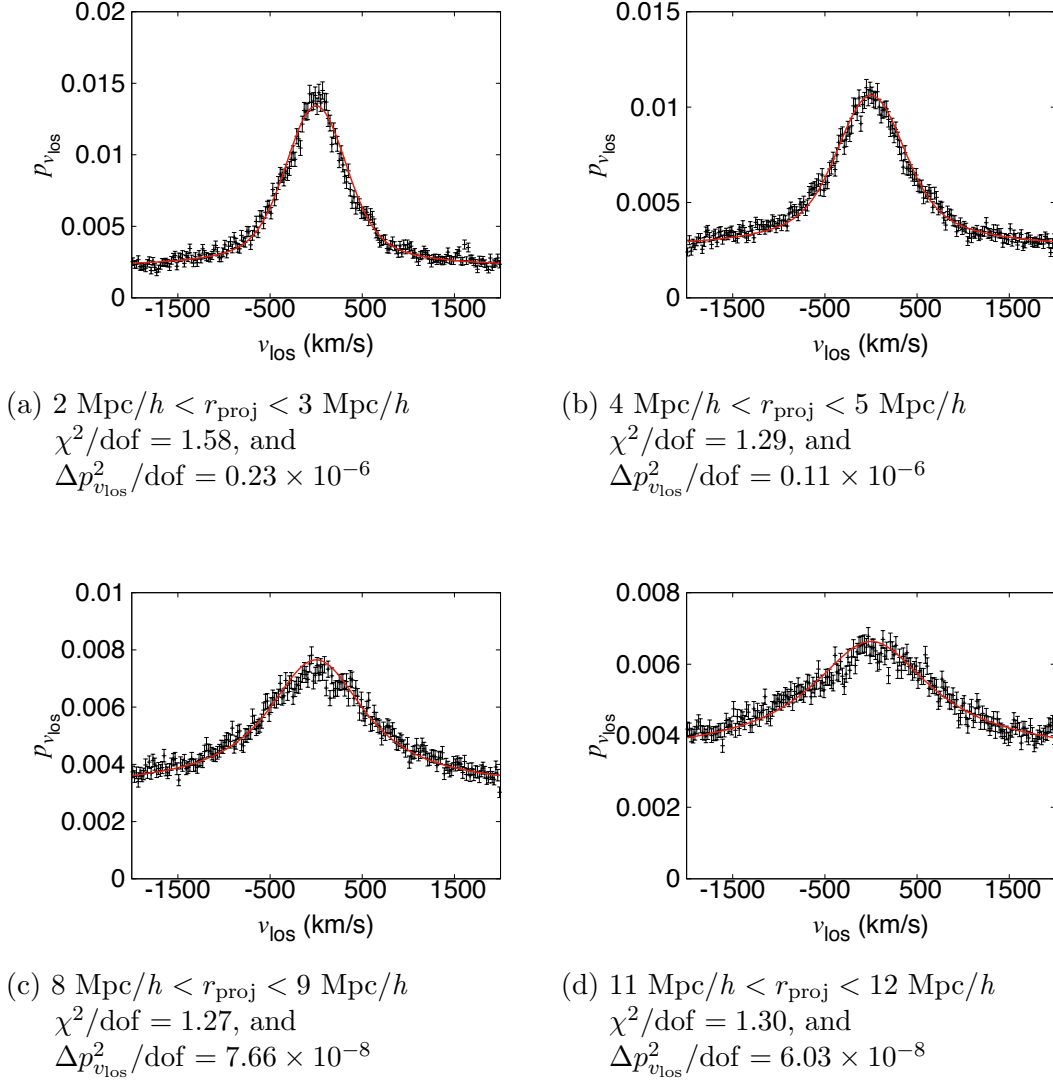
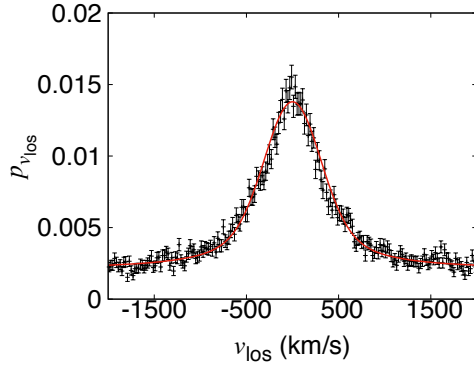
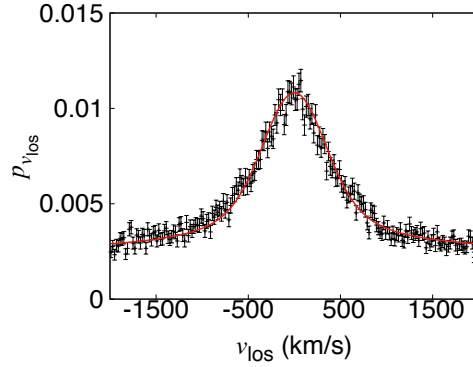


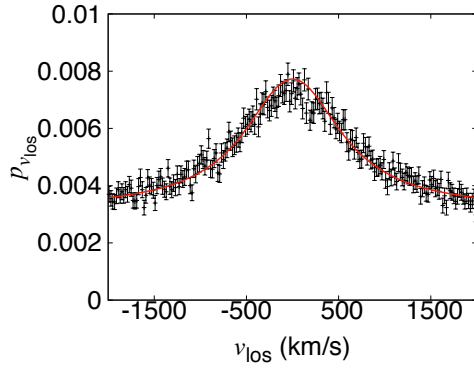
Figure 4.42: Comparison between PDF of  $v_{\text{los}}$  from theory and PDF of  $v_{\text{los}}$  from mock for data-2. Red line is PDF of  $v_{\text{los}}$  from theory, and black points is PDF of  $v_{\text{los}}$  from Mock.



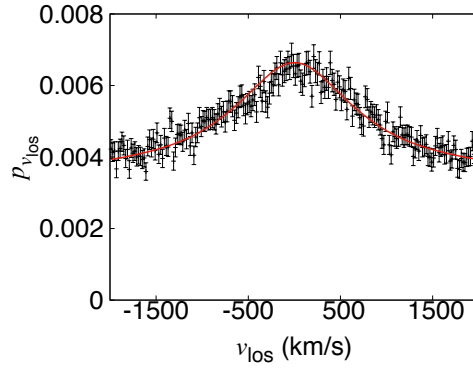
(a)  $2 \text{ Mpc}/h < r_{\text{proj}} < 3 \text{ Mpc}/h$   
 $\chi^2/\text{dof} = 1.24$ , and  
 $\Delta p_{v_{\text{los}}}^2/\text{dof} = 0.31 \times 10^{-6}$



(b)  $4 \text{ Mpc}/h < r_{\text{proj}} < 5 \text{ Mpc}/h$   
 $\chi^2/\text{dof} = 1.10$ , and  
 $\Delta p_{v_{\text{los}}}^2/\text{dof} = 0.18 \times 10^{-6}$

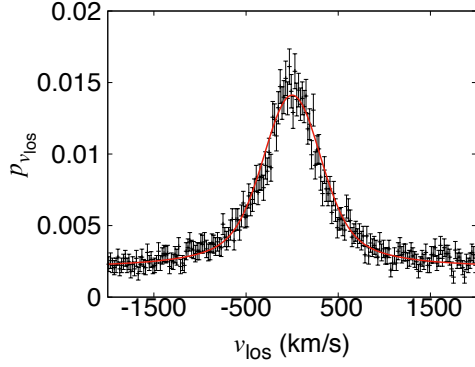


(c)  $8 \text{ Mpc}/h < r_{\text{proj}} < 9 \text{ Mpc}/h$   
 $\chi^2/\text{dof} = 1.03$ , and  
 $\Delta p_{v_{\text{los}}}^2/\text{dof} = 0.11 \times 10^{-6}$

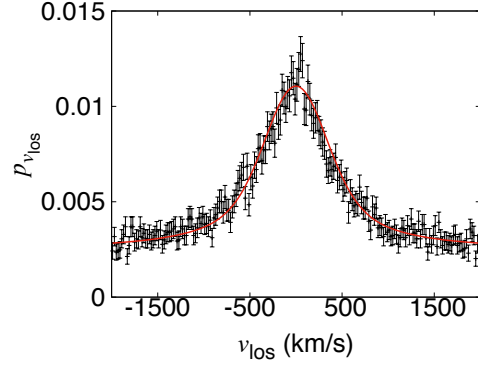


(d)  $11 \text{ Mpc}/h < r_{\text{proj}} < 12 \text{ Mpc}/h$   
 $\chi^2/\text{dof} = 1.00$ , and  
 $\Delta p_{v_{\text{los}}}^2/\text{dof} = 8.15 \times 10^{-8}$

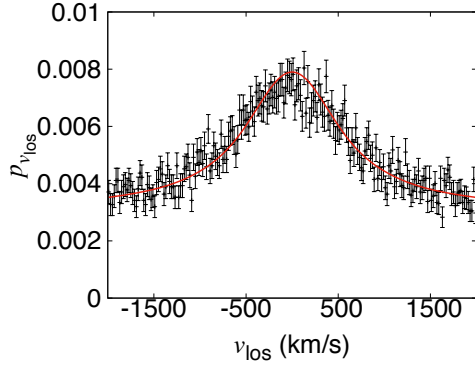
Figure 4.43: Same as Fig. 4.42, but for data-4.



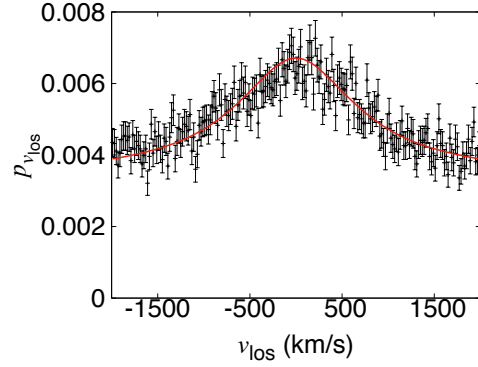
(a)  $2 \text{ Mpc}/h < r_{\text{proj}} < 3 \text{ Mpc}/h$   
 $\chi^2/\text{dof} = 0.85$ , and  
 $\Delta p_{v_{\text{los}}}^2/\text{dof} = 0.48 \times 10^{-6}$



(b)  $4 \text{ Mpc}/h < r_{\text{proj}} < 5 \text{ Mpc}/h$   
 $\chi^2/\text{dof} = 0.80$ , and  
 $\Delta p_{v_{\text{los}}}^2/\text{dof} = 0.30 \times 10^{-6}$

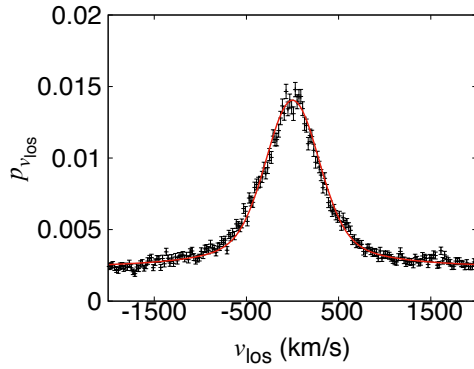


(c)  $8 \text{ Mpc}/h < r_{\text{proj}} < 9 \text{ Mpc}/h$   
 $\chi^2/\text{dof} = 1.01$ , and  
 $\Delta p_{v_{\text{los}}}^2/\text{dof} = 0.22 \times 10^{-6}$

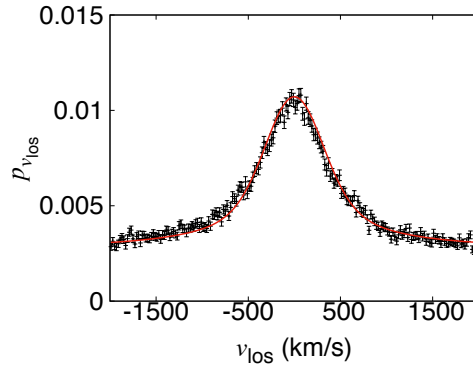


(d)  $11 \text{ Mpc}/h < r_{\text{proj}} < 12 \text{ Mpc}/h$   
 $\chi^2/\text{dof} = 1.10$ , and  
 $\Delta p_{v_{\text{los}}}^2/\text{dof} = 0.19 \times 10^{-6}$

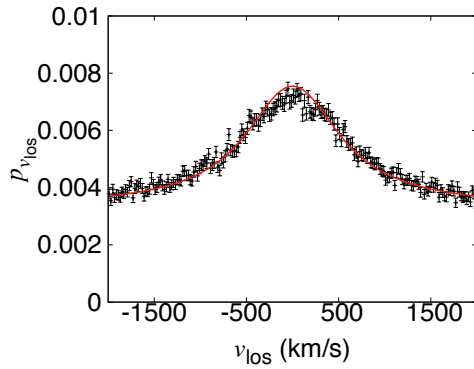
Figure 4.44: Same as Fig. 4.42, but for data-8.



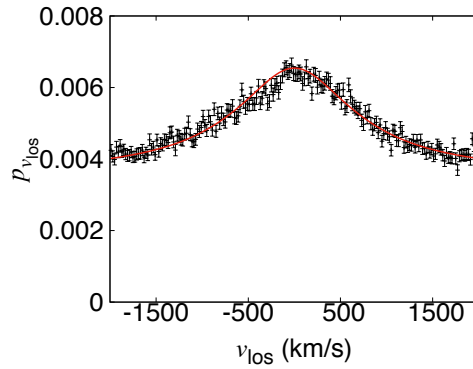
(a)  $2 \text{ Mpc}/h < r_{\text{proj}} < 3 \text{ Mpc}/h$   
 $\chi^2/\text{dof} = 1.64$ , and  
 $\Delta p_{v_{\text{los}}}^2/\text{dof} = 0.16 \times 10^{-6}$



(b)  $4 \text{ Mpc}/h < r_{\text{proj}} < 5 \text{ Mpc}/h$   
 $\chi^2/\text{dof} = 1.58$ , and  
 $\Delta p_{v_{\text{los}}}^2/\text{dof} = 0.10 \times 10^{-6}$



(c)  $8 \text{ Mpc}/h < r_{\text{proj}} < 9 \text{ Mpc}/h$   
 $\chi^2/\text{dof} = 1.42$ , and  
 $\Delta p_{v_{\text{los}}}^2/\text{dof} = 5.77 \times 10^{-8}$



(d)  $11 \text{ Mpc}/h < r_{\text{proj}} < 12 \text{ Mpc}/h$   
 $\chi^2/\text{dof} = 1.37$ , and  
 $\Delta p_{v_{\text{los}}}^2/\text{dof} = 4.16 \times 10^{-8}$

Figure 4.45: Same as Fig. 4.42, but for data-sat.

# Chapter 5

## Measurement of Dynamical Masses from $v_{\text{los}}$ Distribution Functions

In Chapter 4, we constructed a model of the phase space distribution of dark matter halos to compute the PDF of the line-of-sight velocity  $v_{\text{los}}$ . In this Chapter, we discuss how to measure the dynamical mass by using the PDF of  $v_{\text{los}}$ . We also discuss the accuracy of our model constructed in Chapter 4.

### 5.1 Dependence of the PDF of $v_{\text{los}}$ on Cluster Masses

In this Section, we check the host-halo mass dependence of the PDF of  $v_{\text{los}}$ . In Figs. 5.1 and 5.2 we show  $p_{v_{\text{los}}}$  for different cluster masses. To quantify the difference between two different PDFs of  $v_{\text{los}}$ , we use

$$\begin{aligned}\Delta p_{v_{\text{los}},1;2}^2 &\equiv \overline{\{p_{v_{\text{los}},1}(v_{\text{los}}) - p_{v_{\text{los}},2}(v_{\text{los}})\}^2} \\ &= \frac{1}{n_{\text{bin}}} \sum_i^{n_{\text{bin}}} \{p_{v_{\text{los}},1}(v_{\text{los},i}) - p_{v_{\text{los}},2}(v_{\text{los},i})\}^2,\end{aligned}\tag{5.1}$$

as a metric of difference.

We can see a significant difference of  $v_{\text{los}}$  histograms between the middle and high galaxy cluster mass bins, whereas the difference is smaller between the middle and low cluster mass bins. We discuss the origin of this mass dependence in Section 5.2.

In Fig. 5.3, we show the dispersion and kurtosis of  $p_{v_{\text{los}}}$  for each projected radial bin, for each cluster mass bin. The kurtosis is defined as

$$Kurt_{\text{los}} = \frac{\int_{-2000 \text{ km/s}}^{2000 \text{ km/s}} dv_{\text{los}} p_{v_{\text{los}}}^4(v_{\text{los}})}{\sigma_{\text{los}}^4} - 3,\tag{5.2}$$

where  $\sigma_{\text{los}}$  is a dispersion, defined as

$$\sigma_{\text{los}} = \sqrt{\int_{-2000 \text{ km/s}}^{2000 \text{ km/s}} dv_{\text{los}} p_{v_{\text{los}}}^2(v_{\text{los}})}.\tag{5.3}$$

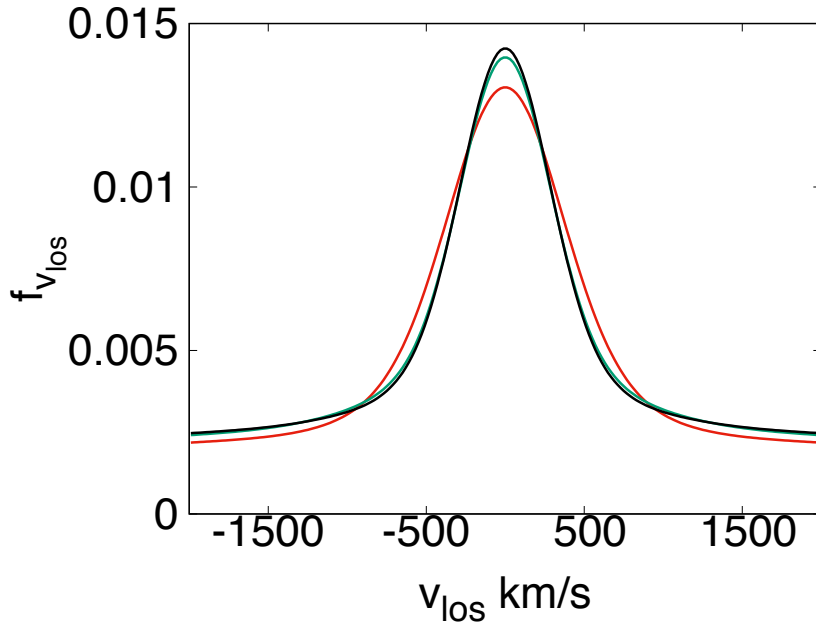
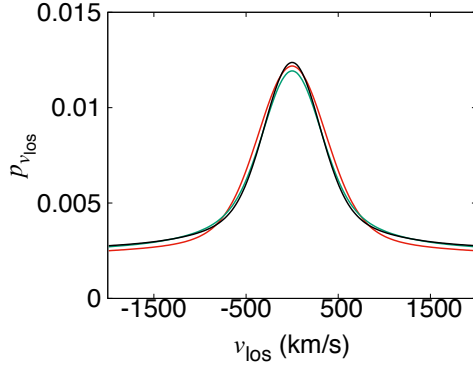
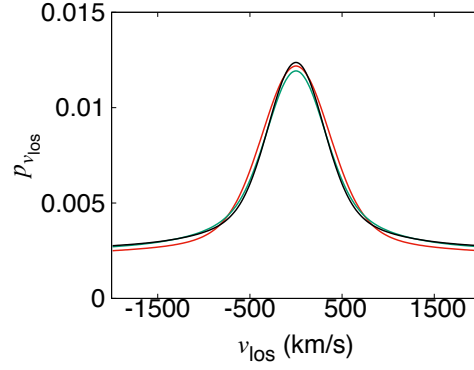


Figure 5.1: The PDF of  $v_{\text{los}}$  for each cluster mass bin at  $2 \text{ Mpc}/h < r_{\text{proj}} < 3 \text{ Mpc}/h$  obtained from our theory. The black line corresponds to the middle galaxy cluster mass bin, red to the high mass bin, and green to the low mass bin.  $\Delta p_{v_{\text{los}}; \text{middle}; \text{high}}^2 = 0.30 \times 10^{-6}$ ,  $\Delta p_{v_{\text{los}}; \text{low}; \text{high}}^2 = 0.22 \times 10^{-6}$ , and  $\Delta p_{v_{\text{los}}; \text{low}; \text{middle}}^2 = 1.14 \times 10^{-8}$ .

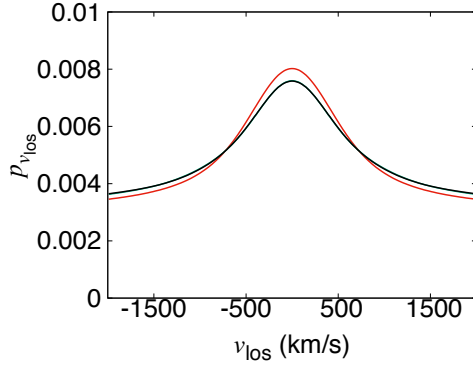
The difference between  $p_{v_{\text{los}}}$  for the middle cluster mass bin and the high is shown in the dispersion and the kurtosis.



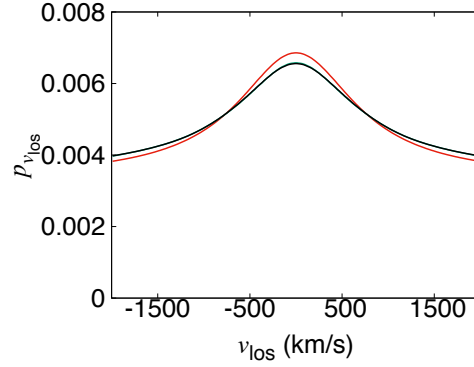
- (a)  $3 \text{ Mpc}/h < r_{\text{proj}} < 4 \text{ Mpc}/h$   
 $\Delta p_{v_{\text{los}};\text{middle};\text{high}}^2 = 0.13 \times 10^{-6}$ ,  
 $\Delta p_{v_{\text{los}};\text{low};\text{high}}^2 = 0.11 \times 10^{-6}$ ,  
 $\Delta p_{v_{\text{los}};\text{low};\text{middle}}^2 = 2.44 \times 10^{-8}$ .



- (b)  $5 \text{ Mpc}/h < r_{\text{proj}} < 6 \text{ Mpc}/h$   
 $\Delta p_{v_{\text{los}};\text{middle};\text{high}}^2 = 0.11 \times 10^{-6}$ ,  
 $\Delta p_{v_{\text{los}};\text{low};\text{high}}^2 = 0.14 \times 10^{-6}$ ,  
 $\Delta p_{v_{\text{los}};\text{low};\text{middle}}^2 = 0.62 \times 10^{-8}$ .



- (c)  $8 \text{ Mpc}/h < r_{\text{proj}} < 9 \text{ Mpc}/h$   
 $\Delta p_{v_{\text{los}};\text{middle};\text{high}}^2 = 5.40 \times 10^{-8}$ ,  
 $\Delta p_{v_{\text{los}};\text{low};\text{high}}^2 = 5.39 \times 10^{-8}$ ,  
 $\Delta p_{v_{\text{los}};\text{low};\text{middle}}^2 = 1.76 \times 10^{-10}$ .



- (d)  $11 \text{ Mpc}/h < r_{\text{proj}} < 12 \text{ Mpc}/h$   
 $\Delta p_{v_{\text{los}};\text{middle};\text{high}}^2 = 2.44 \times 10^{-8}$ ,  
 $\Delta p_{v_{\text{los}};\text{low};\text{high}}^2 = 2.35 \times 10^{-8}$ ,  
 $\Delta p_{v_{\text{los}};\text{low};\text{middle}}^2 = 0.50 \times 10^{-10}$ .

Figure 5.2: Same as Fig. 5.1, but for larger projection radii than  $3 \text{ Mpc}/h$ .

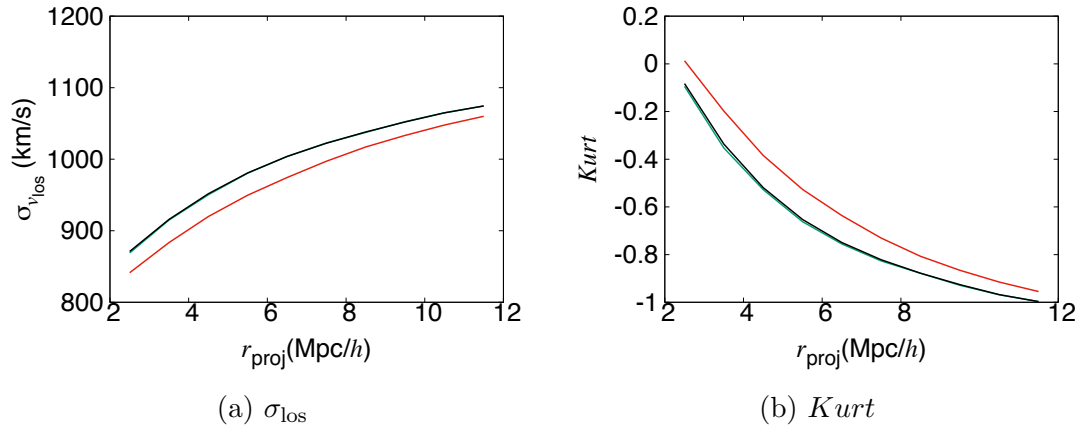


Figure 5.3: The dispersion ( $\sigma_{\text{los}}$ ) and the kurtosis ( $Kurt$ ) as a function of  $r_{\text{proj}}$ , for each cluster mass bin calculated from our model. The black line corresponds to the middle galaxy cluster mass bin, red to high, and green to low.

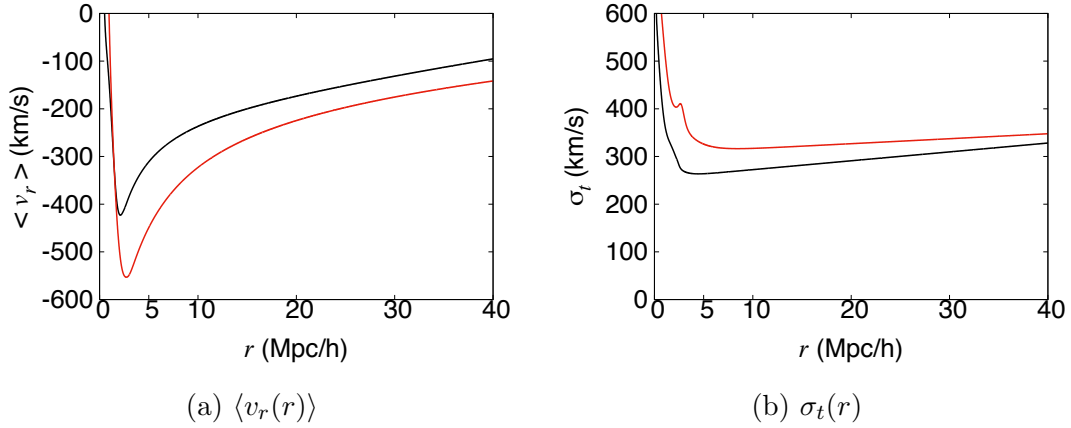


Figure 5.4: Radial distribution of the average of radial velocities of dark matter halos,  $\langle v_r(r) \rangle$ , and the dispersion of tangential velocities,  $\sigma_t(r)$ , for the middle and high cluster mass bins calculated from our theory. The black line corresponds to the middle galaxy cluster mass bin, and red to high.

## 5.2 Origin of Dynamical Mass Dependence of the PDF of $v_{\text{los}}$

In this Section, we explore the relationship between the cluster mass dependence of the PDF of  $v_{\text{los}}$  and the phase space distribution of dark matter halos. As seen in Sections 4.6 and 5.1, our model of the phase space distribution around low mass galaxy clusters may not be accurate enough to allow robust cluster mass measurements. Hence, we focus on the high and middle cluster mass bins.

The most important parameters of the phase space distribution function to the  $v_{\text{los}}$  PDF is the average of  $v_r$ ,  $\langle v_r \rangle$ , and the standard deviation of  $v_t$ ,  $\sigma_t$ . By using  $\alpha$ ,  $\delta$ ,  $\lambda$ ,  $\gamma$ ,  $\xi$ , and  $\mu_r$ , the average of  $v_r$  is described as

$$\langle v_r \rangle = (1 - \alpha) [\xi - \lambda \{\exp(\delta^{-2})\}^{1/2} \sinh \gamma / \delta] + \alpha \mu_r, \quad (5.4)$$

and by using  $\alpha$ ,  $\sigma_{t,\text{infall}}$ , and  $\sigma_{t,\text{SB}}$ ,  $\sigma_t$  is described as

$$\sigma_t = \sqrt{(1 - \alpha) \sigma_{t,\text{infall}}^2 + \alpha \sigma_{t,\text{SB}}^2}. \quad (5.5)$$

In Fig. 5.4, we show  $\langle v_r \rangle$  and  $\sigma_t$  for each cluster mass bin. We can see that more massive halos have lower  $\langle v_r \rangle$  and higher  $\sigma_t$ .

Next, we discuss how these differences of  $\langle v_r(r) \rangle$  and  $\sigma_t$  affect the PDF of  $v_{\text{los}}$ . Following eq. (4.14), we define  $p_{v_{\text{los}}}(v_{\text{los}}, r_{\text{proj}}, d_{\text{los},\text{min}}, d_{\text{los},\text{max}})$  as

$$p_{v_{\text{los}}}(v_{\text{los}}, r_{\text{proj}}, d_{\text{los},\text{min}}, d_{\text{los},\text{max}}) = \frac{2}{N(r_{\text{proj}})} \int_{-2000 \text{ km/s}}^{2000 \text{ km/s}} dv_r \int_{-2000 \text{ km/s}}^{2000 \text{ km/s}} dv_t \int_{d_{\text{los},\text{min}}}^{d_{\text{los},\text{max}}} dd_{\text{los}} n(r) p_v(v_r, v_t, r) \delta_D(v_{\text{los}} - v'_{\text{los}}). \quad (5.6)$$

Table 5.1: Sets of parameters shown in Fig. 5.5

color	range of $r_{\text{proj}}$	$d_{\text{los,min}}$	$d_{\text{los,max}}$
red	2.0 Mpc/h – 3.0 Mpc/h	0 Mpc/h	5.0 Mpc/h
green	2.0 Mpc/h – 3.0 Mpc/h	5.0 Mpc/h	10.0 Mpc/h
blue	2.0 Mpc/h – 3.0 Mpc/h	10.0 Mpc/h	20.0 Mpc/h
magenta	2.0 Mpc/h – 3.0 Mpc/h	20.0 Mpc/h	40.0 Mpc/h
black	2.0 Mpc/h – 3.0 Mpc/h	0 Mpc/h	40.0 Mpc/h

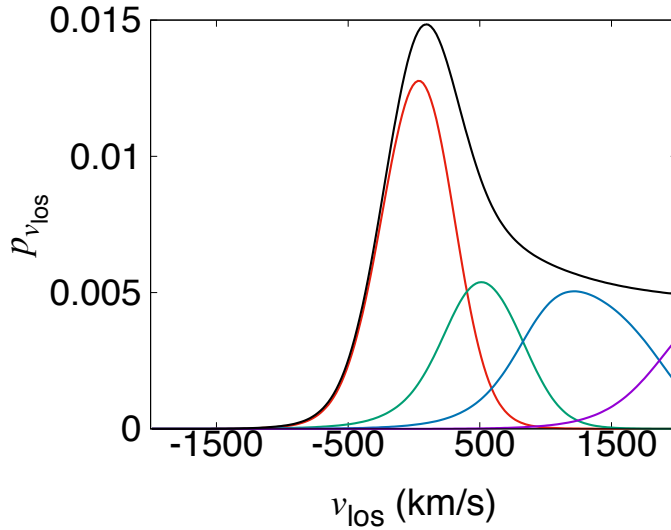


Figure 5.5: Comparison of  $p_{v_{\text{los}}}(v_{\text{los}}, r_{\text{proj}}, d_{\text{los,min}}, d_{\text{los,max}})$  for five sets of parameters for the middle galaxy cluster mass bin. We show sets of parameters in Table 5.1.

In Fig. 5.5, we show  $p_{v_{\text{los}}}(v_{\text{los}}, r_{\text{proj}}, d_{\text{los,min}}, d_{\text{los,max}})$  for five sets of parameters for the middle galaxy cluster mass bin. We show set of parameters in Table 5.1.

We can see that high  $d_{\text{los}}$  segments contribute to the tail of the  $v_{\text{los}}$  PDF, and low  $d_{\text{los}}$  segments contribute to the peak. These are explained as follow. At high  $d_{\text{los}}$  segments, the Hubble flow significantly increase  $v_{\text{los}}$ , whereas at low  $d_{\text{los}}$  segments, the contribution of the Hubble flow is small so that we observe peculiar velocities directly. We then check the dependence of each part of  $p_{v_{\text{los}}}(v_{\text{los}}, r_{\text{proj}}, d_{\text{los,min}}, d_{\text{los,max}})$  on cluster masses.

First, we focus on a  $d_{\text{los}}$  segment with  $d_{\text{los}} \ll r_{\text{proj}}$ . In the left panel of Fig. 5.6, we compare  $p_{v_{\text{los}}}(v_{\text{los}}, r_{\text{proj}}, d_{\text{los,min}}, d_{\text{los,max}})$  for the middle galaxy cluster mass bin at  $2.0 \text{ Mpc}/h < r_{\text{proj}} < 3.0 \text{ Mpc}/h$ ,  $(d_{\text{los,min}}, d_{\text{los,max}}) = (0 \text{ Mpc}/h, 1.0 \text{ Mpc}/h)$  and  $2.0 \text{ Mpc}/h < r_{\text{proj}} < 3.0 \text{ Mpc}/h$ ,  $(d_{\text{los,min}}, d_{\text{los,max}}) = (0 \text{ Mpc}/h, 40.0 \text{ Mpc}/h)$ . We confirm that at low  $d_{\text{los}}$ ,  $p_{v_{\text{los}}}(v_{\text{los}}, r_{\text{proj}}, d_{\text{los,min}}, d_{\text{los,max}})$  contributes to the peak.

In the right panel of Fig. 5.6, we compare  $p_{v_{\text{los}}}(v_{\text{los}}, r_{\text{proj}}, d_{\text{los,min}}, d_{\text{los,max}})$  for the middle and high cluster mass bins at  $2.0 \text{ Mpc}/h < r_{\text{proj}} < 3.0 \text{ Mpc}/h$  and  $(d_{\text{los,min}}, d_{\text{los,max}}) = (0 \text{ Mpc}/h, 1.0 \text{ Mpc}/h)$ . We can see that  $p_{v_{\text{los}}}(v_{\text{los}}, r_{\text{proj}}, d_{\text{los,min}}, d_{\text{los,max}})$  for the high galaxy cluster mass bin has a larger width than the middle one, because of larger  $\sigma_t(r)$  for the

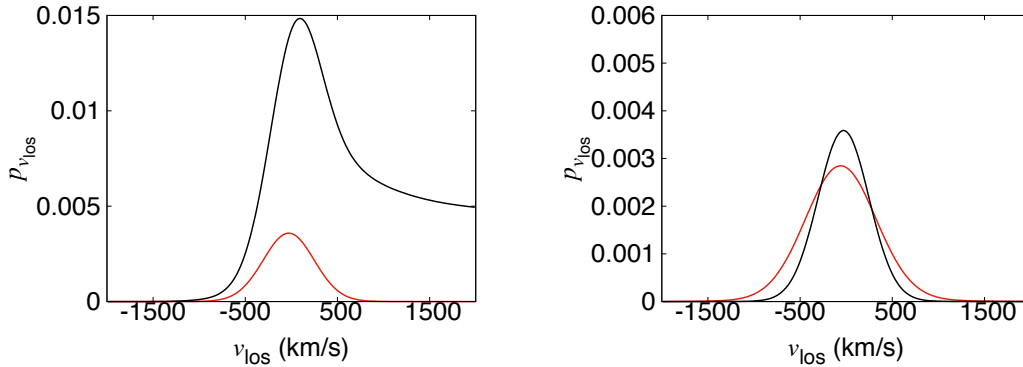


Figure 5.6: Left panel: Comparison between  $p_{v_{\text{los}}}(v_{\text{los}}, r_{\text{proj}}, d_{\text{los,min}}, d_{\text{los,max}})$  for  $2.0 \text{ Mpc}/h < r_{\text{proj}} < 3.0 \text{ Mpc}/h$ ,  $(d_{\text{los,min}}, d_{\text{los,max}}) = (0 \text{ Mpc}/h, 1.0 \text{ Mpc}/h)$  (red line) and  $2.0 \text{ Mpc}/h < r_{\text{proj}} < 3.0 \text{ Mpc}/h$ ,  $(d_{\text{los,min}}, d_{\text{los,max}}) = (0 \text{ Mpc}/h, 40.0 \text{ Mpc}/h)$  (black line) for the middle galaxy cluster mass bin. Right panel: Comparison between  $p_{v_{\text{los}}}(v_{\text{los}}, r_{\text{proj}}, d_{\text{los,min}}, d_{\text{los,max}})$  for the middle galaxy cluster mass bin (black line) and the high one (red line) at  $2.0 \text{ Mpc}/h < r_{\text{proj}} < 3.0 \text{ Mpc}/h$  and  $(d_{\text{los,min}}, d_{\text{los,max}}) = (0 \text{ Mpc}/h, 1.0 \text{ Mpc}/h)$ .

high mass bin as we saw in Fig. 5.4. Note that at  $d_{\text{los}} \ll r_{\text{proj}}$  segments,  $v_r$  does not contribute to the PDF of  $v_{\text{los}}$  as we saw in Section 4.6.

Next we focus on a  $d_{\text{los}}$  segment with  $d_{\text{los}} > r_{\text{proj}}$ . In the left panel of Fig. 5.7, we show a plot similar to the left panel of Fig. 5.6, but we change  $(d_{\text{los,min}}, d_{\text{los,max}})$  from  $(0 \text{ Mpc}/h, 1.0 \text{ Mpc}/h)$  to  $(5.0 \text{ Mpc}/h, 10.0 \text{ Mpc}/h)$ . This segment contributes to the edge of the peak of  $v_{\text{los}}$  PDF. In the right panel of Fig. 5.7, we a plot similar to the right panel of Fig. 5.6, but changed  $(d_{\text{los,min}}, d_{\text{los,max}})$  from  $(0 \text{ Mpc}/h, 1.0 \text{ Mpc}/h)$  to  $(5.0 \text{ Mpc}/h, 10.0 \text{ Mpc}/h)$ . In this segment,  $v_r$ ,  $v_t$ , and the Hubble flow contributes to  $v_{\text{los}}$ . While the Hubble flow is dominated,  $v_r$  also makes non-negligible contribution to the PDF. Since higher mass clusters have lower  $v_r$  (see Fig. 5.4), they shift  $p_{v_{\text{los}}}(v_{\text{los}}, r_{\text{proj}}, d_{\text{los,min}}, d_{\text{los,max}})$  to the lower mean  $v_{\text{los}}$  more significantly, which also results in the wider width of the PDF.

Finally, we focus on a  $d_{\text{los}}$  segment with very large  $d_{\text{los}}$ . In the left panel of Fig. 5.8, we show a plot similar to the left panel of Fig. 5.6, but we change  $(d_{\text{los,min}}, d_{\text{los,max}})$  from  $(0 \text{ Mpc}/h, 1.0 \text{ Mpc}/h)$  to  $(10.0 \text{ Mpc}/h, 20.0 \text{ Mpc}/h)$ . This segment contributes to the tail of the  $v_{\text{los}}$  PDF. In the right panel of Fig. 5.8, we show a plot similar to the right panel of Fig. 5.6, but we change  $(d_{\text{los,min}}, d_{\text{los,max}})$  from  $(0 \text{ Mpc}/h, 1.0 \text{ Mpc}/h)$  to  $(10.0 \text{ Mpc}/h, 20.0 \text{ Mpc}/h)$ . In this segment,  $v_{\text{los}}$  are determined mostly by the Hubble flow and  $v_r$ . Note that the high galaxy cluster mass bin contains more halos with  $v_{\text{los}} < 2000 \text{ km/s}$  than the middle one, because high mass clusters have higher  $v_r$  on average, which pulls more halos from  $v_{\text{los}} > 2000 \text{ km/s}$  to  $v_{\text{los}} < 2000 \text{ km/s}$ . In addition, the high mass cluster bin have more halos at small  $r$  than the middle one. Hence, the relative amplitude of the segment at large  $d_{\text{los}}$  is smaller for the higher cluster mass bin.

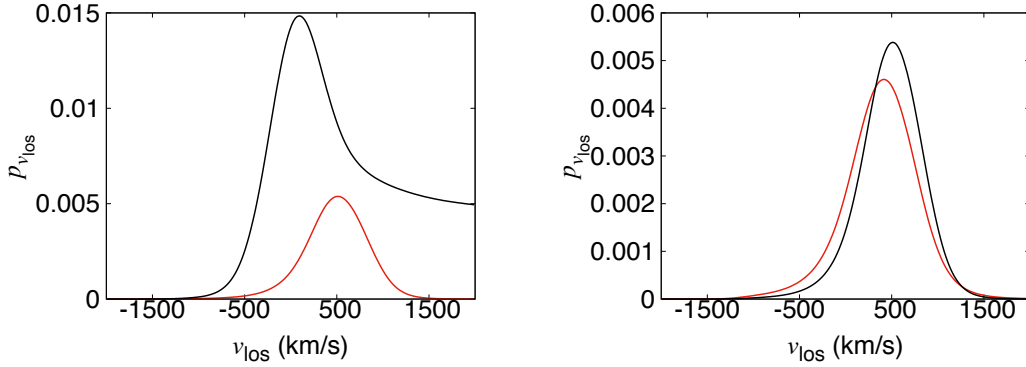


Figure 5.7: Left panel: Comparison between  $p_{v_{\text{los}}}(v_{\text{los}}, r_{\text{proj}}, d_{\text{los, min}}, d_{\text{los, max}})$  for  $2.0 \text{ Mpc}/h < r_{\text{proj}} < 3.0 \text{ Mpc}/h$ ,  $(d_{\text{los, min}}, d_{\text{los, max}}) = (5.0 \text{ Mpc}/h, 10.0 \text{ Mpc}/h)$  (red line) and  $2.0 \text{ Mpc}/h < r_{\text{proj}} < 3.0 \text{ Mpc}/h$ ,  $(d_{\text{los, min}}, d_{\text{los, max}}) = (0 \text{ Mpc}/h, 40.0 \text{ Mpc}/h)$  (black line) for the middle galaxy cluster mass bin. Right panel: Comparison between  $p_{v_{\text{los}}}(v_{\text{los}}, r_{\text{proj}}, d_{\text{los, min}}, d_{\text{los, max}})$  for the middle galaxy cluster mass bin (black line) and the high one (red line) at  $2.0 \text{ Mpc}/h < r_{\text{proj}} < 3.0 \text{ Mpc}/h$  and  $(d_{\text{los, min}}, d_{\text{los, max}}) = (5.0 \text{ Mpc}/h, 10.0 \text{ Mpc}/h)$ .

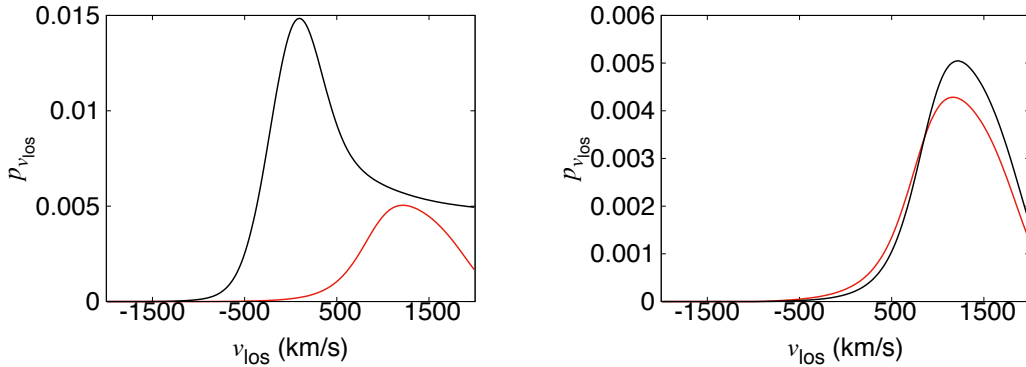


Figure 5.8: Left panel: Comparison between  $p_{v_{\text{los}}}(v_{\text{los}}, r_{\text{proj}}, d_{\text{los, min}}, d_{\text{los, max}})$  for  $2.0 \text{ Mpc}/h < r_{\text{proj}} < 3.0 \text{ Mpc}/h$ ,  $(d_{\text{los, min}}, d_{\text{los, max}}) = (10.0 \text{ Mpc}/h, 20.0 \text{ Mpc}/h)$  (red line) and  $2.0 \text{ Mpc}/h < r_{\text{proj}} < 3.0 \text{ Mpc}/h$ ,  $(d_{\text{los, min}}, d_{\text{los, max}}) = (0 \text{ Mpc}/h, 40.0 \text{ Mpc}/h)$  (black line) for the middle galaxy cluster mass bin. Right panel: Comparison between  $p_{v_{\text{los}}}(v_{\text{los}}, r_{\text{proj}}, d_{\text{los, min}}, d_{\text{los, max}})$  for the middle galaxy cluster mass bin (black line) and the high one (red line) at  $2.0 \text{ Mpc}/h < r_{\text{proj}} < 3.0 \text{ Mpc}/h$  and  $(d_{\text{los, min}}, d_{\text{los, max}}) = (10.0 \text{ Mpc}/h, 20.0 \text{ Mpc}/h)$ .

### 5.3 Accuracy of Mass Estimation

Using our model PDF of  $v_{\text{los}}$ , we can estimate the accuracy of cluster mass estimations from observations of the stacked phase space distribution. Here we assume only the Poisson errors as measurement errors. When we have  $N_{\text{gal}}$  spectroscopic galaxies in a segment, the accuracy of detecting the difference between the PDFs of  $v_{\text{los},1}$  and  $v_{\text{los},2}$  is

$$(\Delta\chi^2)^{1/2} = \left[ N_{\text{gal}} \times \sum_i^{n_{\text{bin}}} \frac{\{p_{v_{\text{los},1}}(v_{\text{los},i}) - p_{v_{\text{los},2}}(v_{\text{los},i})\}^2}{\{p_{v_{\text{los},1}}(v_{\text{los},i})\}} \right]^{1/2}. \quad (5.7)$$

Note that  $n_{\text{bin}}$  is the number of  $v_{\text{los}}$  bins. We approximate  $1\sigma$  error of the Poisson error for  $N$  to  $\sqrt{N}$ .

When we estimate cluster masses by using the PDF of  $v_{\text{los},1}$ , we have some independent data, e.g., the PDF for  $2.0 \text{ Mpc}/h < r_{\text{proj}} < 3.0 \text{ Mpc}/h$  and the PDF for  $3.0 \text{ Mpc}/h < r_{\text{proj}} < 4.0 \text{ Mpc}/h$ . We calculate the accuracy of detecting cluster masses by combining the PDFs at different projected radii as

$$(\Delta\chi^2)^{1/2} = \left[ \sum_l N_{\text{gal},l} \times \sum_i^{n_{\text{bin}}} \frac{\{p_{v_{\text{los},1,l}}(v_{\text{los},i}) - p_{v_{\text{los},2,l}}(v_{\text{los},i})\}^2}{\{p_{v_{\text{los},1,l}}(v_{\text{los},i})\}} \right]^{1/2}. \quad (5.8)$$

We estimate the minimum number of galaxies to detect the difference between the high and middle cluster mass bins at  $1\sigma$ . We combine the  $v_{\text{los}}$  PDFs in the range  $2.0 \text{ Mpc}/h < r_{\text{proj}} < 12.0 \text{ Mpc}/h$  here. By using our model PDF of  $v_{\text{los}}$  and eq. (5.8), we obtain the minimum number of galaxies as

$$N_{\text{gal}} = \left[ \sum_l p_{\text{gal},l} \times \sum_i^{n_{\text{bin}}} \frac{\{p_{v_{\text{los},1,l}}(v_{\text{los},i}) - p_{v_{\text{los},2,l}}(v_{\text{los},i})\}^2}{\{p_{v_{\text{los},1,l}}(v_{\text{los},i})\}} \right]^{-1} \sim 350, \quad (5.9)$$

where,  $p_{\text{gal},l}$  is the fractional number of dark matter halos in the  $l$ -th segment, which satisfy

$$\sum_l p_{\text{gal},l} = 1. \quad (5.10)$$

We obtain  $p_{\text{gal},l}$  from our simulation.

The number of spectroscopic galaxy at  $2.0 \text{ Mpc}/h < r_{\text{proj}} < 12.0 \text{ Mpc}/h$  for  $20 < N < 60$  and  $0.1 < z < 0.4$  galaxy clusters observed in SDSS/BOSS (Dawson et al. 2013) is about 150,000. Note that we use richness  $N$  estimated by CAMIRA (Oguri 2014). We can determine the mean mass of galaxy clusters observed in SDSS/BOSS by using the PDF of  $v_{\text{los}}$  at  $2.0 \text{ Mpc}/h < r_{\text{proj}} < 12.0 \text{ Mpc}/h$  with an accuracy of

$$\left( \frac{M_{\text{high}}}{M_{\text{middle}}} \right)^{\frac{350}{150000}} \sim 1.04 \rightarrow 4\%, \quad (5.11)$$

at  $1\sigma$ , where  $M_{\text{high}}$  and  $M_{\text{middle}}$  are the mean cluster mass of the high and middle cluster mass bin.

## 5.4 Systematic Errors

In this Section, we discuss the systematic errors of the dynamical mass of clusters measured by using our model. Here, we estimate the effect of two systematic errors. One is the satellite-halo and sub-halo mass dependence, and the other is an inaccuracy of our model of the phase space distribution. We also discuss about other source of systematic errors in this Section.

### 5.4.1 Dependence of the PDF of $v_{\text{los}}$ on Satellite-Halo and Sub-Halo Masses

In observations, to measure the  $v_{\text{los}}$  PDF we use redshifts of galaxies whose corresponding halo masses may not be obtained accurately. Hence, the dependence of the PDF of  $v_{\text{los}}$  on satellite-halo and sub-halo masses can be regarded as a systematic error of the PDF of  $v_{\text{los}}$ . To estimate the rough amplitude of the error, we have to estimate the satellite-halo and sub-halo mass dependence of the PDF of  $v_{\text{los}}$ .

In Figs. 5.9 and 5.10, we show the PDF of  $v_{\text{los}}$  from theory for each dataset defined in Section 4.7. By comparing these Figures with Figs. 5.1 and 5.2, we can see that the dependence of the PDF of  $v_{\text{los}}$  on satellite-halo and sub-halo masses is not very large, particularly when we focus on galaxy clusters more massive than  $10^{11} M_{\odot}$ . We can also see that  $\Delta p_{v_{\text{los}}}^2$  shown in Figs. 5.9 and 5.10 are less than one fifth of those shown in Figs. 5.1 and 5.2.

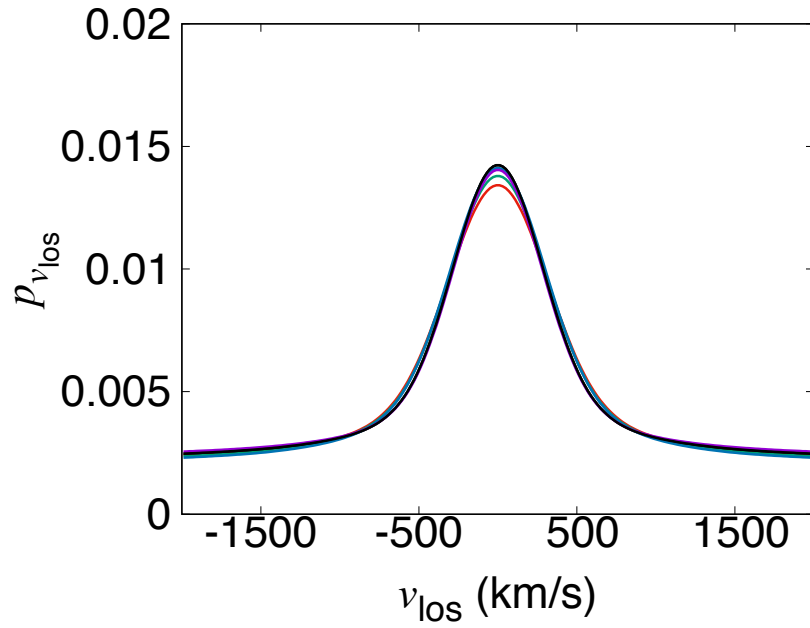
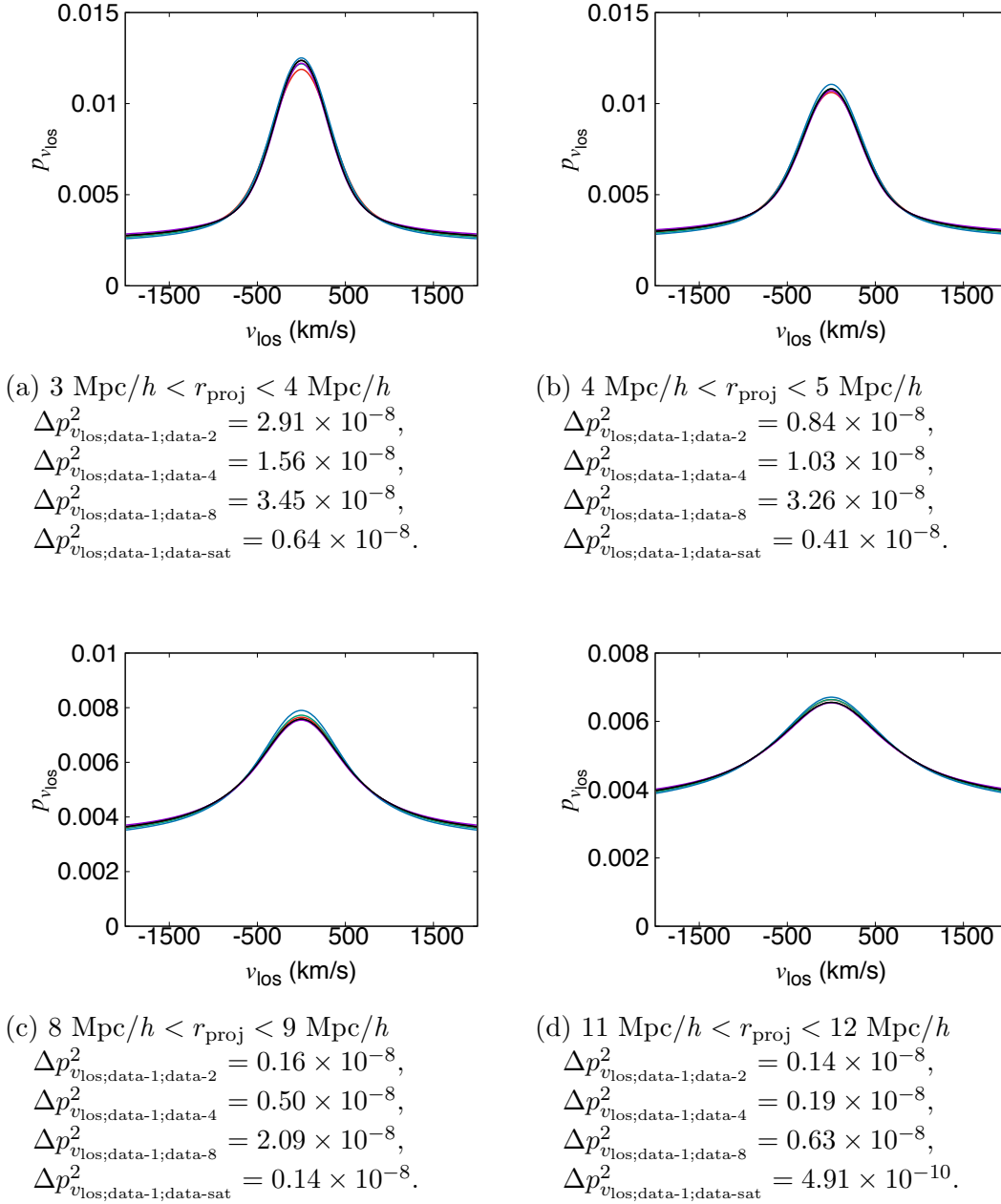


Figure 5.9: PDFs of  $v_{\text{los}}$  for different satellite-halo and sub-halo masses at  $2 \text{ Mpc}/h < r_{\text{proj}} < 3 \text{ Mpc}/h$  obtained from our theory. The black line corresponds to data-1, red corresponds to data-2, green to data-4, green to data-8, and magenta to data-sat.  $\Delta p_{v_{\text{los};\text{data-1};\text{data-2}}^2} = 7.30 \times 10^{-8}$ ,  $\Delta p_{v_{\text{los};\text{data-1};\text{data-4}}^2} = 3.35 \times 10^{-8}$ ,  $\Delta p_{v_{\text{los};\text{data-1};\text{data-8}}^2} = 3.20 \times 10^{-8}$ , and  $\Delta p_{v_{\text{los};\text{data-1};\text{data-sat}}^2} = 0.81 \times 10^{-8}$ .

Figure 5.10: Same as Fig. 5.9, but for larger projection radii than  $3 \text{ Mpc}/h$ .

### 5.4.2 Inaccuracy of Our Model

Our model PDF of  $v_{\text{los}}$  is not perfect as seen in Section 4.6. When we compare the PDF from theory to that from mock in Section 4.6, there are two types of residuals between these two PDFs. One is a statical error, and the other is an imperfection of our model. Now,  $\chi^2$  for the PDF of  $v_{\text{los}}$  is described as

$$\chi_{\text{los}}^2 = \sum_i^{\text{dof}} \frac{\{p_{v_{\text{los}}}(v_{\text{los},i}) - y_i\}^2}{\sigma_i^2}, \quad (5.12)$$

and residual ( $\Delta p^2$ ) is described as

$$\Delta p_{\text{los}}^2 = \sum_i^{\text{dof}} \{p_{\text{los}}(v_{\text{los},i}) - y_i\}^2, \quad (5.13)$$

where dof is the number of datapoint we have from mock observations, and  $\sigma_i$  is a normalized Poisson error of  $i$ -th datapoint. We can rewrite eq. (5.12) as

$$\begin{aligned} \chi_{\text{los}}^2 &= \sum_i^{\text{dof}} \frac{[\{p_{v_{\text{los};\text{ture}}}(v_{\text{los},i}) - y_i\} + \{p_{v_{\text{los}}}(v_{\text{los},i}) - p_{v_{\text{los};\text{ture}}}(v_{\text{los},i})\}]^2}{\sigma_i^2} \\ &= \sum_i^{\text{dof}} \frac{\{p_{v_{\text{los};\text{ture}}}(v_{\text{los},i}) - y_i\}^2}{\sigma_i^2} \\ &\quad + \sum_i^{\text{dof}} \frac{\{p_{v_{\text{los}}}(v_{\text{los},i}) - p_{v_{\text{los};\text{ture}}}(v_{\text{los},i})\}^2}{\sigma_i^2} \\ &\quad + \sum_i^{\text{dof}} 2 \frac{\{p_{v_{\text{los};\text{ture}}}(v_{\text{los},i}) - y_i\} \times \{p_{v_{\text{los}}}(v_{\text{los},i}) - p_{v_{\text{los};\text{ture}}}(v_{\text{los},i})\}}{\sigma_i^2}, \end{aligned} \quad (5.14)$$

where  $p_{v_{\text{los};\text{ture}}}$  is the true PDF of  $v_{\text{los}}$ . The first term of the second low of eq. (5.14) corresponds to the Poisson error, the second term of the second low corresponds to the difference between the  $v_{\text{los}}$  PDF from our model and the true PDF, and the third term is the cross term. Because the Poisson error does not correlate with  $p_{v_{\text{los}}}(v_{\text{los},i}) - p_{v_{\text{los};\text{ture}}}(v_{\text{los},i})$ , the cross term reduces to zero when we have sufficiently narrow  $v_{\text{los}}$  bins. Our dof of the  $v_{\text{los}}$  PDF from the mock is 200, so we neglect the cross term. Comparing the true PDF to the PDF from the mock,  $\chi^2$  must obey the  $\chi^2$  distribution. When dof is enough large,  $\chi^2$  distribution asymptotes to Gaussian distribution with its average equal to dof and the standard deviation equal to  $\sqrt{2 \times \text{dof}}$ . Hence, we can rewrite eq. (5.14) as

$$\chi_{\text{los}}^2 - \text{dof} \sim \sum_i^{\text{dof}} \frac{\{p_{v_{\text{los}}}(v_{\text{los},i}) - p_{v_{\text{los};\text{ture}}}(v_{\text{los},i})\}^2}{\sigma_i^2}. \quad (5.15)$$

By using eq. (5.15), we can estimate  $\{p_{v_{\text{los}}}(v_{\text{los}}) - p_{v_{\text{los};\text{ture}}}(v_{\text{los}})\}^2$  roughly from  $\chi_{\text{los}}^2$  and the typical amplitude of error bars.

Table 5.2: Summary of the new galaxy cluster mass bins. We adopt  $M_{\text{vir}}$  as the cluster masses.

Cluster mass bin name	Lower limit	Higher limit	Mean value
N1	$3.06 \times 10^{14} M_{\odot}$	-	$5.12 \times 10^{14} M_{\odot}$
N2	$2.05 \times 10^{14} M_{\odot}$	$3.06 \times 10^{14} M_{\odot}$	$2.47 \times 10^{14} M_{\odot}$
N3	$1.63 \times 10^{14} M_{\odot}$	$2.05 \times 10^{14} M_{\odot}$	$1.82 \times 10^{14} M_{\odot}$
N4	$1.36 \times 10^{14} M_{\odot}$	$1.63 \times 10^{14} M_{\odot}$	$1.49 \times 10^{14} M_{\odot}$
N5	$1.19 \times 10^{14} M_{\odot}$	$1.36 \times 10^{14} M_{\odot}$	$1.27 \times 10^{14} M_{\odot}$
N6	$1.06 \times 10^{14} M_{\odot}$	$1.19 \times 10^{14} M_{\odot}$	$1.12 \times 10^{14} M_{\odot}$
N7	$9.48 \times 10^{13} M_{\odot}$	$1.06 \times 10^{14} M_{\odot}$	$1.00 \times 10^{14} M_{\odot}$

We conclude that  $\{p_{v_{\text{los}}}(v_{\text{los}}) - p_{v_{\text{los};\text{ture}}}(v_{\text{los}})\}^2$  less than one third of  $\Delta p_{v_{\text{los}}}^2$  shown with Fig. 5.1 and 5.2.

To estimate the inaccuracy of our model more quantitatively, we calculate  $\chi_{\text{los}}^2$  for our theoretical model PDF but shifting cluster mass bins of Mock PDFs. We set new galaxy cluster mass bins so that each cluster mass bin contains 300 galaxy clusters. In Table 5.2, we show the summary of our new galaxy cluster mass bins. Note that we adopt  $1.0 \times 10^{11} M_{\odot}$  as the lower limit of satellite-halos and sub-halos mass for these new galaxy cluster mass bins.

We can estimate the systematic errors of cluster masses estimated from the stacked  $v_{\text{los}}$  PDF by calculating  $\chi_{\text{los}}^2$  with  $p_{v_{\text{los}}}$  constructed in Chapter 4 for the middle and high galaxy cluster mass bins and histograms obtained directly from our  $N$ -body simulation for the new galaxy cluster mass bins. If our theoretical model is perfect, the  $\chi_{\text{los}}^2$  takes the minimum value with the cluster mass bin whose cluster masses are same as cluster masses used to construct  $p_{v_{\text{los}}}$ .

In Fig. 5.11, we show  $\chi_{\text{los}}^2$  defined in eq. (5.12). We use  $p_{v_{\text{los}}}$  constructed in Chapter 4 for the middle and high galaxy cluster mass bins and histograms obtained directly from our  $N$ -body simulation for the new galaxy cluster mass bins listed in Table 5.2, which are different from the three cluster mass bins that are used for our main analysis in previous sections. First, Fig. 5.11 indicates that  $\chi_{\text{los}}^2$  indeed takes the minimum value at least for the middle cluster mass bin, which indicates that our new methodology to constrain cluster masses using the stacked  $v_{\text{los}}$  PDF works. For the high cluster mass bin, the  $\chi_{\text{los}}^2$  minimum is not clearly seen because of the limited cluster mass range originating from the limited simulation box size. Next, the cluster mass that corresponds to  $\chi_{\text{los};\text{min}}^2$  deviates from the input mean mass of clusters used to construct the theoretical model PDF. Therefore this test indicates that the systematic errors on estimating cluster masses do exist and are not negligible. The systematic error is smaller than the mass difference of cluster masses between the middle and high mass bins for our original analysis, which is consistent with our simple analytic estimate presented above.

Together with the dependence of satellite-halo and sub-halo masses, we find that these systematic errors are smaller than the difference of the PDFs between the middle and

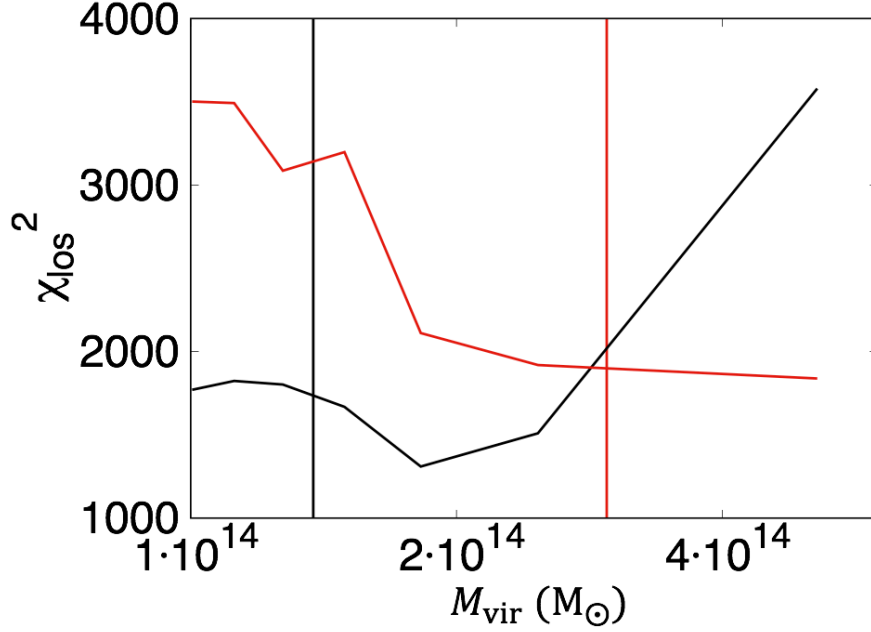


Figure 5.11: Comparison of  $\chi_{\text{los}}^2$  for each galaxy cluster mass bins. The vertical axis is  $\chi_{\text{los}}^2$  summed up for  $2 \text{ Mpc}/h < r_{\text{proj}} < 12 \text{ Mpc}/h$ . The horizontal axis is the mean value of cluster masses within each cluster mass bin. The black line is  $\chi_{\text{los}}^2$  calculated by using  $p_{v_{\text{los}}}$  for the middle galaxy cluster mass bin, and the red line is by using the high one. The vertical lines show the mean values of the middle (black) and the high (red) galaxy cluster mass bins.

high cluster mass bins as we saw in Fig. 5.11, but can make significant contributions to the analysis of observations that we discussed in Section 5.4.1. In principle, we can disentangle these systematic errors from the cluster mass estimate by taking advantage of the difference of these effects on the shape of the  $v_{\text{los}}$  PDF. Our analysis presented here indicates that these potential sources of the systematic error should be addressed carefully, which we leave for future work.

### 5.4.3 Measurement Errors of Galaxy Redshifts

In observation, we cannot measure the exact pairwise line-of-sight velocities, because of measurement errors of galaxy redshifts (see also Section 3.1). The measurement errors of galaxy redshifts distort the PDF of the line-of-sight velocity as

$$p_{v_{\text{los}}:\text{obs}}(v_{\text{los}}) = \int_{-\infty}^{\infty} dv'_{\text{los}} p_{v_{\text{los}}:\text{true}}(v'_{\text{los}}) E(v_{\text{los}} - v'_{\text{los}}), \quad (5.16)$$

where  $p_{v_{\text{los}}:\text{obs}}$  and  $p_{v_{\text{los}}:\text{true}}$  are the observed and the true PDFs of the line-of-sight velocity. Note that  $E$  represents the effect of measurement errors of spectroscopic galaxy redshifts. In the case that measurement errors of spectroscopic galaxy redshifts follow the Gaussian distribution, we can describe  $E$  as

$$E(x) = \frac{1}{\sigma_z \sqrt{2\pi}} \exp \frac{-x^2}{2\sigma_z^2}, \quad (5.17)$$

where  $\sigma_z$  is the root-mean-square of measurement errors of line-of-sight velocities.

Since we focus on  $-2000 \text{ km/s} < v_{\text{los}} < 2000 \text{ km/s}$ , we can regard  $|z_{\text{sat}} - z_{\text{cen}}| \ll 1 + z_{\text{cen}}$ . Hence, eq. (3.3) is rewritten as

$$\Delta v_{\text{los}} \sim \frac{c}{1 + z_{\text{cen}}} \sqrt{\Delta z_{\text{sat}}^2 + \Delta z_{\text{cen}}^2}. \quad (5.18)$$

As the typical measurement error of spectroscopic galaxy redshifts is  $10^{-4}$ , we see  $\sigma_z \sim 40 \text{ km/s}$ . As long as measurement errors of spectroscopic galaxies are well understood, we can include the effect of measurement errors like this to make fair comparisons with observed  $v_{\text{los}}$  PDFs.

### 5.4.4 Miscentering

In observation, we use BCGs defined by cluster finding methods as centers of clusters, whereas in simulations, we determine the most bounded dark matter particles as centers of clusters according to **Rockstar** (Behroozi et al. 2013b). These BCGs may not correspond to the centers defined in our simulation. This miscentering causes systematic errors.

In Rykoff et al. (2016), they compare the sky positions of the BCGs of the clusters observed by SDSS (York et al. 2000) defined in their cluster finding method (Rykoff et al. 2014) with the sky positions of the X-ray peak of the clusters observed by *Chandra* and *XMM* X-ray observations. In Rykoff et al. (2016), they also compare the sky positions of the BCGs with the sky position of the peak of SZ signals observed from the South Pole Telescope SZ cluster survey (Bleem et al. 2015). While we want to estimate distances between centers of clusters defined by **Rockstar** and BCGs defined by their cluster finding method, it is difficult to find centers of clusters defined by **Rockstar** in observations. Hence, they use peaks of X-ray and SZ signals as proxy to true cluster centers to estimate

the frequency of miscentering by their cluster finding method.

In Rykoff et al. (2016), they model the PDF of the miscentering effect as

$$p(x) = \frac{\rho_0}{\sigma_0\sqrt{2\pi}} \exp\left(-\frac{x^2}{2\sigma_0^2}\right) + \frac{(1-\rho_0)x}{\sigma_1^2} \exp\left(-\frac{x^2}{2\sigma_1^2}\right), \quad (5.19)$$

where  $\rho_0$ ,  $\sigma_0$ , and  $\sigma_1$  are free parameters,  $x = r/R_\lambda$ ,  $r$  is the projected radius of the BCGs from peaks of X-ray and SZ signals, and  $R_\lambda$  is the projected radius of the galaxy clusters with richness  $\lambda$ , defined in eq. (3.4). The first term of right hand side corresponds to the BCGs-X-ray (SZ) center offset, and the second term represents systematic failures in identifying the correct BCGs with their cluster finding method. They obtained  $\rho_0 = 0.78_{-0.11}^{+0.11}$  and  $\sigma_1 = 0.31_{-0.05}^{+0.09}$  by comparing the offset distribution derived from the observations mentioned above with eq. (5.20). They marginalize over the parameter  $\sigma_0$  since it is not relevant to the overall fraction of misidentified BCGs.

The miscentering affects the PDF of the line-of-sight velocity in two aspects. First, we mis-measure redshifts of BCGs. This causes systematic errors to  $v_{\text{los}}$ . Second, we mis-measure the projected radii to member galaxies. The first aspect distorts the PDF of the line-of-sight velocity in the similar way as in eq. (5.16), i.e.,

$$E(x) = \frac{1-\rho_0}{\sigma_{\text{BCG}}\sqrt{2\pi}} \exp\left(-\frac{x^2}{2\sigma_{\text{BCG}}^2}\right) + \rho_0\delta(x), \quad (5.20)$$

where  $\sigma_{\text{BCG}}$  is the typical line-of-sight velocity between correct BCGs and galaxies misidentified as BCGs. Estimating values of  $\sigma_{\text{BCG}}$  and discussions of the second aspect are left for future work.



# Chapter 6

## Summary and Future Prospects

In this thesis, we study the phase space distribution of dark matter halos around galaxy clusters using an  $N$ -body simulation. We find that motions of most dark matter halos are not virialized even at  $z = 0$ , although previous studies to measure dynamical masses of galaxy clusters relied on the virial theorem. We construct a new model of the phase space distribution of dark matter halos, adopting a two component model for the phase space distribution. One component is the infall component, and the other is the splashback component. This two component model is in good agreement with the stacked phase space distribution of dark matter halos for a wide range of radii. This model reproduces the double peak histogram of the radial velocity distribution accurately. We find that the radial velocity distribution deviates from the Gaussian distribution even at large radii, which we model the Johnson's SU distribution to reflect the skewness and kurtosis. After fitting the model function of the phase space distribution with stacked phase space distribution obtained from the  $N$ -body simulation, we derived the dependence of these parameters on the radius  $r$ . We find that the phase space distribution shows dependence on galaxy cluster masses even at  $r > 20 \text{ Mpc}/h$ . This suggests that we can extract galaxy cluster masses from the dynamics of dark matter halos at large  $r$ . We also study the satellite-halo and sub-halo mass dependence of the phase space distribution to find that the phase space distribution is affected by satellite-halo and sub-halo selections, albeit weakly.

We then predict the PDF of  $v_{\text{los}}$  from our model of the phase space distribution by projecting our model phase space distribution along the line-of-sight with the effect of the Hubble flow, and find that our model is in good agreement with the PDF of  $v_{\text{los}}$  directly obtained from the mock observation from our simulation. We show that we can indeed estimate galaxy cluster masses by using motions of galaxies at large radii,  $r_{\text{proj}} > 2 \text{ Mpc}/h$ . We discuss the origin of the galaxy cluster mass dependence on the PDF of  $v_{\text{los}}$ , which is complicated due to competing effects of the infall velocity and the Hubble flow.

Finally, we discuss the accuracy of galaxy cluster masses by using the PDF of  $v_{\text{los}}$  at  $2 \text{ Mpc}/h < r_{\text{proj}} < 12 \text{ Mpc}/h$ . We conclude that, by using SDSS spectroscopic galaxies, we can detect about 4% difference of average cluster masses at  $1\sigma$ . We also discuss potential systematic errors of galaxy cluster mass estimations, such as the satellite-halo and sub-halo mass dependence of the PDF and the inaccuracy of our model. We find that

these effects can make significant contributions to the error budget of the mass estimation when a large number of spectroscopic galaxies are used.

Our next step is to improve our model of the phase space distribution. Moreover, we will apply our method of dynamical mass measurements to observations such as SDSS and Subaru Hyper Suprime-Cam survey, which should provide useful and complementary information on large samples of clusters in these surveys.

# Acknowledgments

First of all, I would like express my gratitude and respect to Masamune Oguri who introduced me to the research for his continuous encouragement and advice. I acknowledge my collaborator Takahiro Nishimichi who gave me invaluable comments and warm encouragements. I also acknowledge my supervisor Prof. Yasushi Suto who provided carefully considered feedback.

I would like to gratitude all the members in the University of Tokyo Theoretical Astrophysics (UTAP) and Research Center for the Early Universe (RESCEU) who always provided me with a comfortable research environment.

Finally, I would like to thank my family and friends, who always respect my decisions and support me in various ways.



# Appendix A

## Review of a Cluster Finding Method

In this Appendix, we review the cluster finding method CAMIRA (Oguri 2014) as an example of red-sequence cluster finding methods.

### A.1 Calculating Probability of Red Sequence Galaxy

In CAMIRA, they use a stellar population synthesis (SPS) model of Bruzual & Charlot (2003) to model the red-sequence and its dispersion. In Bruzual & Charlot (2003), they derived colors and magnitudes of galaxies as a function of age, metallicity ( $Z_{\text{SPS}}$ ), stellar mass ( $M_*$ ), and dust extinction. In CAMIRA, they adopt an approximations that all galaxies are formed at redshift  $z_f = 3$  and no dust extinction.

Given the fixed formation redshift, the red-sequence by the relationship between  $Z_{\text{SPS}}$  and  $M_*$  as

$$Z_{\text{SPS}} = Z_{11} + a_Z[\log(M_*/10^{11}M_\odot)], \quad (\text{A.1})$$

where  $Z_{11}$  is the normalization of metallicity, and  $a_Z = 0.15$ .

The SPS model fitting is based on  $\chi^2$  defined by

$$\chi^2 = \sum_i^{N_{\text{fil}}} \frac{(m_{i;\text{obs}} - m_{i;\text{SPS}} - \delta m_{i;\text{resi}})^2}{\sigma_{m_{i;\text{obs}}}^2 + \sigma_{m_{i;\text{resi}}}^2} + \frac{\log Z_{11} - \log \overline{Z_{11}}}{\sigma_{\log Z}^2}, \quad (\text{A.2})$$

where  $N_{\text{fil}}$  is the number of photometric band filters of the galaxy catalog,  $m_{i;\text{obs}}$  and  $\sigma_{m_{i;\text{obs}}}$  are observed magnitude and its error in the  $i$ -th band, and  $\sigma_{m_{i;\text{resi}}}$  corresponds to the scatter of the spectra energy distribution of red-sequence galaxies. Also,  $m_{i;\text{SPS}}$  is the SPS model predicted magnitude in the  $i$ -th band as a function of the galaxy redshift  $z$ ,  $M_*$  and  $Z_{\text{SPS}}$ , and  $\log \overline{Z_{11}} = -2$  and  $\sigma_{\log Z} = 0.14$ .

They include the correction term  $\delta m_{i;\text{resi}}$ , which is the difference between the spectral energy distribution predicted by the SPS model and the observed one. More specifically,  $\delta m_{i;\text{resi}}$  is estimated by comparing spectral energy distributions of spectroscopic galaxies and SPS model predictions, which is modeled as

$$\delta m_{\text{resi};\text{fit}}(\lambda, z_j) = \sum_i^{n_f} a_i(z_j)(\lambda - \lambda_0)^i, \quad (\text{A.3})$$

where  $\lambda_0$  is 5000Å,  $\lambda$  is the rest-frame wavelength, and  $a_i(z_j)$  are fitting parameters.

The process for calculating  $\delta m_{i:\text{resi}}$  (or  $a_i(z_j)$ ) and  $\sigma_{m_{i:\text{resi}}}$  is as follow. First, they minimize  $\chi^2$  for each spectroscopic galaxy by varying  $M_*$  and  $Z_{11}$  with  $\delta m_{i:\text{resi}} = 0$  and  $\sigma_{m_{i:\text{resi}}} = 0$ . Next, they remove  $\log Z_{11} > -1.65$  and  $\log Z_{11} < -2.35$  as outliers. Then, they fit  $a_i(z_j)$  using galaxies with  $\chi^2 < 4$  and estimate the scatter of  $(m_{i:\text{obs}} - m_{i:\text{SPS}} - \delta m_{i:\text{resi}})$ , which correspond to  $\sqrt{\sigma_{m_{i:\text{obs}}}^2 + \sigma_{m_{i:\text{resi}}}^2}$ , using galaxies with  $\chi^2 < 20$  and fixing  $\sigma_{m_{i:\text{resi}}}$ .

The degree of freedom of  $\chi^2$  calculated in eq. (A.2) for each galaxy is  $N_{\text{fil}} - 1$  ( $\equiv \nu$ ). Hence, the distribution of  $\chi^2$  should obey the  $\chi^2$  distribution with  $\nu$  degrees of freedom

$$\frac{dp_\nu}{d\chi^2} = \frac{1}{2^{\nu/2}\Gamma(\nu/2)} e^{\chi^2/2} (\chi^2)^{\nu/2-1}. \quad (\text{A.4})$$

Then, they define a "number parameter" as

$$n_\nu(\chi^2) = \frac{2^{3\nu/4}}{\nu^{\nu/2} U(\nu/4, 1/2, \nu^2/8)} e^{-(\chi^2)^2/2}, \quad (\text{A.5})$$

where  $U(a, b, c)$  is the confluent hypergeometric function of second kind. Note that the number parameter is normalized so as to satisfy

$$\int_0^\infty d\chi^2 n_\nu \frac{dp_\nu}{d\chi^2} = 1. \quad (\text{A.6})$$

## A.2 Calculating the Number of Member Galaxies

They count the number of red-sequence galaxies in a specific stellar mass range and within some aperture to define richness. The stellar mass filter is

$$F_M(M_{*,\text{in}}) = \exp \left[ - \left( \frac{M_{*,\text{in}}}{M_h} \right)^4 - \left( \frac{M_1}{M_{*,\text{in}}} \right)^4 \right] \quad (\text{A.7})$$

where  $M_h = 10^{13} M_\odot$  and  $M_1 = 10^{10.2} M_\odot$  are adopted here. The spatial filter is

$$F_R(R) = \frac{\Gamma[n/2, (R/R_0)^2] - (R/R_0)^n e^{-(R/R_0)^2}}{\Gamma(n/2, 0)}, \quad (\text{A.8})$$

where  $n = 4$  and  $R_0 = 0.8h^{-1}$  are adopted here.

By using eqs. (A.5), (A.7), and (A.8), the number of red-sequence galaxies at  $(\boldsymbol{\theta}, z)$  can be described as

$$N_{\text{mem}}(\boldsymbol{\theta}, z) = \sum_i n_\nu(\chi_i^2; \boldsymbol{\theta}_i; z) F_M(M_{*,i}) F_R(D_A | \boldsymbol{\theta}_i - \boldsymbol{\theta}|), \quad (\text{A.9})$$

where  $D_A$  is the angular diameter distance at redshift  $z$ . From eq. (A.9), they search peaks of the  $N_{\text{mem}}$  map from the celestial sphere  $(\boldsymbol{\theta}_p)$ .

## A.3 Refining Cluster Candidates

They determine the likelihood of the cluster redshift for each identified peak as

$$\ln \mathcal{L}_z = -\frac{1}{2} \sum_i w_i \chi_i^2(\boldsymbol{\theta}_i, z) \Theta[F_R(D_A|\boldsymbol{\theta}_i - \boldsymbol{\theta}_p|)], \quad (\text{A.10})$$

where  $\Theta$  is the Heaviside step function. The weight  $w_i$  is introduced to use only high significance cluster member galaxies for estimating the cluster redshift. It is defined as

$$w_i = \frac{1}{1 + \exp\{(n_{\text{th}} - n_{\text{mem},i})/\sigma_n\}}, \quad (\text{A.11})$$

where

$$n_{\text{mem},i} = n_\nu(\chi_i^2; \boldsymbol{\theta}_i, z) F_M(M_{*,i}) F_R(D_A|\boldsymbol{\theta}_i - \boldsymbol{\theta}_p|), \quad (\text{A.12})$$

and  $n_{\text{th}}$  is defined as

$$\sum_{n_{\text{mem},i} > n_{\text{th}}} n_{\text{mem},i} = f_n N_{\text{mem}}(\boldsymbol{\theta}_p, z), \quad (\text{A.13})$$

where  $f_n = 0.5$  and  $\sigma_n = 0.05$  are adopted here. The cluster redshift  $z_{\text{cl}}$  is the redshift that minimizes the likelihood defined by eq. (A.10).

They determine the likelihood of each galaxy being the BCG of the cluster as

$$\ln \mathcal{L}_{\text{BCG}} = -\frac{[\log(M_{*,i}/M_{*,\text{BCG}})]^2}{2\sigma_{\log M}^2} + \ln n_\nu(\chi^2) - \frac{(D_A|\boldsymbol{\theta}_i - \boldsymbol{\theta}_p|)^2}{\sigma_R^2}, \quad (\text{A.14})$$

where,  $M_{*,\text{BCG}} = 10^{12.3} M_\odot$ ,  $\sigma_{\log M} = 0.3$ , and  $\sigma_R = 0.3h^{-1}$  are adopted here. All variables are calculated at  $z = z_{\text{cl}}$  determined in eq. (A.10). Eq. (A.14) means that a galaxy with larger stellar masses, with the red-sequence color, and located near the peak of the richness map is more likely to be the BCG.

After they obtain the location of the most likely BCG,  $\boldsymbol{\theta}_{\text{BCG}}$ , they recalculate  $z_{\text{cl}}$  by using eq. (A.10) with  $\boldsymbol{\theta}_p \rightarrow \boldsymbol{\theta}_{\text{BCG}}$ . Then, they calculate eq. (A.14) with updated  $z_{\text{cl}}$ . This process is repeated until it converge.

Finally, they estimate  $N_{\text{mem}}(\boldsymbol{\theta}_{\text{BCG}}, z_{\text{cl}})$  of the galaxy cluster using eq. (A.9) to define richness of the galaxy cluster.



# Appendix B

## Comparison Between Velocity Dispersions and Cluster Masses

In this Appendix, we show the comparison between  $\sigma_{\mathcal{G}}$  and cluster masses obtained from our simulation. The difference between Fig. 3.4 in Section 3.3 and Fig. B.1 is as follows. First, we use  $\sigma_{\mathcal{G}}$  instead of  $\sigma_{1D}$ . We calculate  $\sigma_{\mathcal{G}}$  by fitting eq. (3.5) to the  $v_{\text{los}}$  histogram. Second, we set the fitting range to  $-2000 \text{ km/s} < v_{\text{los}} < 2000 \text{ km/s}$ .

In Fig. B.1, we show the comparison between  $\sigma_{\mathcal{G}}$  and cluster masses. We can see that the relation between  $\sigma_{\mathcal{G}}$  and cluster masses is significantly different from "virialized line", i.e., the expected relation for virialized halos, motions of dark matter halos around galaxy clusters are not yet fully virialized as we show in Chapter 4. Hence, we cannot obtain accurate cluster masses based on the method presented in Section 3.3.

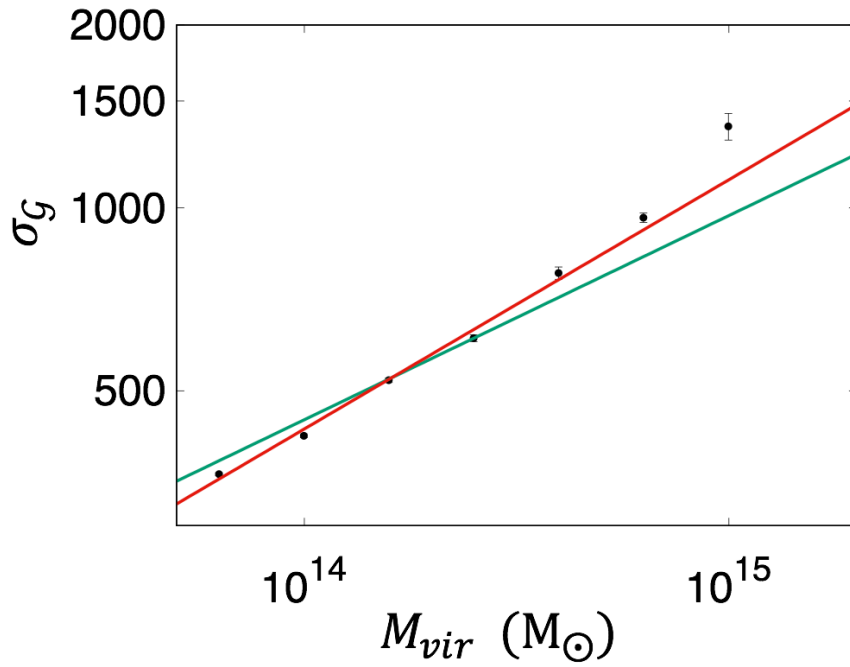


Figure B.1: The relation between cluster mass  $M_{vir}$  and velocity dispersions of dark matter halos. Filled circles are  $\sigma_G$  obtained from our simulation, the red line is the best fit line of eq. (3.8), and the green line is "virialized line" which is same as the one shown in Fig. 3.4. The best fit parameters for the red line are  $A_2 = 1288 \pm 20$  km/s and  $\alpha = 0.410 \pm 0.006$ . The parameters for the green line are  $A_2 = 1095$  km/s and  $\alpha = 0.336$ .

# References

- Arnaud, M., Pratt, G. W., Piffaretti, R., et al. 2010, *A&A*, 517, A92
- Behroozi, P. S., Loeb, A., & Wechsler, R. H. 2013a, *Journal of Cosmology and Astroparticle Physics*, 6, 019
- Behroozi, P. S., Wechsler, R. H., & Wu, H.-Y. 2013b, *ApJ*, 762, 109
- Bleem, L. E., Stalder, B., de Haan, T., et al. 2015, *ApJS*, 216, 27
- Bruzual, G., & Charlot, S. 2003, *MNRAS*, 344, 1000
- Busha, M. T., Evrard, A. E., Adams, F. C., & Wechsler, R. H. 2005, *MNRAS*, 363, L11
- Dawson, K. S., Schlegel, D. J., Ahn, C. P., et al. 2013, *AJ*, 145, 10
- Diaferio, A., & Geller, M. J. 1997, *ApJ*, 481, 633
- Dunkley, J., Spergel, D. N., Komatsu, E., et al. 2009, *ApJ*, 701, 1804
- Farahi, A., Evrard, A. E., Rozo, E., Rykoff, E. S., & Wechsler, R. H. 2016, *MNRAS*, 460, 3900
- Hahn, O., & Abel, T. 2011, *MNRAS*, 415, 2101
- Hinshaw, G., Larson, D., Komatsu, E., et al. 2013, *ApJS*, 208, 19
- Johnson, N. L. 1949, *Biometrika*, 36., 149
- Johnston, D. E., Sheldon, E. S., Wechsler, R. H., et al. 2007, *ArXiv e-prints*, arXiv:0709.1159
- Koester, B. P., McKay, T. A., Annis, J., et al. 2007, *ApJ*, 660, 239
- Lam, T. Y., Schmidt, F., Nishimichi, T., & Takada, M. 2013, *Phys. Rev. D*, 88, 023012
- Lewis, A., Challinor, A., & Lasenby, A. 2000, *ApJ*, 538, 473
- Mansfield, P., Kravtsov, A. V., & Diemer, B. 2017, *ApJ*, 841, 34
- Mo, H., van den Bosch, F. C., & White, S. 2010, *Galaxy Formation and Evolution*

- Munari, E., Biviano, A., Borgani, S., Murante, G., & Fabjan, D. 2013, *MNRAS*, 430, 2638
- Murata, R., Nishimichi, T., Takada, M., et al. 2017, *ArXiv e-prints*, arXiv:1707.01907
- Nandra, R., Lasenby, A. N., & Hobson, M. P. 2012, *MNRAS*, 422, 2931
- Newman, A. B., Treu, T., Ellis, R. S., et al. 2013, *ApJ*, 765, 24
- Nojiri, S., & Odintsov, S. D. 2011, *Phys. Rep.*, 505, 59
- Oguri, M. 2014, *MNRAS*, 444, 147
- Oguri, M., Bayliss, M. B., Dahle, H., et al. 2012, *MNRAS*, 420, 3213
- Planck Collaboration, Ade, P. A. R., Aghanim, N., et al. 2014, *A&A*, 571, A20
- Rozo, E., Rykoff, E. S., Becker, M., Reddick, R. M., & Wechsler, R. H. 2015, *MNRAS*, 453, 38
- Rozo, E., Wechsler, R. H., Rykoff, E. S., et al. 2010, *ApJ*, 708, 645
- Rykoff, E. S., Rozo, E., Busha, M. T., et al. 2014, *ApJ*, 785, 104
- Rykoff, E. S., Rozo, E., Hollowood, D., et al. 2016, *ApJS*, 224, 1
- Sarazin, C. L. 1988, *X-ray emission from clusters of galaxies*
- Schmidt, F. 2010, *Phys. Rev. D*, 81, 103002
- Schneider, P., Ehlers, J., & Falco, E. E. 1992, *Gravitational Lenses*, 112, doi:10.1007/978-3-662-03758-4
- Scoccimarro, R. 2004, *Phys. Rev. D*, 70, 083007
- Smith, S. 1936, *ApJ*, 83, 23
- Springel, V. 2005, *MNRAS*, 364, 1105
- Stark, A., Miller, C. J., & Gifford, D. 2016, *ApJ*, 830, 109
- Stott, J. P., Pimblet, K. A., Edge, A. C., Smith, G. P., & Wardlow, J. L. 2009, *MNRAS*, 394, 2098
- Sunyaev, R. A., & Zeldovich, Y. B. 1972, *Comments on Astrophysics and Space Physics*, 4, 173
- Umetsu, K., Broadhurst, T., Zitrin, A., Medezinski, E., & Hsu, L.-Y. 2011, *ApJ*, 729, 127
- Vikhlinin, A., Kravtsov, A., Forman, W., et al. 2006, *ApJ*, 640, 691
- York, D. G., Adelman, J., Anderson, Jr., J. E., et al. 2000, *AJ*, 120, 1579
- Zu, Y., & Weinberg, D. H. 2013, *MNRAS*, 431, 3319